Using non-contact AFM to study the local doping and damping through the transition in an ultrathin VO_2 film

A DISSERTATION PRESENTED
BY
ALYSON SPITZIG
TO
THE DEPARTMENT OF PHYSICS

IN PARTIAL FULFILLMENT OF THE REQUIREMENTS
FOR THE DEGREE OF
DOCTOR OF PHILOSOPHY
IN THE SUBJECT OF
PHYSICS

HARVARD UNIVERSITY
CAMBRIDGE, MASSACHUSETTS
MAY 2023

Thesis advisor: Professor Jenny Hoffman Alyson Spitzig

Using non-contact AFM to study the local doping and damping through the transition in an ultrathin VO_2 film

Abstract

Bulk VO_2 undergoes an insulator-to-metal transition (IMT) with up to five order of magnitude change its resistivity at 340 K. However, when VO_2 is deposited as a film on a substrate, the strain from the substrate can alter the IMT temperature, resistivity ratio, and hysteresis. Here, we present single-phase VO_2 ultrathin films (thickness less than 20 nm) grown using oxygen plasma molecular beam epitaxy (MBE) on $TiO_2(001)$ and $Al_2O_3(0001)$ substrates. First, we modify existing recipes employing ozone MBE and reproduce the best reported films on $TiO_2(001)$; maintaining an almost three order of magnitude transition in a 12 nm thick film. We then extend our recipe to $Al_2O_3(0001)$ substrates where we stabilize a 12 nm thin single-phase VO_2 film and observe a two order of magnitude transition, expanding the possible growth methods for ultrathin VO_2 films on $Al_2O_3(0001)$.

In a separate, approximately 10 nm thick VO_2 film on $TiO_2(001)$, we use non-contact AFM (nc-AFM) to track electronic properties across the expected temperature range of transition. We first observe a change in the work function of VO_2 at the expected bulk transition temperature. We then measure the frequency shift and

dissipation at varying bias and tip-sample separation at seven stable temperatures, spanning the insulating to the metallic state. Using the frequency shift data, we extract the tip-sample capacitance, then calculate the induced carrier doping within the sample as a result of the proximity of the tip. The work function, carrier density, and damping results above and below the IMT suggest that we observe the IMT; with the damping in particular showing consistent behavior with a decrease in resistance starting as low at 270 K and continuing to 300 K. Furthermore, we observe a change in work function at fixed temperature at close tip-sample separation as low as 240 K, along with elevated damping, suggesting the electric field from the tip itself may be initiating the transition, at least in the surface of the film, at temperatures as low as 240 K in the close tip-sample separation regime.

Contents

1 Introduction: vanadium dioxide **1**
- 1.1 A Mott or Peierls transition . . . 7
- 1.2 Overview of this work . . . 12

2 Molecular beam epitaxy growth of ultrathin VO_2 films **13**
- 2.1 Substrates . . . 14
- 2.2 Film growth and characterization . . . 18
- 2.3 Conclusion . . . 39

3 Non-contact atomic force microscopy **41**
- 3.1 Geometry and Terms . . . 42
- 3.2 Fabricating qPlus probes for nc-AFM . . . 50
- 3.3 Our system: the 'RHK' . . . 52
- 3.4 Approach and calibration . . . 56
- 3.5 Data collection: z-V_b maps . . . 61
- 3.6 Theoretical dependencies of the measured data . . . 63

4 Doping and dissipation measured across the IMT in VO_2 **75**
- 4.1 Δf: drift correction . . . 78
- 4.2 Force: sample position, work function, and doping . . . 80
- 4.3 Drive voltage: damping coefficient and dissipation . . . 94
- 4.4 Conclusion . . . 100

Appendix A *Ex situ* characterization of the film studied via nc-AFM **102**

References **122**

Listing of figures

1.1 Insulator to metal transitions in V-O compounds 2
1.2 Bulk rutile and monoclinic lattices of VO_2 4
1.3 Intermediate lattice phases in VO_2 5
1.4 The resulting band energy from an equally spaced chain of atoms and a dimerized chain 10

2.1 VO_2 thin films from literature showing thinner VO_2 films tend the reduce the reported RR between the insulating and metallic state measured through transport 16
2.2 All V-O films grown in our lab and resulting phase from XRD overlayed with resulting transport 20
2.3 Representative XRR curve and simulation 23
2.4 Schematic of the constructive interference measured during a typical XRD scan 26
2.5 XRD of seven VO_2 ultrathin films grown on $TiO_2(001)$ and $Al_2O_3(0001)$ 29
2.6 View of the top-most layer of Al atoms and a single layer of V atoms in the monoclinic $VO_2(020)$ orientation 31
2.7 Transport of ultrathin VO_2 films grown on $TiO_2(001)$ and on $Al_2O_3(0001)$ 33
2.8 Representative first and second derivative of the log of the resistance to determine IMT properties in VO_2 thin films 34
2.9 XRD and transport of a sample without a post-growth anneal showing rutile VO_2 was crystallized but does not exhibit a transition 36
2.10 AFM topography of all seven samples studied here 38

3.1 Schematic of nc-AFM operation using a qPlus sensor 43
3.2 A typical frequency sweep used to determine the resonant frequency of the tip 45
3.3 Fabrication details of a qPlus probe for use with the RHK 51
3.4 The equivalent circuit model for quartz resonators, such as a qPlus probe 55
3.5 A typical frequency sweep used to determine the range of good frequencies for this probe 56
3.6 Representative force-distance sweep and corresponding Δf-distance curve, showing the attractive and repulsive regimes 59
3.7 Representative tip amplitude calibration between A_e and A_{osc}. 61
3.8 Representative force-distance sweep with separated forces 67

3.9 Schematic of the origin of the contact potential difference (CPD) 70

4.1 Characterization of a copy of the film studied throughout Chapter 4 . . 77
4.2 Correcting for phase drift and subsequent Δf shift 79
4.3 Correcting for any piezo drift but comparing Δf-z curves taken during and during the measurement 80
4.4 Using force-distance curves to determine sample position and tip radius 82
4.5 Representative force-bias curve with fit to determine the CPD voltage . 83
4.6 Bulk resistance and work function change through the IMT 86
4.7 The tip-sample separation dependence of the work function 87
4.8 Representative force-bias fit to determine $\partial C(z)/\partial z$ for each temperature 88
4.9 $\partial C(z)/\partial z$ functional fits 91
4.10 z and V_b dependence of the carrier density in the sample induced by the tip 93
4.11 Damping-bias curves for each temperature at $z = 8$ nm. 95
4.12 Parabolic fitting to the damping coefficient at all temperatures 96
4.13 Theoretical damping coefficient as the result of a phase change within a bias sweep 98
4.14 Damping coefficient at fixed z and V_b vs temperature 99

A.1 Timeline of the Air and Vacuum Samples 105
A.2 XRD and transport characterization of the Air Sample 106
A.3 Transport on the Air Sample over 22 months 107
A.4 XRD and transport characterization of the Vacuum Sample 108
A.5 Full XRD of both the Air Sample and Vacuum sample 108
A.6 XRR of both the Air and Vacuum sample. 109
A.7 AFM topography of the Air and Vacuum Samples at scales from 5 μm to 500 nm. 110

Listing of tables

2.1 Summary of sample thicknesses determined from XRR simulations . . . 22
2.2 Summary of the relevant XRR fitting parameters 24
2.3 Summary of IMT properties of seven ultrathin VO_2 films grown on TiO_2(001) and Al_2O_3(0001) 35

3.1 Table of variables used to describe nc-AFM operation 48

A.1 Timeline of the Air and Vacuum Samples. 105

For Chepstow.

Acknowledgments

First and foremost I would like to thank my advisor, Prof. Jenny Hoffman. She pushed me when I needed a push, but also gave me the tools to figure things out on my own time. She frequently was able to hone in on the problem and ask the relevant questions to get it resovled.

I would also like to thank my committee at Harvard, Prof. Julia Mundy and Prof. Boris Kozinsky for their words of encouragement and useful feedback throughout the years. I also need to give a special shout out to Dr. Jason Hoffman and Dr. Dilek Yildiz for their specific areas of expertise and advice when it came to film growth and non-contact AFM respectively. They offered valuable advice with respect to the Ph.D. and to life in general.

I would like to thank all the members of the Hoffman group that I overlapped with. Our conversations made the process more fun and I learned a lot from each of you!

And of course, I would like to thank all my family and friends who supported me these past 6 years.

Last, but certainly not least, I need to acknowledge Mike. There's really not enough words to describe how supportive he's been since we met.

1

Introduction: vanadium dioxide

Vanadium dioxide, VO_2, has been continuously studied for over six decades due to the abrupt insulator to metal transition (IMT) with resistivity changing by up to five orders of magnitude, and accompanying structural phase transition (SPT) from monoclinic to rutile; both of which occur above room temperature around 340 K[1,2,3]. In

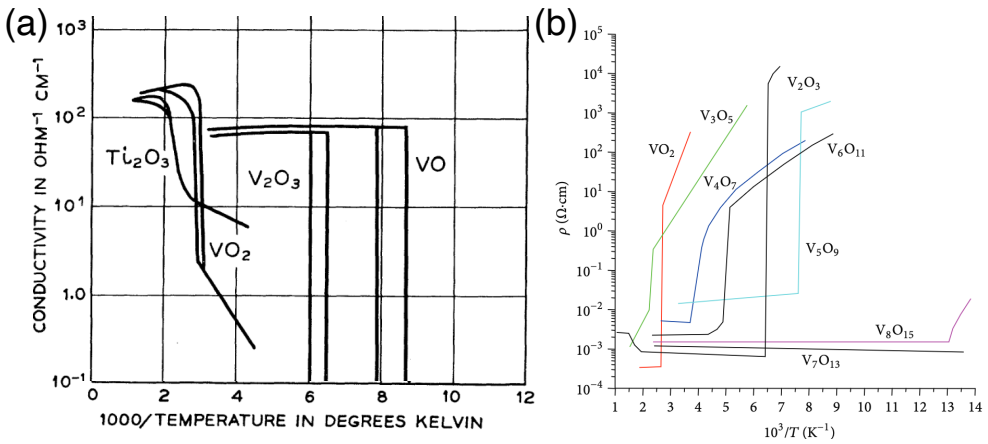

Figure 1.1: (a) Initial IMT characteristics of VO_2, V_2O_3 and VO, plotted as conductivity vs inverse temperature. Adapted from Morin[1]. (b) IMT characteristics of VO_2, V_2O_3, VO, and the Magneli phases: V_nO_{2n-1} ($3 \leq n \leq 9$), plotted as resistivity vs inverse temperature. Reproduced from Pergament *et al.*[4]. Of these compounds only VO_2 and V_3O_5 exhibit an IMT above room temperature, with T_{IMT} of VO_2 being closer to room temperature than V_3O_5.

the same study, the results of which are shown in Fig. 1.1 (a), Morin also observed an IMT in both V_2O_3 and VO[1]. Since then, an IMT has been demonstrated in many other V-O compounds, named the Magneli phases with the chemical formula V_nO_{2n-1} ($3 \leq n \leq 9$), which could be considered intermediate structures between V_2O_3 ($n = 2$) and VO_2 ($n \to \infty$). With the exception of V_7O_{13}, each of these V-O compounds exhibits an IMT, with their compiled transport shown in figure 1.1 (b)[4]. VO_2 is one of only two such compounds that have the IMT temperature (T_{IMT}) above room temperature, and of those it is the closest to room temperature with the largest change in resistivity between the insulating and metallic phase.

While the IMT was first observed by Morin in 1959[1], the SPT was not described until 1971[2]. At elevated temperatures, nominally above the IMT and in the metal-

lic state, VO_2 has a rutile structure with $a_R = b_R = 4.5540$ Å and $c_R = 2.8557$ Å, with each axis at 90° to each other (measured at 400 K)[5], and at low temperatures, nominally in the insulating state, the lattice transitions to the monoclinic structure. Each lattice is shown in Fig. 1.2, with (a) showing the rutile phase, with unit cell outlined in solid black lines. The corresponding monoclinic unit cell is shown as a dotted line. Similarly, panel (b) show the monoclinic lattice, with unit cell in solid black and corresponding rutile unit cell as a dotted line. To differentiate between monoclinic and rutile we use subscript R for rutile and M for monoclinic. Through the transition the V atoms along c_R pair, and twist off-axis. The pairing doubles the unit cell, and the twisting changes the unit cell symmetry from tetragonal to monoclinic[3]. To stay consistent with monoclinic nomenclature, a_M points in the direction of c_R and c_M is at 122.61° with respect to a_M, resulting in a switch in the direction of the b-axis between the phases. Figure 1.2 shows eight V atoms at the edge of the unit cell and three V atoms from the center of the unit cell in the rutile and monoclinic phases, along the b-axis each unit cell (or $VO_2[010]_R$ and $VO_2[0\bar{1}0]_M$) and corresponding lattice constants.

To convert from rutile Miller indices to monoclinic Miller indices we use the follow-

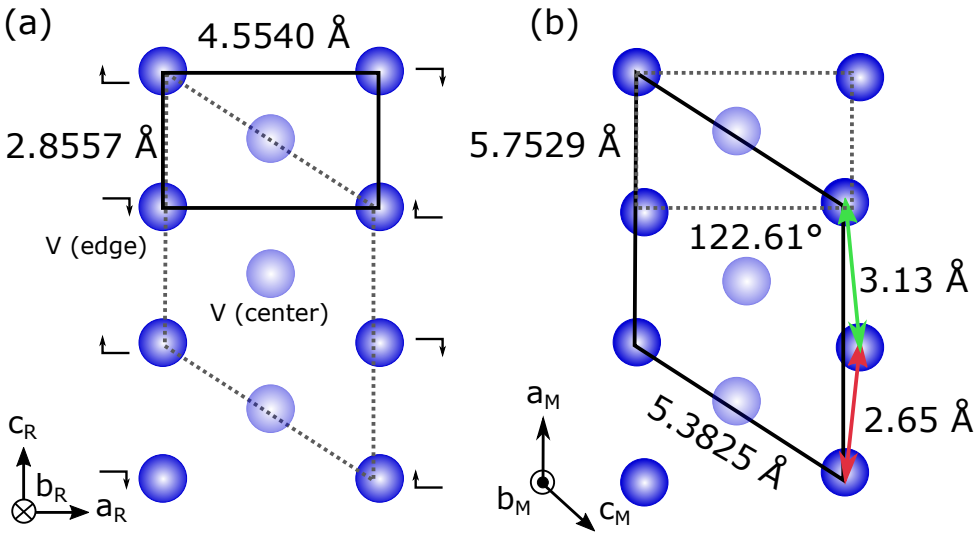

Figure 1.2: Vanadium atoms in the bulk rutile and monoclinic lattice of VO_2. (a) Three rutile unit cells, with the unit cell outlined in solid lines. The corresponding monoclinic unit cell is shown with a dotted line. The arrows next to the V atoms show their relative motion into the monoclinic phase. (b) 1.5 monoclinic unit cells, with the unit cell outlined in solid lines. The corresponding rutile unit cell is shown with a dotted line. The alternating V dimer distances along c_R are labeled with a red and green arrow.

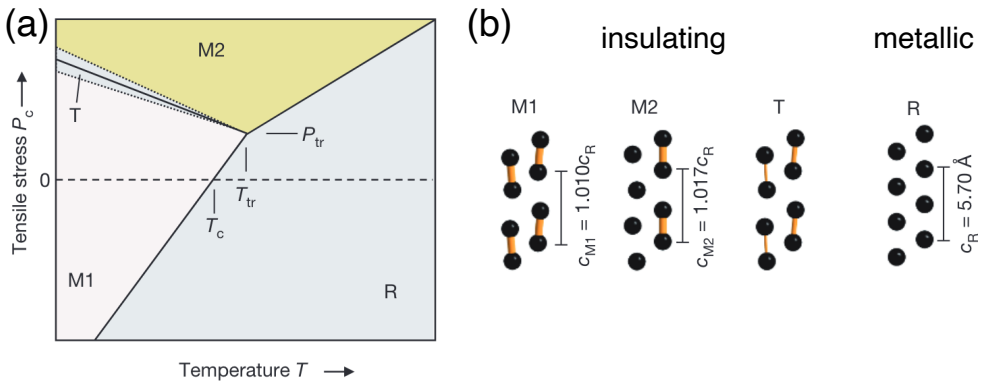

Figure 1.3: (a) Phase-coexistence point of the monoclinic, rutile, and triclinic phases in VO_2, measured through applying nano-mechanical strain to nanobeams of VO_2. (b) Two unit cells of each of the structural phases of VO_2, with the c_R axis pointing upwards. M1 refers to the low-temperature monoclinic phase shown in Fig. 1.2, M2 refers to an intermediate monoclinic phase where only half of the V atoms are dimerized, T refers to the triclinic phase where half of the V atoms are dimerized and the other half are rotated off-axis, and R refers to the high-temperature rutile phase. Reproduced from Park *et al.*[6].

ing transformation matrix:

$$\begin{pmatrix} \mathrm{h} \\ \mathrm{k} \\ \mathrm{l} \end{pmatrix}_M = \begin{pmatrix} 0 & 0 & 2 \\ 0 & \bar{1} & 0 \\ \bar{1} & 0 & \bar{1} \end{pmatrix} \begin{pmatrix} \mathrm{h} \\ \mathrm{k} \\ \mathrm{l} \end{pmatrix}_R . \tag{1.1}$$

There are two intermediate lattices between the insulating monoclinic (M) and metallic rutile (R), shown in Fig. 1.3 (b); a second monoclinic phase (M2) in which only half of the V chains along c_R dimerize (but do not twist off-axis), and a triclinic phase (T) in which half of the V chains are dimerized but not rotated and the other half are rotated off axis but not dimerized[6].

Due to the large change in film properties at close-to-room temperatures, there are

many potential applications that harness the switching behavior in VO_2. Some of the first applications are night vision googles[7] or efficient window coatings[8]. More recently, VO_2 has attracted further interest for infrared detectors[9], THz metamaterials[10,11], memristors[12], Mott transistors[13], neuromorphic computing materials[14], and memory storage devices[15,16]. These applications benefit from high quality films with the resistivity ratio between the insulating and metallic state (RR_{IMT}) greater than three orders of magnitude and the width of the transition being less than 25 K[13,14,16].

$TiO_2(001)$ and $Al_2O_3(0001)$ substrates are commonly used for VO_2 thin film growth because single-crystal films can be obtained that exhibit a sharp IMT. When grown on $Al_2O_3(0001)$, the IMT temperature is typically close to bulk, around 340 K, and when grown on $TiO_2(001)$ the IMT temperature is reduced to around 290 K[17], below room temperature, both of which can be desirable for different applications. However, VO_2 films 30 nm or thicker grown on $TiO_2(001)$ are known to crack due to thermal stress[18,19,20,21]. As a result, ultrathin (thickness less than 20 nm) VO_2 films on $TiO_2(001)$ have been well optimized, achieving RR_{IMT} of 10^3 and sharpness of 2 K[19]. On the other hand, VO_2 films on $Al_2O_3(0001)$ have been a challenge to grow thinner than 20 nm and measure transport due to the Volmer-Weber growth mode (i.e., island growth)[22,23]. A key question then, is whether the desirable IMT properties can be reliably manufactured and reproduced in ultrathin films on both $TiO_2(001)$ and $Al_2O_3(0001)$[24]. In chapter 2, we discuss growth procedures for single-crystal VO_2 ultrathin films using oxygen plasma MBE on $TiO_2(001)$ with RR_{IMT} around 3 orders of

magnitude and on $Al_2O_3(0001)$ that maintains a RR_{IMT} of 2 orders of magnitude.

Besides temperature, the IMT can be trigged through an applied bias[25] (although it is yet unresolved whether the transition is due to field effects[26] or Joule heating[27,28,29]), gating causing charge injection[30], and photoexcitation via ultrafast lasers pulses[31,32,33]. The IMT can be suppressed through strain[17], oxygen vacancies[19] or back gating[34,13]. To further elucidate some of the bias-triggered transitions, we use non-contact atomic force microscopy (nc-AFM) to track the local Joule dissipation and the induced charge through the transition. We discuss these results in Chapter 4.

1.1 A Mott or Peierls transition

The fundamental science question of the IMT in VO_2 is whether it is a Mott or Peierls transition[35,36,37,38,39]. Here, we review the two theories before we discuss their relevance to VO_2. We start with the Hubbard Model and write down the Hamiltonian summed over each site, i, and spin $\sigma = [\uparrow, \downarrow]$:

$$\hat{H} = -t \sum_{i,\sigma} \left(\hat{c}^{\dagger}_{i,\sigma} \hat{c}_{i+1,\sigma} + \hat{c}^{\dagger}_{i+1,\sigma} \hat{c}_{i,\sigma} \right) + U \sum_{i} \hat{n}_{i\uparrow} \hat{n}_{i\downarrow}, \tag{1.2}$$

where $\hat{c}^{\dagger}$, $\hat{c}$ are fermion creation and annihilation operators respectively, $\hat{n}_{i\sigma} = \hat{c}^{\dagger}_{i,\sigma} + \hat{c}_{i,\sigma}$ is the spin-density operator, t the hopping parameter, which is calculated through an integral, and U the relative strength of the on-site repulsion between electrons.

The first test of the Hubbard Hamiltonian is a 1D chain of H atoms - in fact, this

is the only system that can be solved analytically. We can set U to 0 and neglect electron-electron on-site interactions. In a chain the s orbitals of each H atom will overlap and hybridize, which is the foundation of band theory (along with $U = 0$). Solving out the resulting bands from the configuration result in $E \propto k^2$, with band gaps at $ka = \pm\pi$, where a is the lattice spacing of the H atoms[40]. Each atom contributes one electron, filling the energy up to a value of $ka = \pm\pi/2$ in the ground state (half-filling). As per this model, half-filling will result in a metal, consistent with H atoms in a lattice at low T. However, as the atoms in the chain move further away, instead we would want to describe isolated atoms with insulating behavior. In this limit we take U to be non zero, such that $U/t >> 1$ and the electron orbitals do not hybridize. In this limit the Hubbard model predicts an antiferromagnetic insulator, as one would expect for a series of isolated H atoms.

1.1.1 A Mott transition

A Mott transition describes an insulator to metal transition as the temperature is increased due to the thermal effects causing the hopping energy t to become larger than on-site electron-electron repulsion U in the Hubbard Hamiltonian Eq. 1.2. Specifically, at low temperature a Mott insulator has such a large on-site repulsion due to electron-electron interactions that we take the $U/t >> 1$ limit with the Hubbard Hamiltonian and the material is an antiferromagnetic insulator. The Mott transition to the metallic state occurs at a threshold temperature, where the thermal en-

ergy of the electrons makes the hopping parameter larger than the on-site repulsion, $U/t << 1$. While these limits explain the two endpoint behaviors of the Mott transition, there is currently no rigorous solution to how a material behaves in the interim where $U/t \sim 1$[40]. For example, V_2O_3 is a canonical Mott insulator where the transition is truly the result of on-site electron repulsion being overcome by thermal effects, with a transition temperature of 165 K[1,41]. VO_2 may also exhibit a Mott transition above room temperature, at the unusually high temperature of 340 K. We note however, that it does not exhibit an antiferromagnetic insulating state.

1.1.2 A Peierls transition

Due to the SPT in VO_2, we must also consider a Peierls transition as an alternative driver of the IMT. A Peierls transition describes how a periodic lattice would exhibit metallic behavior, but a slight lattice distortion where the atoms dimerize would exhibits insulating behavior. A Peierls instability is the statement that a one-dimensional chain of equally spaced ions (or atoms) with one electron per ion is unstable; there will always be some distortion distance, δ, for which a gap in the energy bands will form at or near the Fermi surface, favoring the dimerized lattice[42]. A Peierls transition uses the assumptions of band theory, namely that the on-site electron repulsion is negligible.

In Fig. 1.4 we compare a 1D chain of atoms with equal spacing a to a 1D chain of atoms whose spacing alternates by $a + \delta$ and $a - \delta$. If every other atom is distorted by

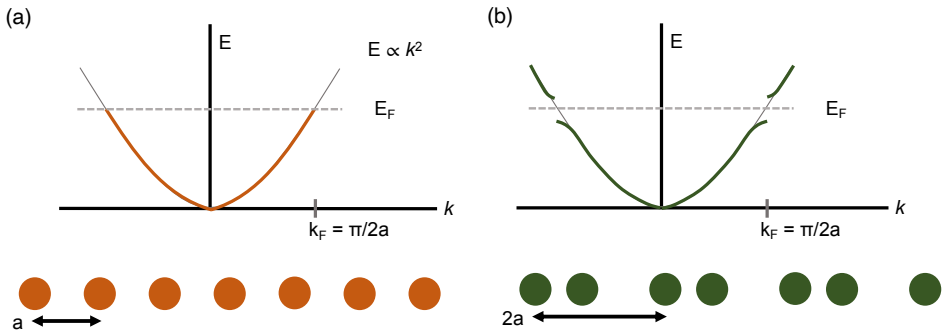

Figure 1.4: The resulting band energy from (a) an equally spaced chain of atoms and (b) a dimerized chain. The dimerized chain is known as the Peierls distortion and has a lower ground state energy due to the reduction of energy at the Fermi level. This distortion also creates a band gap at the Fermi level, resulting in an insulator.

δ (in the same direction, as shown in 1.4 (b)), now there are alternating intra-atomic spacing, so the *periodicity* of the chain is now $2a$. Based on band theory, band gaps will now form at $k(2a) = \pm\pi$, or $ka = \pm\pi/2$, and at this gap the band bends (lowering) slightly. Once again, if each atom contributes one electron, the band will fill up to $ka = \pm\pi/2$ in the ground state, filling to this gap. However, now because of the opening in the band structure there is a slight band bending and the same number of electrons will be at a lower energy, leading to the dimerized chain being more favorable[42]. In other words, the additional energy cost of the longer bond $(a + \delta)$ is less than the energy gained from the shorter bond $(a - \delta)$. However, it also means there is a band gap at the Fermi level and the dimerized chain will be insulating.

The band gap created through this distortion is typically quite small, therefore thermal excitation from some threshold temperature would allow electrons to jump the gap and fill states above and below the gap. In this case, the dimerization would

not lower the energy, and one would observe a periodic lattice and metallic behavior.

Current consensus of the transition

These two descriptions of the IMT seem at odds: a Mott insulator relies on high electron correlations to describe the transition as a function of temperature whereas the Peierls instability description assumes the electron interactions are negligible compared to the electron-atom interactions. While both of these frameworks have been known for decades, there is still debate as to which theory best describes the IMT VO_2. Ultimately, it seems that subtle aspects of both the structure and electron correlations are important to stabilizing the insulating phase, as more and more work details a Mott-Peierls crossover both theoretically[43,44,37,38] and experimentally[39,45,46].

Recent attempts to model the transition using density functional theory (DFT)[47,48] and dynamical mean-field theory (DMFT)[43,37,38] in VO_2 conclude the structural change is not only important, but required to accurately describe the transition. These frameworks use a dimer-Hubbard model where both the dimerization and strong electron correlations are considered.

Experimentally, disentangling the IMT and SPT is difficult, but possible, with some groups observing the IMT without a lattice change; observing a metallic monoclinic phase[49] or an insulating rutile phase[50]. Fratino *et. al.*[38] claim their framework of a doped, dimerized Mott insulator can encapsulate the metallic monoclinic phase observed experimentally[49].

On a final note, a prevailing theory is that the M2 phase to rutile is a true Mott insulator[48], with the transition from the room temperature monoclinic lattice to the M2 lattice requiring half of the V chains to dimerize, as shown in Fig. 1.3 (b).

1.2 Overview of this work

Having now described VO_2 and why it is of interest, both from a device and fundamental physics point of view, we may begin. The first stage of my research relied on growing thin film VO_2 with a high resistivity ratio across the transition, which was also sufficiently smooth to measure with scanning probe techniques. We optimized a growth recipe for VO_2 on both $TiO_2(001)$ and $Al_2O_3(0001)$, for which the results of the growth and final film characteristics are presented in Chapter 2.

We saw the potential to use non-contact atomic force microscopy (nc-AFM) to detect the Joule heating and local charge doping throughout the IMT with minimal current. In many 2-terminal geometries applying a bias results in a sufficiently large current that can locally heat the sample to its IMT temperature[27]. By using nc-AFM we aim to reduce the induced current and observe the material properties through the IMT. In Chapter 3 we overview the fundamentals of non-contact AFM; covering operation, data acquisition, and initial data analysis strategies. In Chapter 4 we go into more specific data analysis pertaining to the IMT in VO_2.

2

Molecular beam epitaxy growth of ultrathin VO_2 films

We use molecular beam epitaxy (MBE) to grow single-phase VO_2 films. MBE is a growth method used to grow material film layer-by-layer on a substrate. The 'molecular beam' aspect is achieved through a sufficiently high vacuum such that the mean

free path of atoms or molecules is on the order of 1 m; which is larger than the source to substrate distance, therefore the atoms from the source will not scatter. This creates an easily controllable beam of atoms or molecules from a source at the bottom of the vacuum chamber aimed at a substrate. By modulating the rate of sublimation the user can control the relative rates of different metals and very precisely deposit compounds layer-by-layer. The 'epitaxy' aspect of the name relies on the choice of substrate where the lattice structure of the material grown will align with the substrate lattice on which it is grown.

For already-gaseous materials, such as oxygen, the deposition method is altered slightly. Instead of controlling the deposition rate through the rate of sublimation, the set partial pressure of the gas is controlled. We use an oxygen plasma source to supply atomic oxygen. Molecular oxygen, or ozone can also be used, with molecular oxygen being less reactive and ozone being more reactive than atomic oxygen.

2.1 Substrates

Substrate choice is an important aspect of MBE growths since the deposited material will align with the substrate orientation to minimize the surface energy. The substrate and film thickness are important for VO_2 properties, such as the temperature, hysteresis, and sharpness of the transition, and even the resistivity ratio between the insulating and metallic state (RR_{IMT}). For example, when grown on $Al_2O_3(0001)$,

the IMT temperature is typically close to bulk, around 340 K, and when grown on $TiO_2(001)$ the IMT temperature is reduced to around 290 K, below room temperature.

Figure 2.1 summarizes the reported RR_{IMT}, IMT temperature, and IMT width for representative thin films grown on both $TiO_2(001)$ and $Al_2O_3(0001)$ substrates from literature at varying thicknesses. Notably, ultrathin VO_2 films grown on $TiO_2(001)$ have been well optimized, maintaining a RR_{IMT} of 10^3 in films around 10 nm thick using ozone molecular beam epitaxy (MBE)[20], and even in films as thin as 2 nm with RR_{IMT} around $10^{2.5}$ using both ozone MBE[20,51] and pulsed laser deposition (PLD)[52]. One obstacle to maintaining high RR_{IMT} in ultrathin VO_2 films on TiO_2 is Ti-V interdiffusion at the film-substrate interface, which has been shown to reduce both the magnitude and sharpness of the IMT[20,52,24]. To minimize Ti-V interdiffusion, groups have developed recipes to grow VO_2 with low substrate temperature of 120°C with a 200°C anneal[51], or 250°C with a 300°C anneal[20]. Even though these recipes aim to reduce Ti-V interdiffusion, 1.4-1.7 nm of interdiffusion can still be observed at the interface[20,51]. $TiO_2(001)$ is also prone to oxygen vacancies which can affect the IMT temperature and RR_{IMT} in VO_2[53]. Furthermore, VO_2 films 30 nm or thicker grown on $TiO_2(001)$ are known to crack due to thermal stress[18,19,20,21].

Looking at trends in VO_2 growths on $Al_2O_3(0001)$ in Fig. 2.1, we observe that there have been many VO_2 films thicker than 20 nm grown on $Al_2O_3(0001)$ with RR_{IMT} of 10^3 and even up to 10^4 using growth methods such as reactive-biased tar-

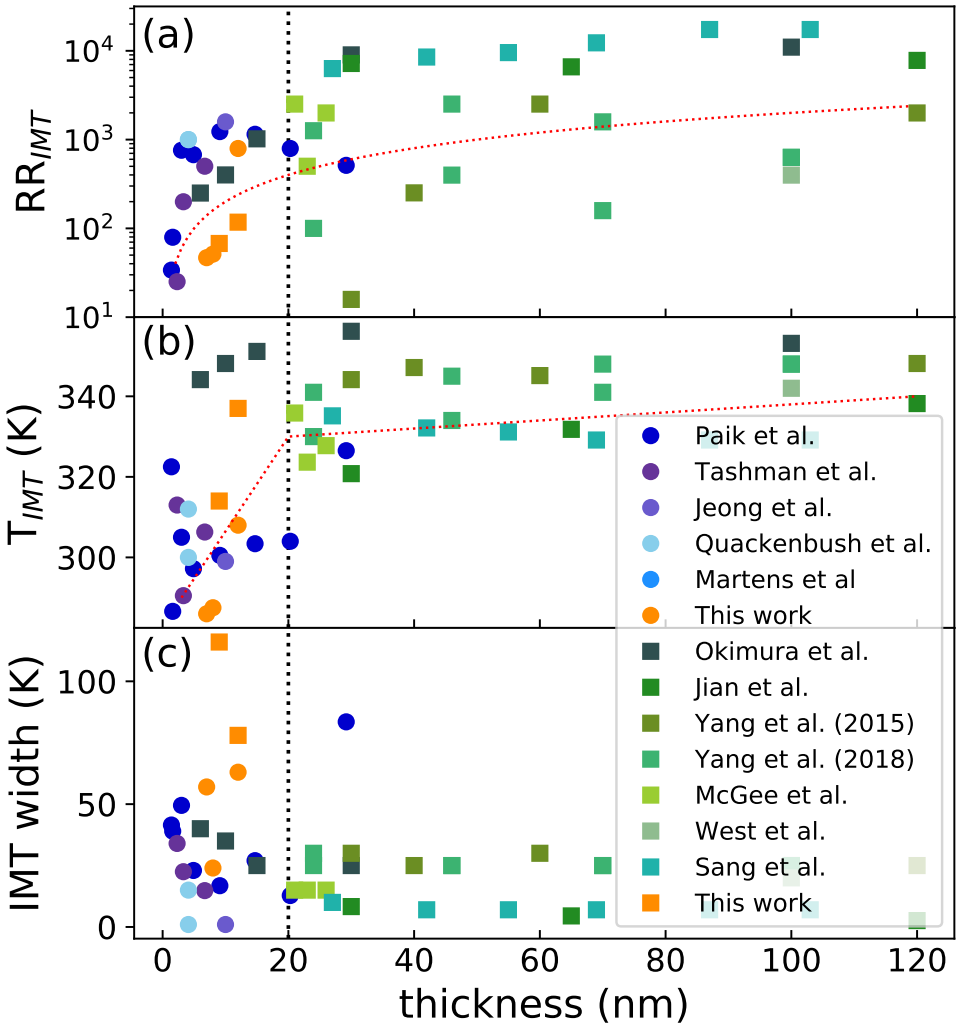

Figure 2.1: VO_2 thin films from literature showing thinner VO_2 films tend the reduce the reported RR between the insulating and metallic state measured through transport. Growths on TiO_2(001) are denoted with a circle, while growths on Al_2O_3(0001) are denoted with a square. The dotted black line denotes the ultrathin film cut-off of 20 nm. The dotted red lines are guides to the eye for the decreasing RR_{IMT} and T_{IMT} with film thickness.

get ion beam deposition (RBTIBD)[54,55], PLD[56], and magnetron-sputtering[57]. However, there has been little success in growing films thinner than 20 nm and observing a transition in transport measurements. Part of the reason growing ultrathin VO_2 on $Al_2O_3(0001)$ has been a challenge is the large lattice mismatch (4-9 %) with all orientations of VO_2[58,59] and island growth mode[22]. There is also a lattice symmetry difference between the film and substrate: $Al_2O_3(0001)$ has a hexagonal structure which creates a 3-fold rotational degeneracy with both phases of VO_2[60]. Furthermore, there are two in-plane orientations that have been observed, named the "on-axis" and "diagonal" growth modes[61]§. The two possible growth orientations, plus the 3-fold rotational symmetry make single-phase growth on this substrate a challenge[19,62]. Even still, many have grown VO_2 films on $Al_2O_3(0001)$ and observe a transition, as evidenced by Fig. 2.1[54,63,19,62,55,56,57,58]. Few papers have studied films as thin as 2 nm, and quantified the optical properties across the transition[22,23]. These studies also observe a decrease in both the T_{IMT} and transmission ratio between the insulating and metallic state in ultrafilms. In particular, only one previous study has achieved VO_2 ultrathin films on $Al_2O_3(0001)$ and measured transport, reporting RR_{IMT} of $10^{2.5}$ in a 6 nm film, grown using RBTIBD[54]. Here, we report a recipe using oxygen plasma MBE to grow a 12 nm VO_2 ultrathin film on $Al_2O_3(0001)$ and observe RR_{IMT} of 10^2 with IMT width of 63 K.

Ultimately, $Al_2O_3(0001)$ is a preferred substrate for VO_2 devices due to the avail-

§we show these growth modes in Fig. 2.6 and discuss them in more detail in Sect. 2.2.2

ability and ease to prepare wafers, plus it has a smaller dielectric constant and larger thermal conductivity than TiO_2[64]. It is also less prone to interdiffusion at the interface, and the IMT in VO_2 is less sensitive to oxygen vacancies in the substrate. Therefore, we would like to produce ultrathin VO_2 films on $Al_2O_3(0001)$ with similarly sharp and large RR_{IMT} characteristics as currently exists on $TiO_2(001)$. Here we present growth procedures for single-crystal VO_2 ultrathin films using oxygen plasma MBE on $TiO_2(001)$ with RR_{IMT} around 3 orders of magnitude and on $Al_2O_3(0001)$ that maintains a RR_{IMT} of 2 orders of magnitude.

2.2 Film growth and characterization

We use a *Veeco GENxplor* MBE with base pressure better than 10^{-9} Torr and an oxygen plasma source to generate atomic oxygen to grow VO_2 thin films. Using a calibrated quartz crystal microbalance (QCM) inside the chamber, we use V deposition flux of 1 $\times 10^{13}$ V atoms/(cm$^2\cdot$ s) during growth, comparable to the flux stated by both Paik *et al.*[20] and Tashman *et al.*[51]. For this V flux, we used an oxygen partial pressure of 2.4 $\times 10^{-6}$ Torr for all growths, which we determined produced single-phase VO_2 with high RR_{IMT} on $TiO_2(001)$

Fig. 2.2 overviews the results of all samples grown and characterized throughout this project. We find an important aspect to the correct V-O stochiometry is the ratio of O pressure to V flux. In Fig. 2.2 we plot the growth V flux and the O partial pres-

sure. We use the color to denote the the resulting film grown: orange for VO_2, purple for V_2O_5, and green for V_2O_3. The shape or the marker corresponds the electronic properties of the film as measured between 280 K and 360 K: circle for an observed IMT, upward triangle for high resistance and insulating, and downward triangle for low resistance and metallic. For samples that we did not perform transport measurements we indicate that with an 'x'. Using this plot we find a window with the V flux equal to 1×10^{13} V atoms/(cm^2· s) and O partial pressure of 2.4 $\times 10^{-6}$ Torr where we consistently grow samples with an IMT when measured between 280 K and 360 K.

Using this fixed V flux and O partial pressure, we grew a series of VO_2 thin films on TiO_2(001) and Al_2O_3(0001) at substrate temperatures ranging from 150°C to 400°C, with an additional 10 minute post-growth anneal at 300°C in the same oxygen partial pressure for samples grown below 300°C. We describe a total of 7 samples in detail, with each thickness and composition summarized in Table 2.1. We target a VO_2 film thickness of 10 nm, well below the thickness where cracking is observed[19,20], but thick enough that we expect large RR_{IMT}, even if there is film-substrate interdiffusion[24,51,63].

Once a film has been grown we remove the film from the chamber and characterize the thickness and roughness with x-ray reflectivity (XRR), the composition with x-ray diffraction (XRD), the surface morphology with tapping AFM in air, and the transport properties using a physical property measurement system (PPMS).

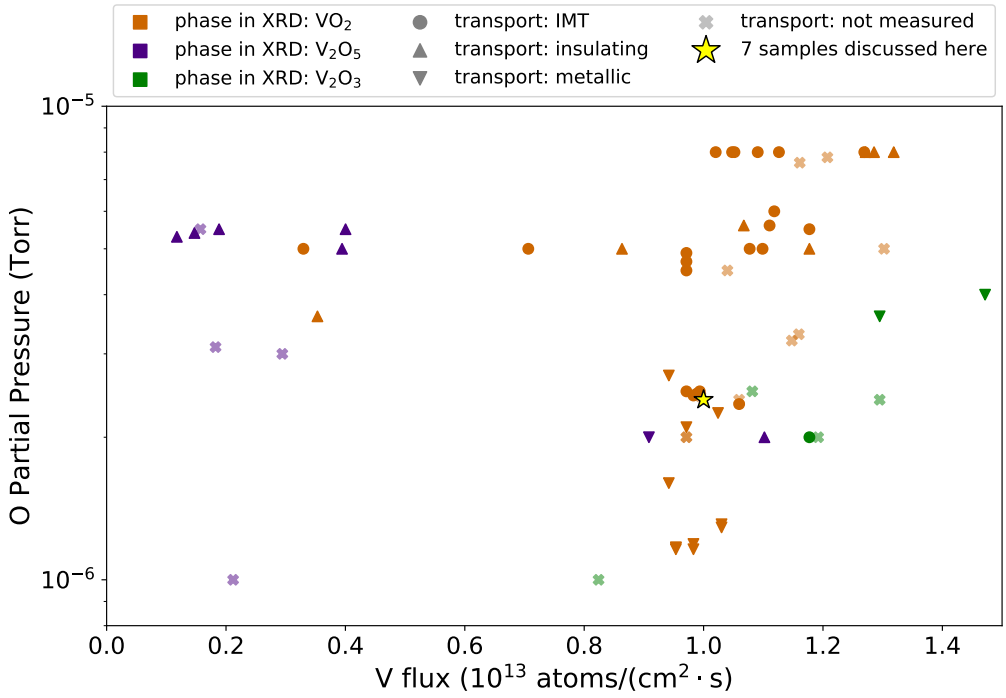

Figure 2.2: All ∼100 V-O films grown in our lab, plotted according to the V flux and O partial pressure during growth, and resulting phase from XRD overlayed with resulting transport. The color of the marker represents the phase determined through XRD: orange for VO_2, purple for V_2O_5 and green for V_2O_3. The shape of the marker represents the electronic transport properties between 280 K and 360 K: circle for an observed IMT, upward triangle for high resistance and insulating, and downward triangle for low resistance and metallic. We indicate samples without measured transport with an 'x'. The growth conditions of the seven samples studied in detail in this chapter is marked with yellow star. All seven samples were grown with the same V flux and O partial pressure, but the substrate temperature was varied, which is not indicated on this plot.

2.2.1 X-ray reflectivity (XRR)

We perform x-ray reflectivity (XRR) measurements and simulate XRR curves using GenX software[†] to determine film thickness, density, roughness, and any interface or surface layers[65]. The final film and total interface thickness are reported in Table 2.1. Based on the simulations, all film densities are within 20% of the expected bulk density of VO_2, and the density of the substrate-film interface or surface layers is within 30% of the bulk density of VO_2 (See Table 2.2), and all film thicknesses agree within a few nm of the target thickness of 10 nm. The sample grown at 400°C on Al_2O_3 had a particularly thick substrate-film interface of 4 nm, while all other samples had a corresponding film-substrate interface of 1 nm or less. The samples grown on TiO_2(001) at 275°C and 375°C, and the sample grown on Al_2O_3(0001) at 275°C all had a particularly thick ($\sim$ 4 nm) surface layer, likely a surface oxide from being exposed to air in a desiccator for $\sim$ 8 months before the XRR data was taken.

We use the film and interface thicknesses extracted from our XRR simulations to verify the V flux used during deposition. The V flux is calculated from adding the film and interface thickness, weighted by the densities relative to the bulk density of VO_2, to determine the number of V atoms in the sample, then divided by the known deposition time. The calculated V flux of each deposition falls within 2 $\times 10^{12}$ V atoms/(cm$^2\cdot$ s) of the target flux of 10^{13} V atoms/(cm$^2\cdot$ s).

[†] https://aglavic.github.io/genx/

substrate	growth T (°C)	film + interface thickness (nm)	XRD peak position (°)	out-of-plane spacing (Å)	bulk monoclinic spacing* (Å)	monoclinic mismatch %	bulk rutile spacing** (Å)	rutile mismatch %
$TiO_2(001)$	150†	12 + 2	65.43 ± 0.01	1.425 ± 0.006	1.438	-0.9 ± 0.4	1.428	-0.2 ± 0.4
$TiO_2(001)$	275†	8 + 4	65.712 ± 0.008	1.420 ± 0.003	1.438	-1.3 ± 0.2	1.428	-0.6 ± 0.2
$TiO_2(001)$	375	7 + 4	65.350 ± 0.009	1.427 ± 0.004	1.438	-0.8 ± 0.3	1.428	-0.1 ± 0.3
$Al_2O_3(0001)$	275†	11 + 4	–	–	–	–	–	–
$Al_2O_3(0001)$	325	10 + 1	39.48 ± 0.01	2.281 ± 0.005	2.263	0.8 ± 0.2	2.277	0.2 ± 0.2
$Al_2O_3(0001)$	375	9 + 1	39.853 ± 0.017	2.260 ± 0.007	2.263	-0.1 ± 0.3	2.277	-0.8 ± 0.3
$Al_2O_3(0001)$	400	12 + 4	39.942 ± 0.023	2.25 ± 0.01	2.263	-0.6 ± 0.4	2.277	-1.2 ± 0.4

Table 2.1: Sample thicknesses determined from XRR simulations with any fit interface layer thicknesses, XRD fit peaks, and the corresponding out-of-plane lattice mismatch for monoclinic and rutile phase. All measured out-of-plane lattice mismatch values are less than or about 1%, so it is difficult to determine the phase of the lattice from the XRD alone.

†Samples were annealed to 300°C after V deposition for 10 minutes in the same oxygen partial pressure as V deposition.

*The monoclinic orientation we consider for each substrate is $VO_2(40\bar{2})_M||TiO_2(001)$ and $VO_2(020)_M||Al_2O_3(0001)$. Bulk lattice constants reported from the room temperature measurements of Rogers[5].

**The rutile orientation we consider for each substrate is $VO_2(002)_R||TiO_2(001)$ and $VO_2(0\bar{2}0)_R||Al_2O_3(0001)$. Bulk rutile lattice constants are reported from the 400 K measurements of Rogers[5].

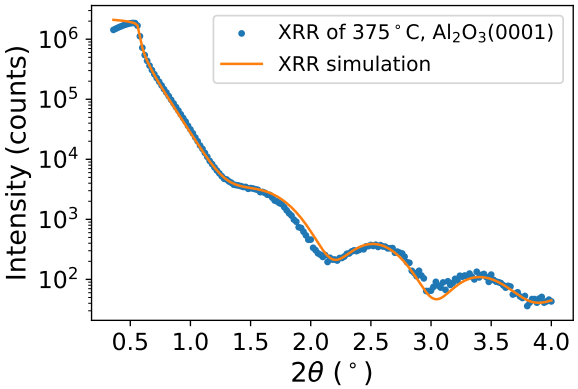

Figure 2.3: XRR data from the sample grown at 375 °C on Al_2O_3(0001) with the GenX simulation showing acceptable agreement. The simulation corresponds to film parameters tabulated in Table 2.2.

We report the full XRR simulation parameters for each sample, and show a representative fit for the sample grown on Al_2O_3(0001) at 375°C in Fig. 2.3. Fit parameters for each sample include two background offsets: the initial and background intensity, two parameters for the substrate: density and roughness, and three properties per additional layer: thickness, density and roughness. In the Table 2.2 we show the fit parameters for each sample, as well as specify where any interfacial layers are located: either at the film-substrate interface or on the surface of the film (i.e. the film-air interface).

The substrate density of Al_2O_3 is consistently close to the bulk value in the fits. However, the density of TiO_2 in the fits is at up to 33% lower than bulk TiO_2 in the samples grown at 150°C and 275°C. The density XRR is sensitive to is the scattering length density, which is related to the electron density, not the mass density.

sample substrate, growth T	substrate density ($FU/Å^3$)	film thickness (nm)	film density ($FU/Å^3$)	interface thickness (nm)	interface density ($FU/Å^3$)	surface thickness (nm)	surface density ($FU/Å^3$)	weighted thickness (nm)
TiO_2, 150°C	0.0287	12	0.03535	1.2	0.0390	0.6	0.0640	14.4
TiO_2, 275°C	0.0216	8	0.0294	–	–	4	0.0238	9.9
TiO_2, 375°C	0.0327	7	0.0348	–	–	4	0.0222	9.4
Al_2O_3, 275°C	0.0233	11	0.0284	–	–	4	0.0235	12.6
Al_2O_3, 325°C	0.0233	10	0.0382	0.6	0.0308	–	–	12.2
Al_2O_3, 375°C	0.0233	9	0.0366	0.8	0.0280	–	–	10.9
Al_2O_3, 400°C	0.0271	12	0.0398	4	0.0380	–	–	18.7

Table 2.2: Summary of the eight relevant XRR fitting parameters: substrate density and roughness, film density, roughness, and thickness, and any interface density, roughness, and thickness. The density of interest for XRR is the scattering length density which is related to electron density as opposed to the mass density. The density parameter within the simulations is the chemical formula unit per $Å^3$ ($FU/Å^3$), which is related to the unit cell size and mass density. Bulk densities: VO_2: 0.0332 $FU/Å^3$, TiO_2: 0.0327 $FU/Å^3$, Al_2O_3: 0.0233 $FU/Å^3$. The non-trivial surface interface layer is likely an oxide on the surface, due to those samples having XRR data taken months after growth.

Therefore, even though the simulations fit to a lower density in TiO_2, this points to a decrease in electrons in the substrate, which may indicate we have interdiffusion between our sample and substrate.

When creating the model, we place the interface between the substrate and film, with a density near but below that of the film, then start the fitting procedure. In some cases the fitting reduced the film thickness and the density while increasing the interface density and thickness, to a point where the interface more closely matched the density of the film than the film layer. In this case we took the interface layer to be located on the surface of the film, and assume a negligible substrate-film interface. For the film grown at 150 °C on TiO_2 the fit required the inclusion of both interfacial layers.

2.2.2 X-ray diffraction (XRD)

We use x-ray diffraction (XRD), measured at room temperature, to determine the structural characteristics of the samples. The results for each sample are shown in Fig. 2.5. Peaks in the XRD correspond to constructive interference of x-rays incident at angle θ from the surface that are transmitted and reflected along planes of atoms parallel to the surface. The constructive interference is described by Bragg's law: $n\lambda = 2d\sin\theta$, where n is the diffraction order, λ is the x-ray wavelength (we use Cu K-α radiation with $\lambda = 1.5406$ Å), d is the spacing of the planes of atoms, and θ is the reflected angle relative to the surface, as shown in Fig. 2.4. Thus, a peak in intensity at a particular angle of incidence will correspond to a plane spacing where the constructive interference is the strongest. 2θ is the independent variable for this measurement schema; both the source and the detector are positioned such that they have the same incident angle with respect to the surface, which is then swept from 4° to 55°. The intensity is then collected as a function of 2θ, where 2θ refers to the angle of the detector with respect to the through-line of the source.

The substrate will also be detected in this measurement (labelled in both panels in Fig. 2.5) and is typically used as a calibration since the orientation is known and there is no strain to alter the plane spacing from known bulk values. The substrate has effectively infinite atomic planes for constructive interference which will result in a very sharp and intense peak. A thin film however, has fewer planes contributing to

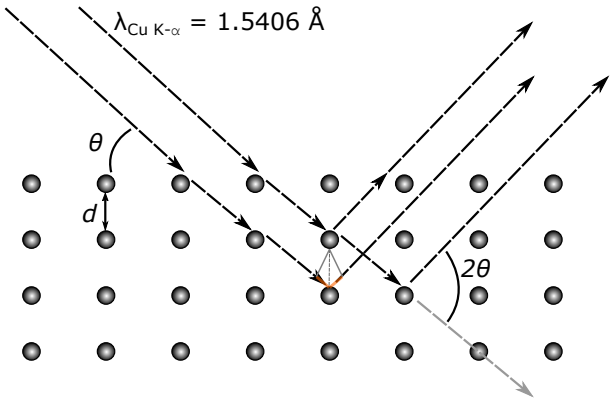

Figure 2.4: Schematic of the constructive interference measured during a typical XRD scan. The orange dashed lines are the path length difference, each one equal to $d \sin\theta$.

the constructive interference which results in a broader, less intense peak.

We note that some reflections predicted by Bragg's law are forbidden. Specifically, $VO_2(001)_R$ is forbidden because the V atoms in VO_2 have a body-centered tetragonal structure and due to the symmetry of the O atoms within the lattice. The additional V atom at the center of the unit cell adds an atomic plane between the planes at the top and bottom of the unit cell and thus we would not find a peak corresponding to 2.8557 Å lattice spacing. Because there are two planes of atoms per unit cell, the plane spacing one would expect to measure is 2.8557 Å/2 = 1.428 Å, corresponding to $VO_2(002)_R$ (Fig. 1.2 (a)). For the same orientation but in the monoclinic phase, a_M = 5.7529 Å[5], but there are now 4 atomic planes per unit cell (Fig. 1.2 (b)), resulting in an expected plane spacing of 1.438 Å. Rigorously, the forbidden reflections occur when the structure factor of a specific orientation, (HKL), goes to zero. The structure

factor for the (HKL) reflection is:

$$F_{\mathrm{HKL}} = \sum f_j \exp[-2\pi i \times (Hx_j + Ky_j + Lz_j)], \tag{2.1}$$

where the sum is over all atoms in the unit cell labelled by j, f_j is the atomic form factor (different for each atom), and x_j, y_j, and z_j are the fractional coordinates of the atoms within the unit cell.

Previous work on $TiO_2(001)$ substrates has shown that VO_2 thin films can maintain the rutile structure from the growth temperature down to room temperature[17]. Specifically, we expect $VO_2(001)_R$ to form, adopting the lattice structure and orientation from the substrate. However, due to the structure factor of this lattice the first peak we would expect to see in the XRD corresponds to $VO_2(002)_{\mathrm{R}}$ with a plane spacing of 2.8557 Å/2 = 1.428 Å[5]. $VO_2(40\bar{2})_{\mathrm{M}}$ is the corresponding film orientation in the monoclinic phase which has a plane spacing of 1.438 Å. Fig. 2.5 (a) shows the XRD data for each sample grown on $TiO_2(001)$, with the bulk peak positions for both $VO_2(002)_{\mathrm{R}}$ and $VO_2(40\bar{2})_{\mathrm{M}}$ labeled. For each sample we fit the peak position and extract the out-of-plane lattice spacing. We notice the non-monotonic behavior of the peak position with substrate temperature. This may be due to the sensitivity of VO_2 film growth on the substrate preparation of $TiO_2(001)$[52]. For example, the sample grown with the substrate temperature at 275° may have had a different substrate terrace sizes than the other two samples shown here.

Using this measured out-of-plane spacing (d_{XRD}), and bulk plane spacing ($d_{(002)_R}$ or $d_{(40\bar{2})_M}$) we calculate the out-of-plane lattice mismatch for both the monoclinic and rutile phase on $TiO_2(001)$ using

$$\text{monoclinic mismatch} = \frac{d_{\mathrm{XRD}} - d_{(40\bar{2})_M}}{d_{(40\bar{2})_M}} \tag{2.2}$$

and

$$\text{rutile mismatch} = \frac{d_{\mathrm{XRD}} - d_{(002)_R}}{d_{(002)_R}} \tag{2.3}$$

respectively. Based on the calculated lattice mismatch of each phase, we find that all growths on TiO_2 are more consistent with VO_2 in the rutile phase than the monoclinic phase. However, because the films are thin, the peak is very broad which makes it difficult to fit the exact position in 2θ. Furthermore, all the calculated out-of-plane mismatch values are close to or less than 1%, so the phase can not be conclusively determined from XRD measurements alone.

When depositing VO_2 on $Al_2O_3(0001)$ the elevated substrate temperature favors the rutile phase during deposition. However as the film is cooled through the IMT and SPT temperature the VO_2 lattice transitions to the monoclinic phase. Therefore when thinking about strain, we must consider how the rutile phase will align with the $Al_2O_3(0001)$ lattice during growth, but acknowledge that the film is expected to be monoclinic phase at room temperature, which may affect room temperature strain

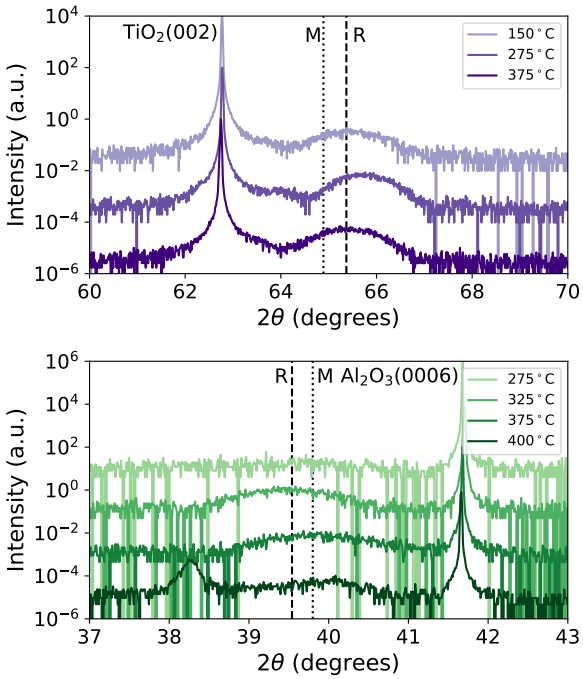

Figure 2.5: XRD of the films show that VO_2 crystallizes at all temperatures studied here on TiO_2 but only at or above 325°C on Al_2O_3. (a) The samples grown on TiO_2 (001) and the bulk VO_2 rutile (002) and monoclinic ($40\bar{2}$) peaks denoted with a dashed and dotted line respectively. The variable VO_2 peak position may be due to differences in the substrate surface after preparation[52]. (b) The samples grown on Al_2O_3(0001) with the VO_2 rutile ($0\bar{2}0$) and monoclinic (020) similarly denoted. Curves are offset by a factor of 100 for clarity. The peak at 38.1° in the 400°C growth corresponds to Au (111) because the XRD for this film was taken after gold contacts had already been deposited, but should not affect the VO_2 peak.

considerations.

In Fig. 2.6, we show schematically both the "on-axis" and "diagonal" growth orientations of rutile VO_2 on $Al_2O_3(0001)$[61]. Using the bulk crystal values for the rutile phase (measured at 400 K[5]), we calculate a compressive 2.4% strain on c_R and tensile 4.5% strain on a_R for the on-axis growth, $VO_2[100]_R \| Al_2O_3[2\bar{1}\bar{1}0]$. We calculate the strain for the diagonal growth mode along $VO_2[101]_R \| Al_2O_3[10\bar{1}0]$ to be -2.1 %, using a supercell of three VO_2 lattices to two Al_2O_3 lattices along that diagonal 'axis' alignment (specifically the dashed line in Fig. 2.6 (b)). Even with this high strain, the $VO_2(0\bar{1}0)_R \| Al_2O_3(0001)$ is consistently observed[60,57,62], with either $VO_2[100]_R \| Al_2O_3[2\bar{1}\bar{1}0]$ or $VO_2[101]_R \| Al_2O_3[10\bar{1}0]$[61].

In our VO_2 samples grown on $Al_2O_3(0001)$ we observe peaks in the XRD corresponding to $VO_2(020)_M$ (or $VO_2(0\bar{2}0)_R$ in the rutile phase), in agreement with results from literature. We find $VO_2(020)_M$ crystallizes only at and above 325°C (Fig. 2.5 (b)), consistent with, and slightly below the previously reported minimum growth temperature of 350°C[55]. Of the three samples that crystallized on $Al_2O_3(0001)$, we once again fit the peak position to calculate the out-of-plane lattice parameter and determine the out-of-plane lattice mismatch of the monoclinic (rutile) phase using $d_{(020)_M}$ ($d_{(0\bar{2}0)_R}$) for the bulk plane spacing. Based on the resulting mismatch, we predict that the two higher temperature growths are in the monoclinic phase at room temperature, and we can not determine the phase of the VO_2 films grown at 275°C due to there being no peak in the XRD. Interestingly, the sample grown at 325° is more consis-

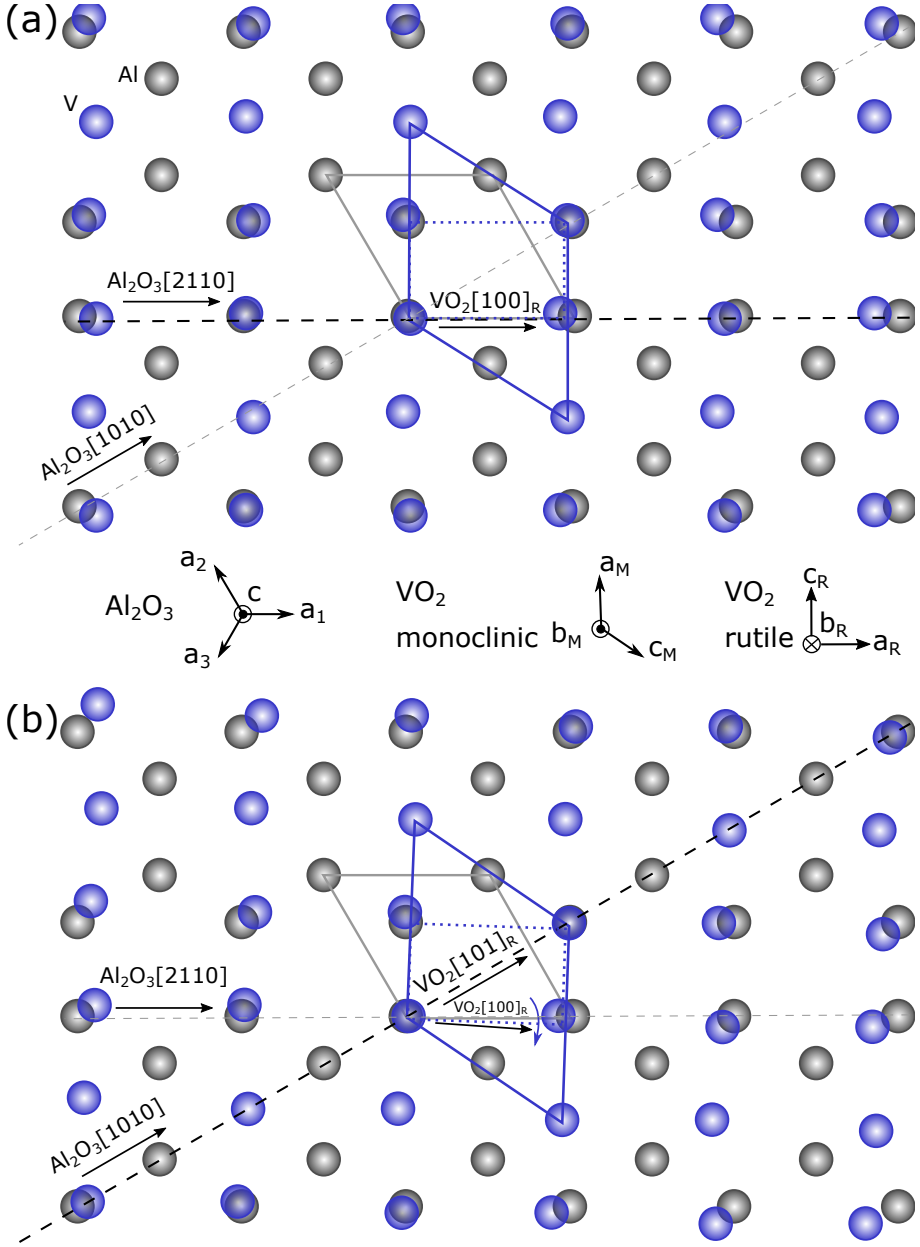

Figure 2.6: View along $VO_2[010]_M$ of the top-most layer of Al atoms (grey) and a single layer of V atoms (blue) in the monoclinic VO_2(020) orientation. The unit cell of Al_2O_3 is shown in grey, the unit cell of monoclinic VO_2 in solid blue, and the equivalent rutile unit cell is shown in dotted blue. The dark dashed line highlights which axes are aligned between Al_2O_3 and VO_2 in each case. (a) $VO_2[100]_R \| Al_2O_3[2\bar{1}\bar{1}0]$ alignment; on-axis growth. (b) $VO_2[101]_R \| Al_2O_3[10\bar{1}0]$ alignment; diagonal growth[61]. Panel (b) corresponds with a 2.16° (2.06°) rotation of V atoms clockwise from panel (a) in the monoclinic (rutile) phase.

tent with the rutile phase, however, we cannot determine the structure for this sample based on XRD alone. Similar to our VO_2 thin film growths on TiO_2, we need transport to confirm these phases. We could not determine the in-plane orientation using reciprocal space maps (RSM) because the film too thin and we could not detect an off-axis peak within the noise.

2.2.3 Measuring the IMT with transport

To quantify the IMT temperature, width, and hysteresis we use a physical property measurement system (PPMS) to measure the resistance as we sweep the temperature between 250 K and 370 K at $\pm$ 2.5 K/min. We deposited contacts in a van der Paaw geometry using an electron beam evaporator and a cross-shaped mask. 5 nm of Cr is deposited as a wetting layer before 100 nm of gold is deposited. The sample grown at 400 °C on Al_2O_3 used Ti as a wetting layer instead. The contacts are 2 - 2.5 mm apart, depending on the sample. Within the PPMS, we use an AC current of 1 μA, at either 9.16 Hz or 15.26 Hz. The transport for each sample is shown in Fig. 2.7, showing the that largest IMT occurs at the lowest growth temperature on TiO_2(001). On Al_2O_3(0001) we observe a broad, two order of magnitude transition for the film grown at 400°C, and less than two order of magnitude transition for the film grown at 375°C.

We quantify the IMT properties of each sample by taking the first and second derivative of the log of the resistance with respect to temperature. We establish the

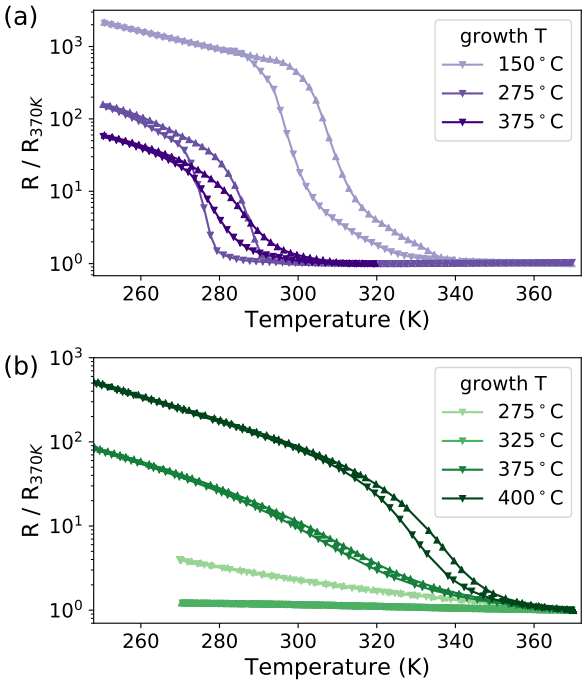

Figure 2.7: (a) Transport of films grown on TiO_2(001) and (b) on Al_2O_3(0001), with lower substrate temperature corresponding to lighter colors. All growths on TiO_2 show a transition below room temperature, and only 2 films on Al_2O_3 show a transition, both of which occur above room temperature. ▼ symbols refer to the down sweep, ▲ refer to the up sweep.

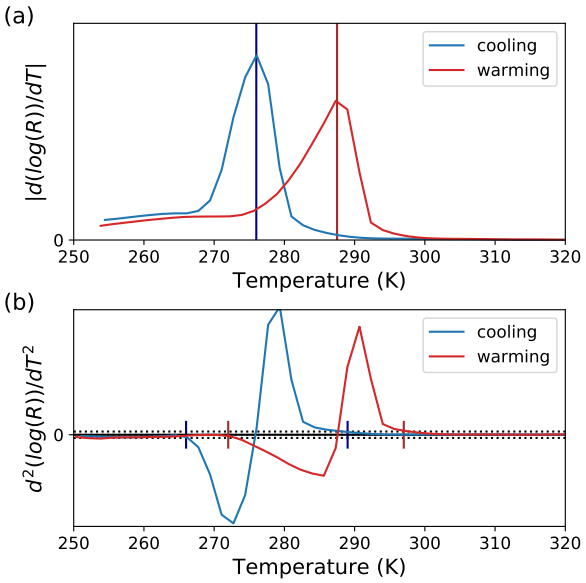

Figure 2.8: (a) Representative first derivative of the log of the resistance, showing the IMT temperatures of the cooling (blue) and warming (red) transport for the sample grown at 275°C on TiO_2. (b) The second derivative of the log of the resistance with the start and end of the transition marked by vertical lines: dark blue for cooling, dark red for warming[51]. We use a window around zero equal to 5% of the maximum double derivative value (shown in dotted lines) to determine when the double derivative is zero. We use the resistance at the corresponding start and end of the transport to calculate the RR.

IMT temperature by fitting the peak in the first derivative (i.e, $d(\log(R))/dT$, as shown in Fig. 2.8(a)). We then use the second derivative to determine the start and end point of the transition based on where the second derivative goes to 0[51] . We use a window around zero equal to 5% of the maximum of the double derivative to determine when the curves are consistent with zero. In Fig. 2.8 (b) we show the start and end point of the warming and cooling sweeps marked with a dark red and dark blue line respectively. We then take the ratio of the resistance at the start and the end of the transition, as defined by the IMT width, to calculate $\mathrm{RR_{IMT}}$.

We perform this fitting for both the warming and cooling sweeps and present the IMT temperature (T_{IMT}), IMT width, and RR_{IMT} in Table 2.3, where the error in the IMT width comes from differences in warming and cooling, and the error in RR_{IMT} comes from uncertainty in the endpoints of the double derivative due to noise in the data. For the sample grown on $Al_2O_3(0001)$ at 275°C there were no peak in the first derivative, consistent with no IMT, and for the sample grown at 325°C there was a broad peak in the first derivative, but the second derivative was flat within the noise, meaning there is no meaningful transition.

substrate, growth T	T_{IMT} (K) (warming)	T_{IMT} (K) (cooling)	IMT width (K)	$\log_{10}(RR_{IMT})$
TiO_2, 150°C	308	296	63 ± 3	2.90 ± 0.05
TiO_2, 275°C	287.5	275.5	24 ± 2	1.71 ± 0.02
TiO_2, 375°C	286	278	57 ± 4	1.67 ± 0.05
Al_2O_3, 275°C	insulating ($dR/dT < 0$) at all measured T			
Al_2O_3, 325°C	no measurable transition			
Al_2O_3, 375°C	314	307	116 ± 4	1.83 ± 0.03
Al_2O_3, 400°C	337	329	78 ± 4	2.07 ± 0.03

Table 2.3: Summary of film transport properties studied in this work. For growth on $TiO_2(001)$ we reproduce ultrathin films with high RR_{IMT}. We produce ultrathin VO_2 films $Al_2O_3(0001)$ with RR of 10^2. The sample grown on $Al_2O_3(0001)$ at 325°C showed a broad peak in the first derivative but only noise in the second derivative, and so we determine it has no measurable transition.

The two samples grown on $TiO_2(001)$ at higher temperatures showed an IMT below room temperature, consistent with the findings from XRD. However the film grown at 150°C with a 300°C anneal on $TiO_2(001)$ showed a IMT just above room temperature at 302 K. Based on transport, this sample is mid-transition at room temperature, and so may contain both monoclinic and rutile domains. The 300°C anneal

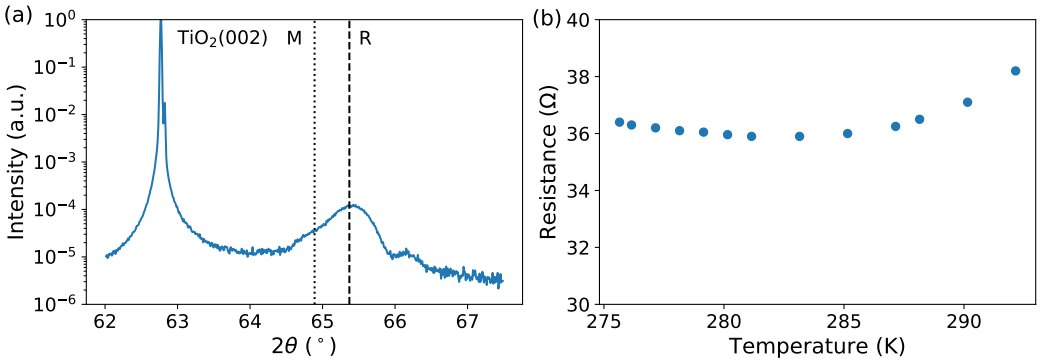

Figure 2.9: (a) XRD and (b) transport of a sample that was deposited at 150°C on $TiO_2(001)$ with the same V flux but had no post-growth anneal. Based on the XRD data, the sample crystallized rutile VO_2, but according to transport does not exhibit a transition down to 275 K.

was critical in producing a film with a transition, in agreement with Paik *et al.*[20]. We grew a second film at 150°C, not reported in Table 2.1, but without a post-growth anneal. As shown in Fig. 2.9, this sample showed a peak in the XRD where one would expect a $VO_2(002)_R$ peak, however no transition was observed in the transport.

On $Al_2O_3(0001)$, only films grown at the highest two substrate temperatures showed an IMT, both above room temperature. The transport shows the sample grown at 275° is insulating, with $dR/dT < 0$, down to at least 270 K. The sample grown at 325 K shows a very broad and shallow peak in the first derivative, with insulating behavior above 325 K and metallic behavior below. This is consistent with the room temperature XRD results, where out-of-plane lattice mismatch for the rutile phase was less than the mismatch to the monoclinic phase. However, there was no significant second derivative, and so we do not consider this sample to have a transition.

2.2.4 Atomic force microscopy (AFM): topography

To determine the surface topography and roughness of each film, we use atomic force microscopy (AFM) operating in tapping mode in air. We show a representative 500 × 500 nm^2 topography for each sample in Fig. 2.10. Panels (a)-(d) shows the AFM topography for samples grown on Al_2O_3(0001) at (a) 275°C, (b) 325°C, (c) 375°C, and (d) 400°C. Similarly, Panels (e) - (g) show the AFM topography for samples grown on TiO_2(001) at (e) 150°C, (f) 275°C, and (g) 375°C. All films have a root-mean-square (rms) roughness less than 2 nm. We use these topographies to estimate the characteristic domain size within each sample. To determine the average domain size in our films we take three line cuts through the image, and find the average grain width, shown in panel (h). The peak-to-peak roughness of each sample seems to indicate lower substrate temperature produces rougher films. The domain size on the other hand, does not seem to follow a trend with substrate temperature during growth.

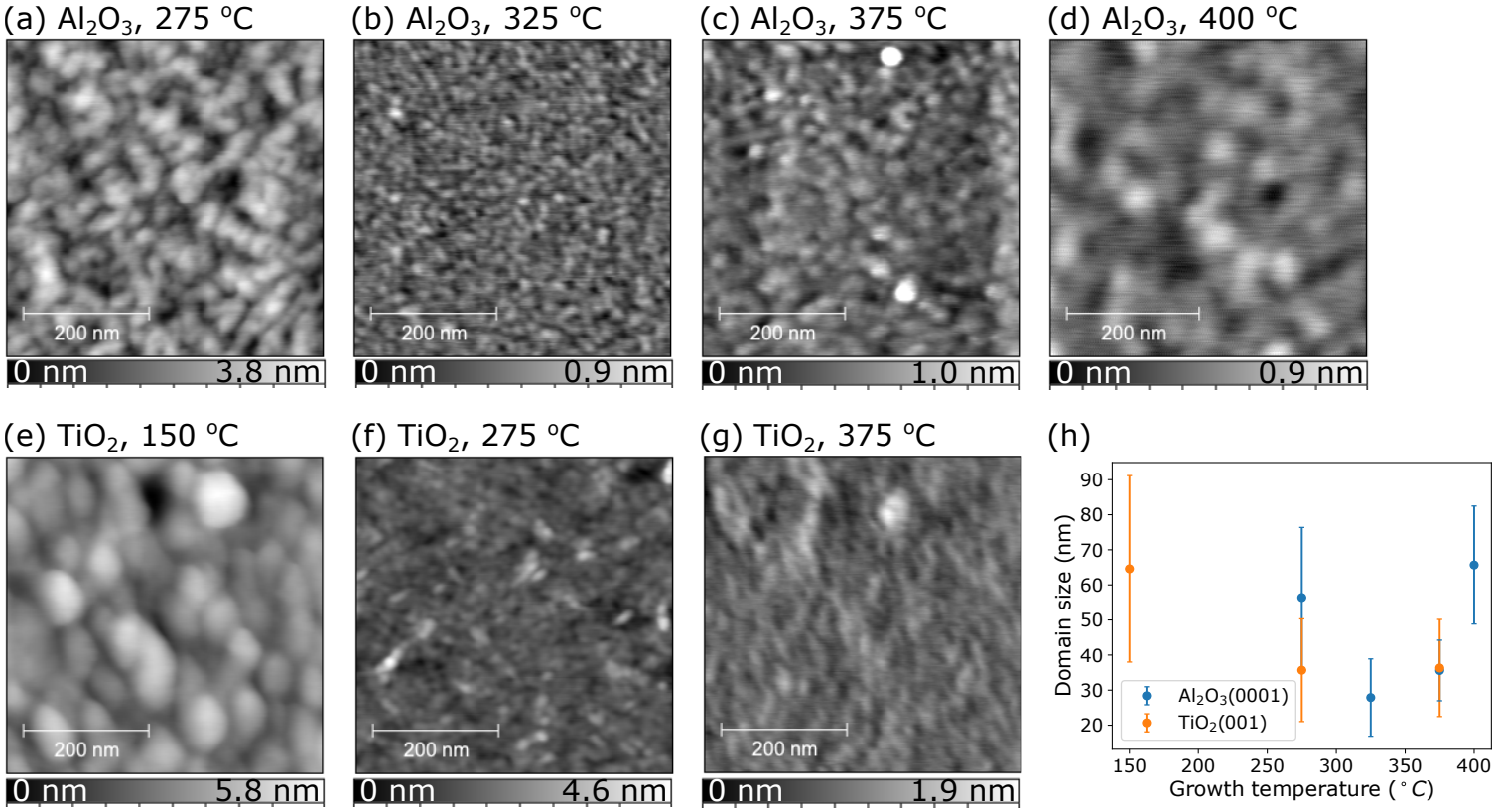

Figure 2.10: AFM topography of all seven samples studied here. (a)-(d) AFM topography of samples grown on Al_2O_3(0001) at (a) 275°C, (b) 325°C, (c) 375°C and (d) 400°C. (e)-(g) AFM topography of the samples grown on TiO_2(001) at (e) 150°C, (f) 275°C, and (g) 375°C. (h) Domain size extracted from line cuts for each sample plotted against the growth temperature. We see no significant trend with growth temperature within these samples.

2.3 Conclusion

We confirm that the best recipe used here for growing VO_2 on $TiO_2(001)$ is at the lowest substrate temperature; 150°C with a 10 minute, 300°C anneal in oxygen to produce a film with an almost three order of magnitude transition, IMT width of 63 K, and low rms roughness.

Finally, we confirm that ultrathin VO_2 films can be stabilized on $Al_2O_3(0001)$ that maintain an RR_{IMT} of at least 10^2. Interestingly, the film grown at 375°C, which has no measurable out-of-plane mismatch, has a IMT temperature of 314 K, reduced by 25 K from bulk, while the sample with higher out-of-plane mismatch (-0.2%) has a warming IMT temperature of 337 K, closer to the bulk IMT of 340 K. This points to the difficulty of predicting the effect of out-of-plane lattice parameter on the IMT temperature in $VO_2(010)_M$ oriented films, and the potential importance of measuring the in-plane strain.

We have described a growth technique using oxygen plasma MBE to grow single-phase VO_2 ultrathin films 12 nm thick on $TiO_2(001)$ with RR_{IMT} around 3 orders of magnitude and IMT width of 63 K. We reproduce the best films on $TiO_2(001)$ from literature and extend the lower bound of the deposition temperature of continuous growth to 150°C. Similarly, we grow a 12 nm VO_2 film on $Al_2O_3(0001)$ using oxygen plasma MBE with a two orders of magnitude RR_{IMT} and IMT width of 78 K. Additionally, we grow an ultrathin, 9 nm thick VO_2 film on $Al_2O_3(0001)$ with a warming

IMT temperature of 314 K and a transition width greater than 100 K. We develop a growth recipe using MBE to stabilize ultrathin VO_2 films on $Al_2O_3(0001)$ with a measurable electronic transition.

3

Non-contact atomic force microscopy

Non-contact atomic force microscopy (nc-AFM), is a nanoscale measurement technique that utilizes an oscillating probe to detect forces between the probe and a sample. The three common probe geometries include a silicon cantilever either in a horizontal or vertical geometry, or a qPlus sensor. For all 3 geometries the probe is

oscillated at its resonant frequency, f_0, and the response of the probe's frequency and amplitude are measured.

Here we use a qPlus sensor for its ease of construction, calibration, and use. A qPlus sensor uses a high-Q factor quartz tuning fork with one prong glued to a post, with the other prong free to oscillate. A metallic tip is glued to the oscillating prong and is used to detect tip-sample forces or current. Typical resonant frequencies are on the order of 10s of kHz with spring constant $\sim$ 1000s N/m. The high Q allows for high signal-to-noise within the measurement. Oscillations of the probe are detected through the piezoelectric signal generated by the quartz prong[66].

3.1 Geometry and Terms

Before diving into derivations, we first give a general overview of the basic geometry (Fig. 3.1) and variables (Table 3.1) we'll use in later sections. In Fig. 3.1 we schematically show the feedback in two operation modes: (a) constant drive mode and (b) constant amplitude mode. A red box denotes a fixed variable and green box denotes a varying variable. All boxed variables are recorded within the controller software[‖].

The probe is oscillated by a piezo which is driven an AC voltage, V_{drive} at frequency f. A qPlus probe detects the mechanical oscillation via the voltage signal generated through the piezo electric effect of the quartz[66]. The qPlus probe therefore requires two electrodes on the prong that span the length of the prong to detect the voltage

[‖]We use RHK's R9 Software.

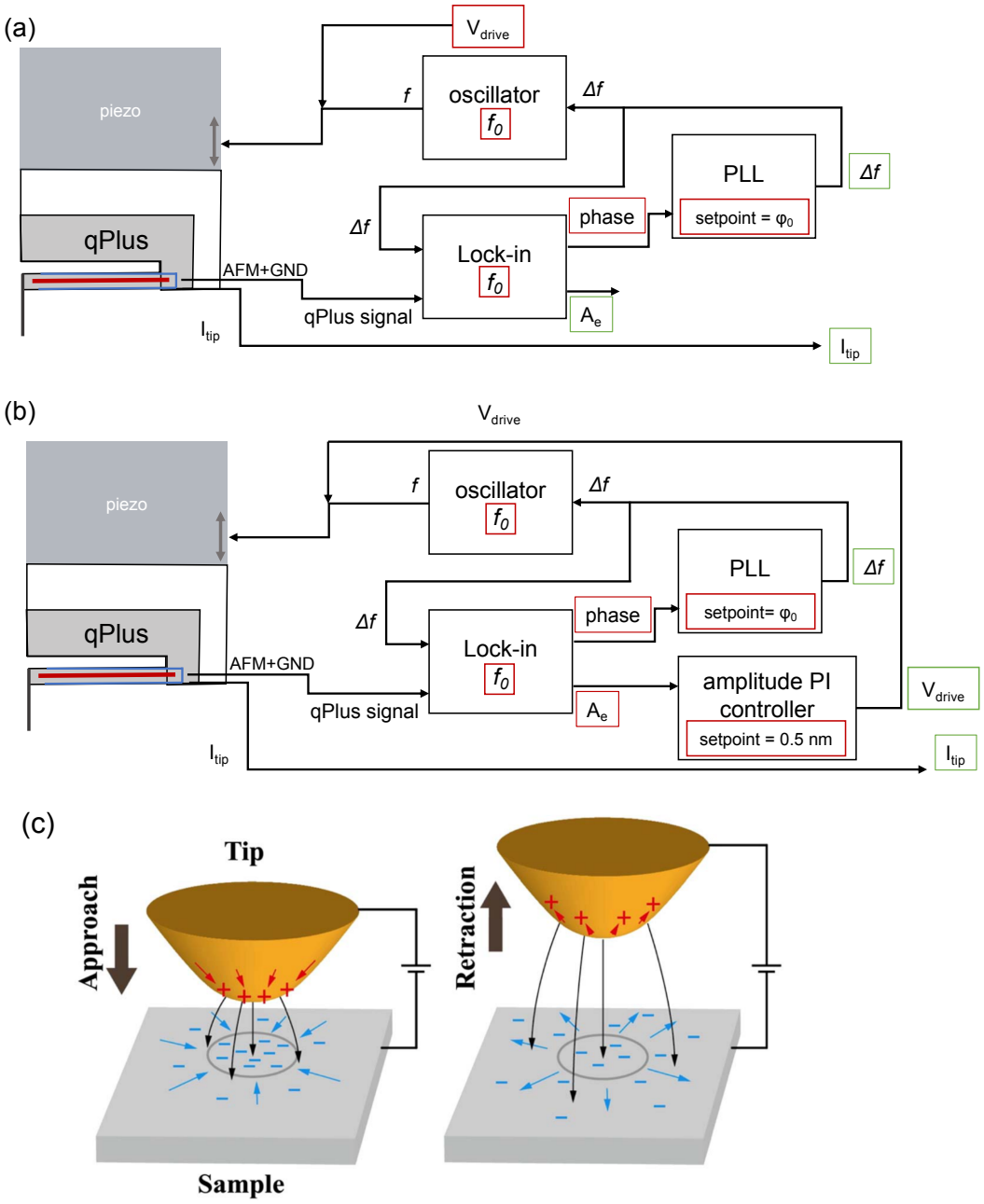

Figure 3.1: Schematic of nc-AFM operation using a qPlus sensor in (a) constant drive mode and (b) constant amplitude mode. All recorded variables are in either a red or green box. A red box denotes a fixed variable, a green box denotes a changing variable. In both modes the phase, φ, is kept constant by adjusting f_0 via Δf. (a) In constant drive mode V_{drive} is fixed, and any decay to A_{e} is recorded. (b) In constant amplitude mode a second PI controller is used on A_{e}, and V_{drive} is varied to maintain constant amplitude. (c) Schematic of the displacement current created in the sample due to an oscillating tip close to the sample. (c) has been reproduced from Hasan *et al.*[67].

signal, shown in blue and red in Fig. 3.1[§]. The voltage signal from the probe (called 'qPlus' in the controller software) is fed into a lock-in amplifier which disentanlges the signal into the AC electric amplitude of oscillation A_e and the phase difference, φ between V_{drive} and A_e.

During operation, the probe is driven at the resonant frequency of the probe, f_0. To determine f_0 of the probe, the frequency of V_{drive} is swept with the probe far from the sample so that there are no tip-sample forces (known as free space) and A_e and φ are recorded. A typical frequency sweep is shown in Fig. 3.2. f_0 is then recorded, and is used as reference throughout the measurement.

When the probe is close enough to a sample it will detect both conservative and non-conservative forces. Conservative forces will cause the resonant frequency of the probe to decrease and non-conservative (or dissipative) force will cause the amplitude of the probe to decrease. In frequency-modulated AFM (FM-AFM) a phase locked loop (PLL) will shift the frequency of oscillation to match the lowered resonant frequency by keeping the phase constant at the set point $\varphi = \varphi_0$ (See Sect. 3.1.1 for more detail). This shift in resonant frequency is recorded as Δf.

The decaying amplitude can be handled in one of two ways: constant drive or constant amplitude mode. In constant drive mode (Fig. 3.2 (a)) any change in A_e is simply recorded (V_{drive} is also recorded, but is constant). In constant amplitude mode,

[§]The contacts on the tuning fork are also shown in Fig. 3.3, and are labelled 'AFM' and 'GND'

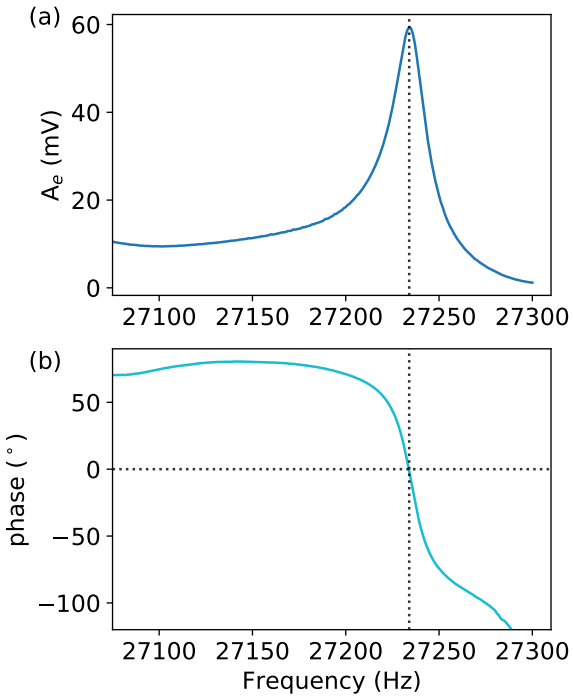

Figure 3.2: A typical frequency sweep used to determine the resonant frequency of the tip with the resulting (a) measured electronic amplitude, A_e, in mV and (b) phase in degrees. At resonance the phase between the V_drive and A_e is 0°, $\varphi_0 = 0°$

shown in Fig. 3.2 (b), there is a second feedback loop on A_e to keep it at the set point, which will increase V_{drive} to do so. In this case, V_{drive} is proportional to the losses in the system. Both A_e and V_{drive} are recorded, but A_e is constant while V_{drive} varies.

We can apply a bias between the tip and sample, V_b, as shown schematically in Fig. 3.1 (c). In our system the bias is applied to the sample and the tip itself is grounded. This ground can be different from the 'GND' electrode on the tuning fork, but are both connected to the chamber ground at the moment. V_b allows us to vary the electrostatic forces between the tip and sample (for more information see Sect. 3.6.1). Fig. 3.1 (c) also shows the induced charge due to proximity of the tip to the sample sample and the applied bias. Because the tip is oscillating, the charge moves within some region under the tip, creating a displacement current, I_d. It is this displacement current, along with the resistance of the system and sample, R_J, that leads to Joule dissipation, which we detect through an increase in V_{drive}. We use the increase in V_{drive} to calculate the damping, Γ, between the tip and sample.

As a final measurement channel we can measure the tunneling current between the tip and sample. For all measurements here, the probe was too far from the sample to detect a tunneling current. However, the total current measured by the tip, I_{tip}, is sensitive to more than the tunneling current; by oscillating the tip we induce a current within the tip, I_{osc}, even in free space[68]. We use the fact that larger V_{drive} results in larger peak-to-peak I_{tip} to determine the calibration factor, κ_1, between V_{drive} and

the mechanical oscillation amplitude of the tip, A_{osc}, in Sect. 3.4.1.

variable	description
V_{drive}	AC voltage applied to the scan tube piezo to oscillate the probe, $\sim$ 20-50 mV.
f_0	Resonant frequency of the qPlus probe.
Q	Quality factor of the probe resonance. Our probes $Q \sim 1000$ at room temperature.
k	Spring constant of the tuning fork. $k = 1800$ N/m for our tuning forks.
Δf	Frequency shift from resonance. One of our measurement channels.
φ	Measured phase between V_{drive} and A_{e}.
φ_0	Phase set point within PLL during operation. At resonance $\varphi_0 = 0°$.
PLL	Phase Locked Loop. A feedback control for oscillatory systems. See Sect. 3.1.1
A_{e}	Electronic oscillation amplitude of the qPlus probe, typically $\sim$ 50-150 mV. Held at a set point $\sim 50 - 150$ mV.
A_{osc}	Mechanical oscillation amplitude of the qPlus probe, here we use 0.5 nm by setting A_{e} inside the PLL.
κ	Calibration factor between A_{e} and A_{osc}. See Sect. 3.4.1
κ_1	Calibration factor between V_{drive} and A_{osc}.
ネ, ("ne")	Frequency-dependent calibration factor to account for off-resonance features within A_{e}. See Sect. 3.3.1.
V_b	Applied bias to the sample. The tip is grounded in our system.
V_{CPD}	Contact Potential Difference voltage, equal to the work function difference between the tip and sample. See Sect. 3.6.2
Φ	Work function of a material, defined as the energy required to remove an electron from the surface.
r_{tip}	Radius of the tip.
I_d	Displacement current, created by moving charges in the sample in the vicinity of the tip.
R_J	The Joule resistance measured by the tip, the sum of sample resistance and system resistance.
Γ	Damping coefficient of the losses between the tip and sample. See Sect. 3.6.3
Γ_J	The Joule damping between the tip and sample. See Sect. 3.6.3
I_{tip}	Current measured by the STM tip.
I_{noise}	Background noise of the STM current line. Typically $\sim$10 pA peak-to-peak in AFM mode.
I_{osc}	Induced current within the tip, caused by the act of oscillating the tip in free space.

Table 3.1: Table of variables used to describe nc-AFM operation and data collection.

3.1.1 Phase locked loop (PLL)

A phase locked loop (PLL) is a feedback control system where the phase output signal is related to phase of the input signal. A PLL is standard for FM-AFM where the probe is driven at its resonant frequency and the system uses the measured oscillation frequency to adjust z position to keep Δf at the set point. The PLL makes use of the *instantaneous* frequency which is defined as the time derivative of the phase. The PLL compares the phase of the drive and detected signals, and keeps them fixed with respect to each other by varying the drive frequency. In this way it keeps the drive and amplitude frequency the same, and measures the frequency shift from its resonant frequency, Δf, required to do so. Tuning the PLL feedback is important because if the PLL feedback is too slow it limits the height feedback speed and reduces the scanning speed.

For completeness, we briefly describe amplitude-modulated AFM (AM-AFM). In AM-AFM there is no PLL to keep the frequency of V_{drive} and A_{e} locked. Instead, the probe is driven at a constant frequency, slightly above f_0 and both the frequency and amplitude are allowed to vary as the probe interacts with the sample. This mode uses the decrease in A_{e} for the z height feedback. This feedback method is more straightforward and is used more often in tapping or contact mode when the topography of the sample is the main measurement of interest. In contrast, extracting the dissipation from this type of measurement is much more difficult since the frequency and

amplitude information are convolved.

3.2 Fabricating qPlus probes for nc-AFM

In nc-AFM the probe measures the force between the tip and samples. It is worth making and testing multiple tips to ensure the probe has a Q-factor of at least 1000 at room temperature. Additionally, it is good practice to perform test measurements with a sample that is well understood such as gold or HOPG to calibrate the work function of the tip and the internal damping.

An AFM probe consists of a macor base (the base can be any material, however the best material will be electrically insulating but thermally conductive), two leaf springs to hold the base in the head securely, and a thin but long macor post upon which a tuning fork is mounted. A side view of the full probe in shown in Fig. 3.3 (a) and (b). In a qPlus configuration one prong of the tuning fork is glued to the macor post (Fig. 3.3 (c)) in the middle of the base and the other prong is allowed to oscillate freely. Fig. 3.3 (e) shows a thin Pt-Ir wire is then attached to the free prong and is either cut or etched to produce the tip of the AFM probe.

Fig. 3.3 (d) shows the electrical connections on the probe which are connected to the head when the probe is loaded: the STM signal line, the AFM signal line, and the AFM reference line, which is connected to ground. The AFM reference ground is the same ground as the chamber, but can be a different ground if the chamber ground is

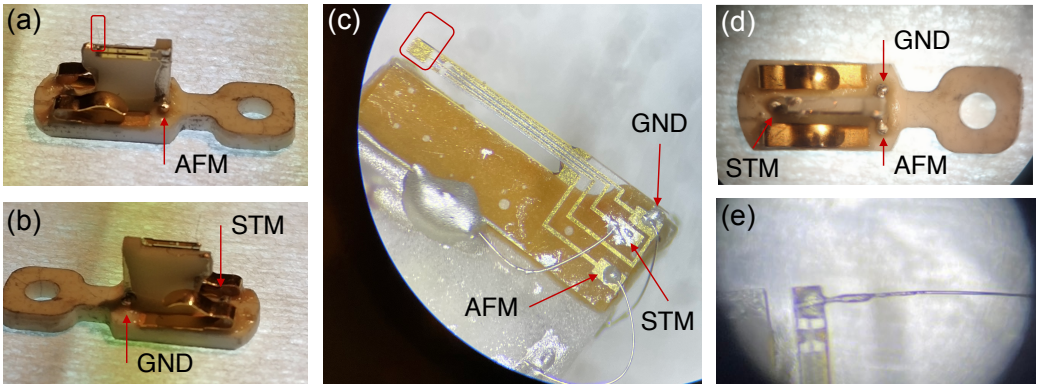

Figure 3.3: A qPlus probe compatible with the RHK head (See Sect. 3.3). (a) A 'front' view of the full probe, with the macor post in the middle. The tip is inside the red rectangle. The AFM signal connection is indicated. (b) A 'back' view of the pull probe. The ground connection (reference for the AFM signal) and STM connection are indicated. The tuning fork shown in (a) and (b) are quartz tuning forks, adapted for nc-AFM. (c) An S1.0 qPlus tuning fork probe from *Nanosurf* attached to the macor post with non-conducting epoxy. The qPlus-specific tuning fork shown in (c) has the signal lines and contact pads deposited directly onto the quartz. Here, we've wire bonded connections to the tuning fork pads, then used conducting epoxy to secure the connection to the macor and subsequently the connections at the base of the probe (indicated in panels (a), (b), and (d)). The GND connection goes to the other side of the macor post, in order to stay separate from the AFM signal line. (d) Top view of the probe, with all signal line connections indicated. (e) A tip attached to the end of the prong with conducting epoxy.

too noisy. At this time, changing this ground would required some re-wiring inside the head.

3.3 Our system: the 'RHK'

We use a commercially purchased system from *RHK Technology*, a company that has developed, designed, and manufactured advanced UHV SPM instruments since 1981. Specifically, we use the *PanScan Freedom model*, which boasts 9 K temperatures using a closed He cycle[†]. Here we refer to the *PanScan Freedom* as simply 'RHK' since that is the name the system has adopted within the lab. Base operating pressure of the chamber is typically better than 7 $\times 10^{-10}$ Torr which is classified as ultrahigh vacuum (UHV) and is used to keep the surface free of contaminants.

By using a closed He cycle, there is no need for cryogens, thus reducing operating costs, and increasing up time on the system. Instead, the system uses ultrapure He gas (99.999%). The gas is fed into a compressor which reduces the temperature of the gas. This compressed gas is then pumped to an expander that extends down a cavity on the top of the system, ending very close the the head where the probe and sample are loaded. This cavity is not under vacuum, in fact it is slightly over pressurized with more UHP He gas to a pressure of +0.5 psi. The expander allows the gas to expand, but to do so requires heat, thus removing heat from the head of the system and cooling it. The compressor and expander make up the cryo-cooling system,

[†] https://www.rhk-tech.com/products/panscan-freedom/

and was purchased from ARS along with the purchase of the RHK. In addition to the cryo-cooler there is a *Lakeshore* heater between the cold finger of the cryo-cooler and the head. This heater can be turned on to counter-act the cooling provided by the cryo-cooler, resulting in a range of possible measurement temperatures from 9 K (minimum temperature with the cryo-cooler on) to 400 K (maximum temperature with the heater on). We use this capability to measure on VO_2 above, below, and during its IMT; from 220 K to 315 K.

We do note that the expander portion of the cryo-cooler introduces 2.4 Hz noise into the system that needs to be either isolated or damped out. First, the expander's support system reduces the amount of weight put on the RHK. Due to space constraints the support frame is one-sided, with the expander overhanging from the side of an upright structure. If possible, a more symmetric design, with two upright support structures on either side of the expander, could support the expander's weight better long-term and reduce the amount of noise introduced to the system. The second aspect of isolation are a set of springs that hold the head. The head can be clamped within the chamber to load and unload tips and samples, but can be suspended on these springs during measurement. These are two important aspects to reducing all sources of noise, specifically the 2.4 Hz noise, detected by the probe during measurements.

The RHK is also designed for interchangeable probes within the head making it easy to switch between an STM and an AFM probe. This design also makes it sim-

ple to switch between different probes of the same type, which was useful for making and testing multiple probes at once then choosing the best one for measurements. For the purposes of this research we focus on using nc-AFM, and thus will focus on that aspect of the system. The ability to quickly change probes is useful, however it introduces the possibility of a probe not being held well mechanically. This can result in different resonance curves by simply unloading and re-loading the same tip.

3.3.1 Determining the usable frequency range

We suspect our system has some non-homogenous driving effects as a function of frequency. This would mean that at some frequencies it is easier or harder to drive the tip, even off resonance, meaning an increase or decrease in the the drive voltage may simply correspond to a particular frequency mode of the system, and not a true difference in tip-sample dissipation.

This frequency-dependent, apparent damping has been characterized for silicon cantilevers by Labuda *et al.*[69]. They propose a unitless, frequency-dependent calibration factor ネ, "ne", to correct for non-linearities when driving the probe, and outline the steps within their report. We have attempted to calculate this calibration factor for our qPlus sensors, but could not detect a good resonance by electrically exciting the probe using the bias voltage. The difficulty of electrically driving a qPlus probe has be documented by at least one previous study[70]. Lee *et al.* model the qPlus as a an equivalent circuit with an inductor (L), resistor (R), and capacitor (C) all in parallel

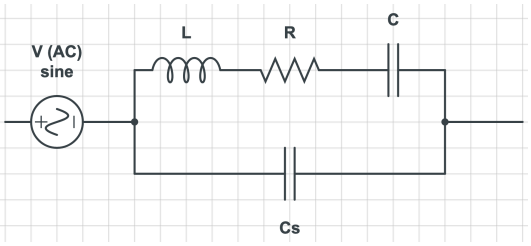

Figure 3.4: The equivalent circuit model for quartz resonators, such as a qPlus probe, adapted from Lee *et al.*[70]. L, R, and C represent the vibrational motion of the probe, and C_s represents a stray capacitance.

with another capacitor (C_s), shown in Fig. 3.4. From this, they derive the electrical signal of the oscillation amplitude as a function of frequency ($\omega = 2\pi f$) to be

$$A_e(\omega) = \frac{A_0 \omega}{Q\omega_0} \sqrt{\frac{1 + 2C_0(1 - \frac{\omega^2}{\omega_0^2}) + C_0^2(1 - \frac{\omega^2}{\omega_0^2})^2 + C_0^2(\frac{\omega}{\omega_0 Q})^2}{(1 - \frac{\omega^2}{\omega_0^2})^2 + (\frac{\omega}{\omega_0 Q})^2}} \tag{3.1}$$

where A_0 is maximum of the resonance, Q is the Q factor, $C_0 = C_s/C$, and $\omega_0 = 1/\sqrt{LC} = 2\pi f_0$ and is equal to the resonant frequency[70]. We fit our resonance curves to this model to determine frequencies that deviate from this well-behaved resonance.

We normalize the amplitude of the frequency sweep so that A_0 is 1, then use Q, f_0 and C_0 as fit parameters. Fig. 3.5 shows a frequency sweep and fit to Eq. 3.1. The fitting produces Q and f_0 values that are within error of those determined by the R9 software during measurement. We then compare the fit and the amplitude data and select cutoff frequencies where the data deviates from the fit. In Fig. 3.5 we show one such data sweep with fit to Eq. 3.1, and denote the cut off frequencies above and below the resonance with dotted black lines. Inside the dotted black lines is the range of

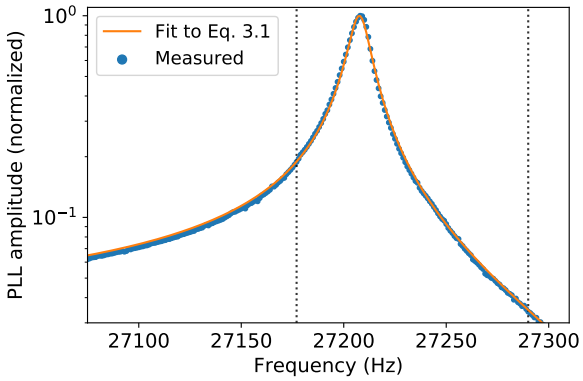

Figure 3.5: A representative frequency sweep used to determine the range of good frequencies for this probe. The data is fit to Eq. 3.1. We then set a cut off frequency where tails of the resonance deviates from the fit by 5% of the value, discarding the data below (above) that cut off below (above) resonance. The region inside the dotted black lines are the frequencies used throughout this work for this temperature.

frequencies that adequately follow the model, and thus have little to no influence from the drive-factor of our system ネ (f). We determine the cut-off frequencies for each temperature, since ネ (f) may also be temperature dependent.

3.4 Approach and calibration

After loading a probe and sample into the head of the RHK, next step is to approach the sample the tip. Initially this is done by eye with the coarse walker and a magnifying video feed. However, once the tip and probe are a few less than mm apart (estimated by eye) the final, 'fine' approach is completed by the software using the z feedback. The z feedback uses a PI-loop on the measured current in STM mode, and on the measured Δf in nc-AFM mode.

Approaching using AFM can be unreliable because the approach relies on the z feedback, which for AFM relies on good PLL feedback settings, and the Δf and phase of the probe. Both the central frequency (f_0) and phase can drift due to slight temperature differences. For example, if the probe is loaded from room temperature but the head and sample are at a different temperature, there is a thermal gradient between tip and sample which can affect the resonant frequency of the probe. Also, as described in Sect. 3.3, coarse approach steps can shift the probe in its holder slightly, but enough to alter the resonant frequency. If possible (i.e. if a tunneling current can be achieved), it is recommended to approach in STM mode, then switch to AFM mode once the probe is within the fine z movement of the scan tube.

When approaching in AFM (coarse or fine), bias sweeps are useful for determining the probe is within range of electrostatic forces between the tip and sample. Electrostatic force are long range (up to $\sim$ μm) and present as a parabolic dependence in both the frequency shift (inverted) or the drive voltage (up-right)[‡]. If the frequency-bias or damping-bias curves are flat this indicates no, or very little, electrostatic forces, implying the probe is far from the sample. Once the bias-sweeps show parabolic behavior this indicates the probe is within $\sim$ 100s nm of the surface, depending on the sample-dependent strength of the electrostatic forces.

Once the sample is in range of the piezo scan tube, tune the PLL at the resonant

[‡]For more details on the electrostatic forces and CPD see Sect. 3.6.2

frequency[§], and calibrate the amplitude (See Sect. 3.4.1).

The final, and most useful sweep to determine tip-sample separation is the distance sweep. While bias sweeps are useful for determining when the probe is within 100s nm of the sample, the distance sweep is the only way to determine the tip-sample separation on the nm scale. Since nc-AFM measures forces between the tip and sample, we expect the force-distance curve similar to the Lennard Jones potential[††]: a strong repulsive force at the closest z, followed by a dip at some slightly further z separation, as shown in Fig. 3.6. However, nc-AFM measures the tip-sample forces via Δf in the resonant frequency, which is proportional to the derivative of the force with respect to z. The actual measured Δf is shown overlayed on Fig. 3.6, with a similar behavior: a steep repulsive regime at the closest z values (corresponding to a positive frequency shift), and a minimum ~ 3 nm (corresponding to the attractive regime).

3.4.1 Tip amplitude calibration

Within the RHK software, R9, the signal for the probe oscillation is called the 'PLL amplitude' and is measured in V. We need to perform an amplitude calibration to convert a voltage reading (typically 10s mV) to a physical amplitude (typically 100s pm). We follow the calibration outlined by Dagdeviren *et al.*[68]. The method equates the mechanical dissipation in free space (i.e. while not interacting with the sample)

[§]RHK provides a detailed tutorial here https://www.rhk-tech.com/support/tutorials/

[††]See Sect. 3.6.1 for a full description of tip-sample forces

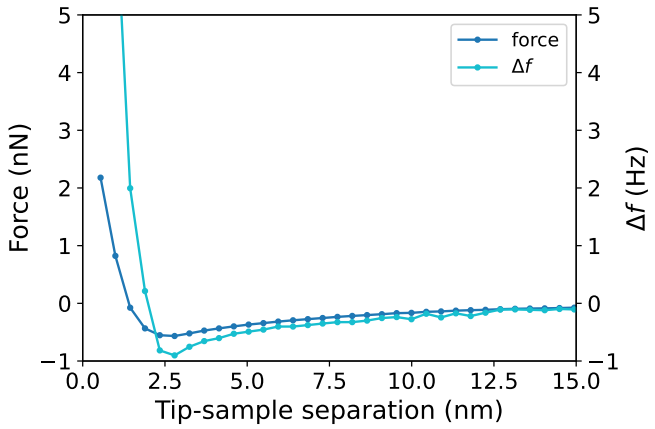

Figure 3.6: Representative force-distance sweep showing the repulsive regime ($z < \sim$2 nm) and attractive regime ($z > \sim$2 nm). The force is calculated from the corresponding measured Δf-distance curve using Eq. 3.16 in Sect. 3.6.1.

with the power supplied per cycle:

$$E_{\text{diss, mechanical}} = P_{\text{supplied}}/f_0 \tag{3.2}$$

$$\frac{2\pi}{Q} \times \frac{1}{2} k A_{\text{osc}}^2 = \frac{1}{2f_0} V_{\text{drive}} I_{\text{osc}} \cos\varphi \tag{3.3}$$

where Q is the Q-factor of the resonance, k and f_0 are the spring constant and central frequency of the probe respectively, V_{drive} is the drive bias applied to the piezo, and I_{osc} is the induced current due to the mechanical oscillation (See Fig.3.1 for reference).

We rearrange for A_{osc}, using the fact that at resonance the phase between the drive

and measured probe is 0, so $\cos\varphi_0 = 1$.

$$A_{\text{osc}} = \sqrt{\frac{V_{\text{drive}} I_{\text{osc}} Q}{2\pi f_0 k}} \tag{3.4}$$

Since $I_{\text{osc}} \propto V_{\text{drive}}$, then $A_{\text{osc}} \propto \kappa_1 V_{\text{drive}}$, where κ_1 is the calibration factor between the piezo drive (in mV) and mechanical oscillation amplitude (in nm). One could calibrate the amplitude to the drive, but it may be more useful to calibrate the measured electrical amplitude signal, A_{e} (in mV), to A_{osc}. To do so, we recognize that A_{e} is related to V_{drive} by a linear signal-to-drive gain value. As such, we arrive at

$$A_{\text{osc}} \propto \kappa A_{\text{e}}, \tag{3.5}$$

where κ is the calibration factor between electrical amplitude signal in mV and mechanical oscillation amplitude in nm[68].

Using Eq. 3.4, calculate A_{osc} using probe parameters Q, k, and f_0 measured through a frequency sweep at each V_{drive}. However, when determining current induced by tip oscillation, we note that the current measured with the oscilloscope will include both the background noise of the system and the induced current due to the tip oscillating,

$$I_{\text{tip}} = I_{\text{noise}} + I_{\text{osc}} \tag{3.6}$$

To extract I_{osc} from I_{tip} we perform frequency sweeps at a minimum of four V_{drive} val-

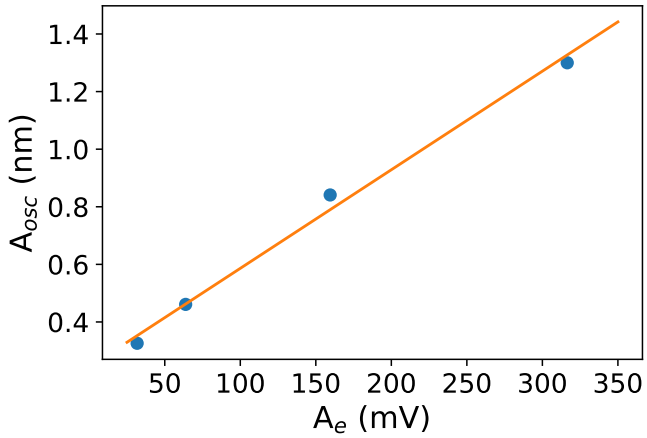

Figure 3.7: A representative tip amplitude calibration. A_e values were read at set V_drive values, and A_osc values were calculated using I_tip in Eq. 3.4. The slope is 0.0034232 nm/mV and is the calibration between measured electrical amplitude in mV to mechanical oscillation amplitude in nm for this probe, at this temperature.

ues, and use I_tip as the peak-to-peak value of the oscilloscope, calculating a not-quite-correct A_osc. We then fit the slope of the A_osc vs A_e plot to determine κ in Eq. 3.5, in units of nm/mV.

3.5 Data collection: z-V_b maps

At each temperature we first found the surface using STM mode then switched to constant amplitude nc-AFM mode and calibrated the tip (See Sect. 3.4.1). Once the PLL was tuned, we found the surface using nc-AFM at $V_b = 1.5$ V and a set point of around -1.5 Hz. We then performed a distance sweep to determine the position of the tip relative to the sample. Once the characteristic inflection was found (as shown in Fig. 3.6) we could safely assume we were within 5 nm of the surface of the sample.

We saved a distance sweep with the inflection upwards and as much of the flat Δf as possible for drift correction (See Sect. 4.1).

After taking at least one good distance sweep, we ran a custom-made routine named "V-z Spectroscopy" that moved the tip back 20 nm, then would iteratively perform a bias sweep from +10 V to - 10 V and back to +10 V before stepping towards the sample by 0.2 nm and repeating. The system would repeat this process until stopped, either manually or by the 'Lock Guard' within the PLL*. This would occur when the PLL could no longer feedback; typically when the probe was too close to the sample such that the repulsive forces push the frequency too far from the resonant frequency. For 290 K, 300 K and 315 K a step sized of 0.5 nm was used. At 300 K the initial step back was 30 nm. This procedure resulted in anywhere between 30 and 100 bias sweeps, depending on the step sizes used. Any discrepancy between the programmed number of sweeps to reach the surface and the required number of sweeps could be due to piezo drift or high electrostatic forces. We consider piezo drift in Sect. 4.1 and find plays a small role in our measurements. More likely, the high electrostatic forces achieved during a bias sweep disrupt the PLL's ability to feedback at 10 V, compared to the 1.5 V used to find the surface. Each bias sweep included a forward and backwards sweep, taking 20 s, with a full map taking approximately 30 minutes, up to an hour. Within a full measurement the thermocouple reading nearest the sample would

*The Lock Guard fully retracted the piezo if the PLL could not be locked into stable feedback.

drift by no more 0.4 K, but was typically closer to 0.2 K.

This entire procedure would be repeated at different probe oscillations amplitudes (0.25 nm, 0.5 nm, and 1 nm), sample bias ramp rates (1 V/s, 5 V/s, 10 V/s, 20 V/s), and locations ($\sim$ 500+ nm away) on the sample before retracting the tip via the scan tube, and allowing the sample to heat and stabilize once again.

3.6 Theoretical dependencies of the measured data

Here we consider the general behavior of the two measurement channels we have access to: Δf and V_{drive}. We recall that the system also records the phase, oscillation amplitude voltage, and current at each data point. The PLL is holding the phase constant, and so should measure φ_0. Any large deviations from φ_0 can be used to quantify the error on the measurement. We do not record any large deviations from φ_0 within any of our data sets. Similarly, in constant amplitude operation, the oscillation amplitude is being held constant at the set point through the PLL, which is also what we observe in the data. The current signal can be used to detect tunneling current; for all measurements here we detect 0 pA of current, within the baseline peak-to-peak noise of the system of 5 pA.

3.6.1 Forces between the tip and sample

The tip detects three dominating forces acting between the tip and sample: the close range repulsive force, the mid- to long-range attractive van der Waals (vdW) forces, and long-range attractive electrostatic forces. Each of these forces have different z and V_b dependencies, allowing us to isolate the electrostatic forces by looking at bias curves.

We base the repulsive force off of the well known phenomenological Lennard-Jones model, which consists of a repulsive term proportional to z^{-12} and an attractive term proportional to z^{-6}. In this model the attractive term is derived from the vdW forces between two particles, and the repulsive term is simply the square of that for computational purposes. In reality, our system consists of a tip and a sample which will have a different vdW attractive dependence. Specifically, we assume the tip is a sphere with a conical base and, following the work by Kuhn and Rahe[71] for the functional form, we determine vdW force to be

$$F_{\mathrm{vdW}}(z) = -\frac{H}{6}\left(\frac{r_{\mathrm{tip}}}{z^2} + \frac{r_{\mathrm{tip}}(1-\sin\theta)}{z[z + r_{\mathrm{tip}}(1-\sin\theta)]} + \frac{\tan^2\theta}{z + r_{\mathrm{tip}}(1-\sin\theta)}\right), \tag{3.7}$$

where H is Hamaker's constant; defined specifically for vdW forces between two materials, r_{tip} is the radius of the tip, and θ is the conical half-angle of the tip, defined relative to the z direction.

Hamaker's constant, H_{132}, is defined for two materials (subscripts 1 and 2) interacting in a third material (subscript 3). For our experiment we know the tip is Pt, the sample is VO_2 and they are interacting in vacuum. Hamaker's constant also has the property that

$$H_{1V2} = \sqrt{H_{1V1}}\sqrt{H_{2V2}} \tag{3.8}$$

where the subscript $_V$ symbolizes vacuum.

The tip material, Pt, is a well known metal and thus we can look up $H_{Pt-V-Pt}$ in a table: 4.55 $\times 10^{-19}$ J[72]. VO_2 on the other hand is less comprehensively studied. However, TiO_2 is similar to VO_2 in many ways and does have some tabulated values. One paper reports $H_{TiO_2-V-TiO_2} = 18.1 \times 10^{-20}$ J[73]. A second paper lists the vacuum self-Hamaker's constant for many ceramics and they all tend to fall in the range 10-20 $\times 10^{-20}$ J[74]. The TiO_2 measurement included in this table is 15.3 $\times 10^{-20}$ J. Although we do not have an exact measurement of $H_{VO_2-V-VO_2}$, given that ceramics tend to fall in this narrow range, we use $H_{VO_2-V-VO_2} = 18 \times 10^{-20}$ J. Then using Eq. 3.8 we calculate Hamaker's constant for our set-up to be about 0.3 aJ.

We chose a repulsive force of the form

$$F_{\text{repulsive}}(z) = C_{\text{repulsive}} \exp(-z/\tau_{\text{repulsive}}), \tag{3.9}$$

where $C_{\text{repulsive}}$ is the strength of the repulsive force and $\tau_{\text{repulsive}}$ is the length scale

of the repulsive force[75]. In the canonical Lennard-Jones model the repulsive force is completely phenomenological and so instead, we chose an exponential decay model that allows us to tune both the strength and the length scale separately.

Finally, for electrostatic forces, we model the tip-sample junction as a capacitor that varies with the tip-sample separation and oscillation of the tip. The electric potential energy stored in a capacitor is $U = \frac{1}{2}C(V_b - V_{\text{CPD}})^2$, and $F = -\partial U/\partial z$, giving an expression for the electrostatic force

$$F_{\text{el}}(V_b, z) = -\frac{1}{2}\frac{\partial C(z)}{\partial z}(V_b - V_{\text{CPD}})^2 \tag{3.10}$$

where we shifted the applied bias V_b, by the contact potential difference (CPD) V_{CPD} of the materials. The CPD corresponds to the minimum electrostatic forces between the tip and sample and is equal to the difference in the work functions between the materials. We explain the origin of CPD further in Sect. 3.6.2.

Putting the repulsive (Eq. 3.9), vdW (Eq. 3.7), and electrostatic forces (Eq. 3.10) together, we write the full force between the tip and sample

$$\begin{aligned} F(V_b, z) = {} & C_{\text{repulsive}} \exp(-z/\tau_{\text{repulsive}}) \\ & - \frac{H}{6}\left(\frac{r_{\text{tip}}}{z^2} + \frac{r_{\text{tip}}(1-\sin\theta)}{z[z + r_{\text{tip}}(1-\sin\theta)]} + \frac{\tan^2\theta}{z + r_{\text{tip}}(1-\sin\theta)}\right) \\ & - \frac{1}{2}\frac{\partial C(z)}{\partial z}(V_b - V_{\text{CPD}})^2 \end{aligned} \tag{3.11}$$

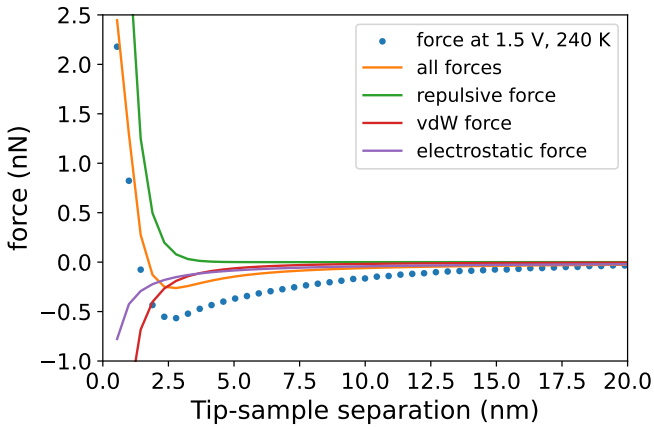

Figure 3.8: Representative force-distance sweep showing the total force (Eq. 3.11) and each individual force: repulsive (Eq. 3.9), vdW (Eq. 3.7), and electrostatic (Eq. 3.10). The sum of the forces (orange) doesn't exactly match the measured data (blue points) due to the difficulty of accurately modeling the z dependence of the electrostatic forces.

We show the total forces detected by the tip and the individual components based on this equation in Fig. 3.8.

The tip-sample forces will shift the resonant frequency, which is one of the raw data channels we measure. For small oscillation amplitude ($A_{\text{osc}} << z$) the frequency shift is related to derivative of the force[76]

$$\Delta f(V_b, z) = -\frac{f_0}{2k}\frac{\partial F(V_b, z)}{\partial z}. \tag{3.12}$$

This can also be seen in the Sader-Jarvis formula, Eq. 3.16 which we discuss in Sect. 3.6.1.

We write an expression for the bias-dependence of the frequency shift due to elec-

trostatic forces in terms of the tip-sample separation z and applied bias, V_b,

$$\Delta f_{\mathrm{el}}(V_b, z) = \frac{f_0}{4k}\frac{\partial^2 C(z)}{\partial z^2}(V_b - V_{\mathrm{CPD}})^2, \tag{3.13}$$

namely, we expect an inverted parabola, centered at the CPD voltage.

This derivation is very general up to this point, so let us specify the tip geometry and calculate the resulting capacitance. The typical approach is to model the tip as a sphere and the film as a plane[77,78], with the resulting

$$\partial C(z)/\partial z = -2\pi\epsilon_0 r_{\mathrm{tip}}/z. \tag{3.14}$$

Thus, we can model the measured frequency shift due to electrostatic forces as

$$\Delta f_{\mathrm{el}}(V_b, z) = -\frac{\pi\epsilon_0 r_{\mathrm{tip}} f_0}{2k}\frac{(V_b - V_{\mathrm{CPD}})^2}{z^2}. \tag{3.15}$$

Based on Eq. 3.15 we expect an inverted parabola in the Δf-bias curves. From this fitting we extract two important film-dependent quantities: the tip-sample capacitance and the CPD voltage.

Calculating the force from measured data: Δf

To calculate the force from the measured frequency shift we use the Sader-Jarvis formula[79], which has the form

$$F(z) = \frac{2k}{f_0}\left[\int_z^\infty \Delta f(\zeta)d\zeta + \frac{A_{\text{osc}}^{1/2}}{8\sqrt{\pi}}\int_z^\infty \frac{\Delta f(\zeta)}{\sqrt{(\zeta - z)}}d\zeta - \frac{A_{\text{osc}}^{3/2}}{\sqrt{2}}\int_z^\infty \frac{1}{\sqrt{(\zeta - z)}}\left(\frac{d\Delta f(\zeta)}{d\zeta}\right)d\zeta\right], \tag{3.16}$$

where A_{osc} is the tip amplitude and ζ is the integration variable over tip-sample separations at fixed V_b. This formula is the most accurate calculation of the force. However, it may be useful to simplify the formula; namely a small amplitude and large amplitude approximation (as seen in Eq. 3.12). The small amplitude approximation uses only the first term ($\sim \Delta f/f_0$), while the large amplitude approximation uses only the last term ($\sim A_{\text{osc}}^{3/2}$).

3.6.2 Contact potential difference (CPD)

The contact potential difference (CPD) is the bias value of the minimum of the Δf-bias parabola, and corresponds to the minimum electrostatic force. Each material has a work function (Φ), defined as the energy required to remove electrons from the surface (Fig. 3.9 panel (i)). Here, the tip and sample are connected via the bias line in the AFM. The tip and sample are therefore in thermodynamic equilibrium and their Fermi levels will align (Fig. 3.9 panel (ii)).

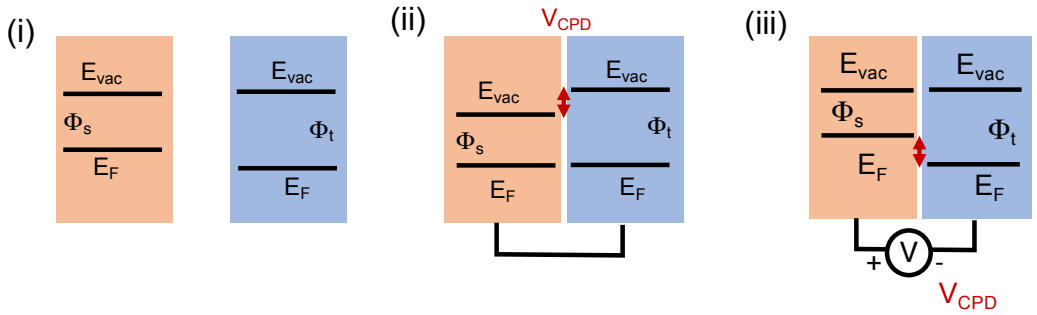

Figure 3.9: Schematic of the origin of the contact potential difference (CPD). Panel (i) two non-interacting materials each have a work function Φ defined as the energy required to remove one electron from the surface to the vacuum. (ii) When the materials are brought to thermodynamic equilibrium charges re-organize so that the Fermi energies are equal. This causes an imbalance of charge and a net, macroscopic electrostatic force between the materials. (iii) A voltage opposing the charge imbalance sets the electrostatic forces equal to 0, such that $V_b = -V_{\text{CPD}}$.

This however causes an imbalance of charge and a net electrostatic force with potential equal to $(\Phi_s - \Phi_t)/e$. To eliminate the electrostatic force we apply a sample bias equal to the work function difference, the CPD voltage (Fig. 3.9 panel (iii)). The CPD voltge is equal to

$$V_{\text{CPD}} = (\Phi_{\text{sample}} - \Phi_{\text{tip}})/e. \tag{3.17}$$

Furthermore, if we know the work function of our tip, then the work function of VO_2 is simply a linear shift from the measured CPD value:

$$\Phi_{VO_2} = eV_{\text{CPD}} + \Phi_{\text{tip}} \tag{3.18}$$

3.6.3 Dissipation between the tip and sample

The Joule dissipation (in eV/cycle) is equal to the power dissipated due to the motion of charge within the sample induced by the motion of the tip, which is shown in Fig. 3.1 (c). The average Joule power dissipated per cycle equal to

$$\langle P_J \rangle = \int_0^{1/f} I_d^2 R_J dt, \tag{3.19}$$

where I_d is the displacement current, and R_J is the Joule resistance which is equal to the full resistance of the sample and system[67].

The displacement current is entirely due to the tip-sample capacitance, which can be written as $I_d = \partial C/\partial t\ (V_b - V_{\mathrm{CPD}})$. The power equation becomes

$$\langle P_J \rangle = \int_0^{1/f} \left(\frac{\partial C}{\partial z(t)} \frac{\partial z(t)}{\partial t} \right)^2 (V_b - V_{\mathrm{CPD}})^2 R_J dt. \tag{3.20}$$

We use $z(t) = z + A_{\mathrm{osc}} \cos(2\pi f t)$, $\partial z(t)/\partial t = 2\pi f A_{\mathrm{osc}} \sin(2\pi f t)$, and $\partial C/\partial z(t)$ as defined in equation 3.14. Plugging these in and removing all constants from the integral leaves:

$$\langle P_J \rangle = (4\pi^2 \epsilon_0 r_{\mathrm{tip}} A_{\mathrm{osc}} f)^2 R_J (V_b - V_{\mathrm{CPD}})^2 \int_0^{1/f} \left(\frac{\sin(2\pi f t)}{z + A_{\mathrm{osc}} \cos(2\pi f t)} \right)^2 dt. \tag{3.21}$$

This integral has been solved elsewhere[77], with the following result

$$\langle P_J \rangle = 16\pi^4 \epsilon^2 r_{\text{tip}}^2 f^2 R_J (V_b - V_{\text{CPD}})^2 \frac{f}{A_{\text{osc}}^2} \frac{z\sqrt{z^2 - A_{\text{osc}}^2}}{\sqrt{z^2 - A_{\text{osc}}^2}}. \tag{3.22}$$

From classical mechanics of a damped, driven system, the power dissipated is the $v^2\Gamma$, where v is the velocity of the object and Γ is the damping coefficient. Using the $v = \partial z(t)/\partial t$ for the velocity of the tip, and taking the average over one period, the average power in terms of damping coefficient is:

$$\langle P_J \rangle = 2\pi^2 f^2 A_{\text{osc}}^2 \Gamma. \tag{3.23}$$

Using the small angle approximation where $a << z$, and $\sqrt{1-x} \approx 1 - \frac{x}{2}$ we arrive at

$$\Gamma_J(V_b, z) = 8\pi^2 \epsilon^2 r_{\text{tip}}^2 R_J \frac{(V_b - V_{\text{CPD}})^2}{z^2}. \tag{3.24}$$

Based on Eq. 3.24 we expect an upward parabola in the damping-bias curves, with the opening proportional to the sample resistance.

Calculating the damping coefficient from measured data: drive voltage

To calculate the damping coefficient, Γ, from constant amplitude FM-AFM data we use

$$\Gamma(V_b, z) = \Gamma_0 \left(\frac{V_{\text{drive}}(V_b, z)}{V_{\text{drive}}(z \to \infty)} - \frac{\Delta f}{f_0} \right) \tag{3.25}$$

$$\Gamma_0 = \frac{k}{f_0 Q} \approx \frac{1800 \text{ N/m}}{27 \text{ kHz} \times 1000} \approx 7 \times 10^{-5} \text{ kg/s} \tag{3.26}$$

where Γ_0 is the internal damping of the tip and is related to the power required to maintain the tip oscillation in the absence of any tip-sample interactions[66].

3.6.4 drive-Δf

We notice that Δf and Γ_J have the same z and V_b dependence (Eq. 3.15 and 3.24 respectively).

If we fit both the Δf-bias and Γ-bias data to parabolas of the form $\Delta f(V_b) = -\alpha_{\Delta f}(V_b - V_{\text{CPD}})^2 + \beta_{\Delta f}$ and $\Gamma(V_b) = \alpha_\Gamma(V_b - V_{\text{CPD}})^2 + \beta_\Gamma$, then $\alpha_{\Delta f} = \pi \epsilon r_{\text{tip}} f_0/(2kz^2)$ for each z and $\alpha_\Gamma = 8\pi^2 \epsilon^2 r_{\text{tip}}^2 R_J / z^2$. Then we find that

$$\frac{\alpha_\Gamma}{\alpha_{\Delta f}} = \frac{8\pi^2 \epsilon^2 r_{\text{tip}}^2 R_J / z^2}{\pi \epsilon r_{\text{tip}} f_0/(2kz^2)} = \frac{16 k \pi \epsilon r_{\text{tip}} R_J}{f_0}, \tag{3.27}$$

and

$$R_J = \frac{f_0}{16k\pi\epsilon r_{\text{tip}}} \frac{\alpha_\Gamma}{\alpha_{\Delta f}}, \tag{3.28}$$

where α_Γ and $\alpha_{\Delta f}$ are nominally positive fit values.

Or, similarly, if we substitute $-2k\Delta f/f_0$ (from Eq. 3.15) for $\pi\epsilon_0 r_{\text{tip}}(V_b - V_{\text{CPD}})^2/z^2$ into the expression for Γ (Eq. 3.24) we find that if we plot Γ and Δf, the negative slope of the would be proportional to the resistance,

$$\Gamma_J(V_b, z) = \frac{-16k\pi\epsilon r_{\text{tip}}}{f_0} \; R_J \; \Delta f(V, z) \tag{3.29}$$

Hasan *et al.*[67] performed a similar derivation for large tip amplitude, however here we show the results hold for small amplitudes as well.

Physically, the Joule damping and frequency shift are related because both the Joule dissipation and electrostatic forces are dependent on the displacement current induced in the sample by the motion of the tip (Fig. 3.1 (c)). Mathematically, the induced current comes from the respective dependencies on the capacitance gradient: $\Delta f \sim \partial^2 C/\partial z^2$ and $\Gamma \sim (\partial C/\partial z)^2$, which are generic, and hold in all small amplitude cases. However, the specific z dependence is only the same because we assume $(\partial C/\partial z) \sim 1/z$, which *may not always be the case.*

4

Doping and dissipation measured across the IMT in VO_2

For nc-AFM measurements we grew a two VO_2 samples on TiO_2(001) on the same day using the same growth conditions. We used a V flux of 10^{13} V atoms/(cm^2· s) and an O partial pressure of 2.5 $\times 10^{-6}$ Torr, depositing V for 1 hour, result-

ing in a 10 nm thick film based on our results from Sect. 2.2. The substrate temperature was held at 150°C during growth and was ramped to 300°C for 10 minutes after V deposition, all with same O pressure as V deposition.

The VO_2 sample we study here was grown then transferred entirely *in situ*, never being exposed to air between growth and nc-AFM measurements[‡]. The second sample (Air Sample) was removed from vacuum, and XRD, and transport were performed. These measurements are shown in Fig. 4.1, and confirmed this sample was VO_2 with change in resistance of almost 3 orders of magnitude at 290 K, as expected. Both samples' *ex situ* characterization are discussed in more detail in Appendix A.

For the series of measurements presented in this chapter, we started on a gold sample at 220 K. After confirming the expected behavior of Δf and V_{drive} as a function of z and V_b on the gold, we loaded the VO_2 sample into the microscope. The sample sat at 220 K overnight to thermalize. We then took multiple z-V_b maps at varying oscillation amplitude, V sweep rate, and locations. All maps were self-consistent. We then warmed the system to 240 K, letting it thermally stabilize overnight. We repeated the series of z-V_b map measurements,

[‡]Due to required fixes within the chamber, it was briefly transferred to a glove box (with water oxygen index less than 1 part per million) for no more than two weeks before being re-loaded in the UHV chamber of the RHK, after which the measurements presented in this work were taken. More information is given in Appendix A

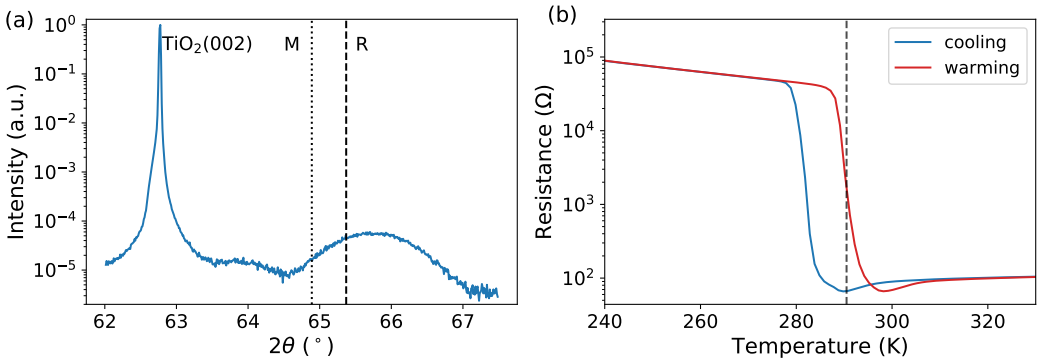

Figure 4.1: Characterization of a copy of the film studied throughout Chapter 4. (a) XRD on the Air Sample, with the peak position for bulk $VO_2(40\bar{2})_M$ ($VO_2(002)_R$) marked with a dotted (dashed) black line and labeled with 'M' ('R'). The peak position of the Air Sample is most consistent with $VO_2(002)_R$. (b) Transport showing a 3 order of magnitude transition centered at 290.5 K (warming), marked with the dashed black line.

again finding consistent results. We continued in this manner at 255 K, 270 K, 290 K and 315 K. After 315 K, we loaded the same Au sample and repeated the series of measurements to once again confirm the expected behavior of a known sample.

After the final 315 K z-V_b map on gold, we loaded VO_2 into the microscope again and turned the heater off but left the cryo-cooler on to perform a temperature sweep. During the temperature sweep we continuously measured bias sweeps from +3V to -2 V, forwards and backwards, adjusting the tip position to keep the max Δf around -10 Hz. After the cooling sweep reached 220 K, the heater was set to high power to sweep the temperature upwards and bias-sweeps we repeated. After this series of measurements the sample was removed from

vacuum and placed in a desiccator.

Three months later, to confirm the 290 K behavior, a second (previously unused) tip and the same VO_2 sample we loaded back into the RHK. We once again started with a known sample, this time HOPG, and confirmed metallic behavior. We then loaded VO_2 into the microscope head and measured the same series of $z - V_B$ maps at 300 K, with both the cryo-cooler and heater off. This measurement was after the sample had been exposed to air, however we do not expect this to affect the measurement[80].

4.1 Δf: DRIFT CORRECTION

There are two drift corrections that we may have to apply to our data, and we use to Δf data to perform these corrections. The first is drift related to the stability of the measured phase, φ, which may be due to thermal drift shifting f_0 or due to electronic drift within the PLL. As a result of the phase drifting, Δf will be above or below 0 Hz far from the sample, at the CPD voltage where the vdW forces should be ~ 0. We can see this by looking at a z slice of Δf (dark blue line in Fig. 4.2). This z slice is taken at V_{CPD} of the z-V_b map. The light blue curve in Fig. 4.2 shows the linearly shifted Δf with z, after correcting for any offset far from the sample where Δf should be 0.

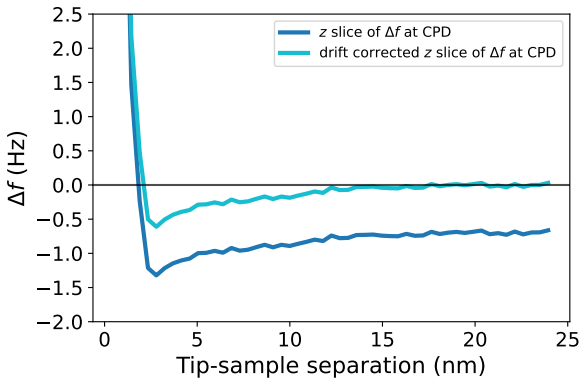

Figure 4.2: In the time between calibrating the probe and starting the z-V_b measurement we find that the phase can drift, causing Δf to shift by a few Hz. We correct for the phase, and subsequent Δf, shift by shifting the whole z-V_b map by a constant such that the z slice at $V_{\text{CPD}} \to 0$. Here, that shift is $\sim$ -1 Hz.

The second potential drift within the measurement is piezo drift due to the z-V_b map taking a finite amount of time. In this case we typically ramp at 1 V/s, meaning each z position takes 20 s, and a full dissipation map takes at minimum 30 minutes. This drift would affect the apparent tip-sample separation, stretching compressing the z axis in the z-V_b map. We can correct for this type of drift by comparing the z-slice of the data at the set bias voltage to the Δf in the pre-map z-sweep. In Fig. 4.3 we show a representative Δf-z measurement taken before the dissipation map in orange, and the corresponding z slice both before (dark blue) and after (light blue) the piezo drift factor. The correction shown here is a factor on the measured z of 0.9, highlighting that the effect of piezo drift on our measured z is typically quite small, and that we are able to

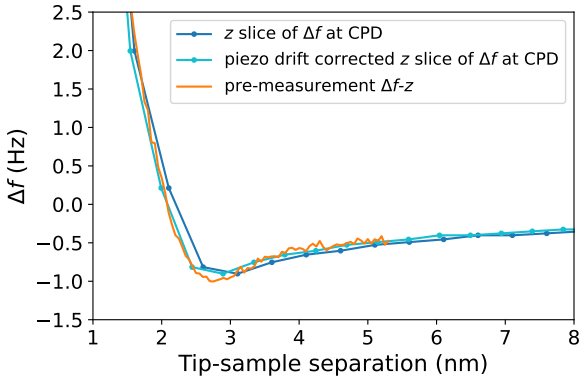

Figure 4.3: We show the Δf-z curve taken before the z-V_b measurement and the corresponding Δf-z slice from the z-V_b map (both at 1.5 V). In this map we estimate piezo drift has shortened the apparent z values by up to 10%, and show the corresponding piezo drift corrected Δf-z slice in light blue. This temperature had the largest piezo drift with a 0.9 correction factor on z, while other temperatures had a factor closer to 1, highlighting the small effect of piezo drift on these measurements.

correct for it.

4.2 Force: sample position, work function, and doping

As outlined in Sect. 3.6.1, we calculate the force between the tip and sample by integrating Δf with respect to z at each applied bias, creating a force map over the same z and V_b range. We then use the force in three ways: first to determine the sample position by fitting, second to determine the work function of the sample, and third to calculate the tip-sample capacitance.

4.2.1 Fit the sample position using force-distance curves

To determine the sample position relative to the tip we fit the force-distance curves at the V_{CPD} to the short-ranged repulsive forces and attractive vdW forces, as in Eq. 3.11 (See Sect. 3.6.1). We use V_{CPD} such that the electrostatic forces are 0. Fitting the repulsive and vdW forces to accurately determine the sample position is necessary to compare quantitative behaviors at similar tip heights between data collected at different temperatures. To determine V_{CPD} we fit the force-bias curves to a parabola of the form defined by Eq. 3.10 and extract V_{CPD} at each z. We see a slight z dependence to the CPD at each temperature, which we discuss in more detail in Sect. 4.2.2. For the purpose of the force-bias fitting we take the average of V_{CPD} for $z > 10$ nm and assume the electrostatic forces are negligible within the observed variation of 0.1 V.

The z data collected is the z position of the probe relative to the piezo scan tube, and therefore must be converted to tip-sample separation. To do so, we fit to Eq. 3.11 where z is replaced with $z - z_s$, where z_s is the relative sample position, such that z is the tip-sample position. Fig. 4.4 shows one such fit where z_s, $C_{\text{repulsive}}$, $\tau_{\text{repulsive}}$, r_{tip}, and θ are fit parameters. We determine the the relative sample position z_s, giving us an accurate tip-sample spacing z. The fitting also allows us to extract the radius of the tip. We fit the tip radius at each tempera-

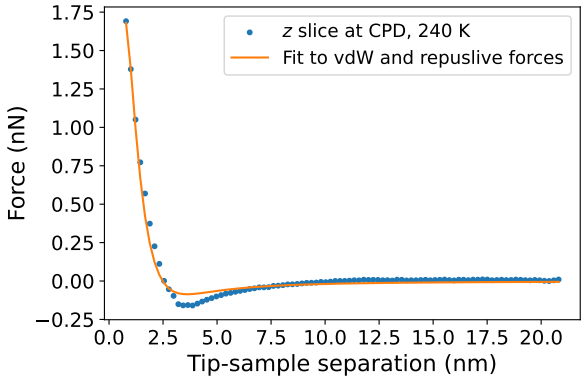

Figure 4.4: Representative force-distance curve with fit to vdW and repulsive forces (Eq. 3.11) at $V_b = V_{\text{CPD}}$ to determine sample position and tip radius. The vdW force used here models the probe as a sphere with conical sides. Our real probe may not be a perfect cone or sphere, leading to an under-estimation of the attractive force around 3 nm. We have considered a sphere and a cone separately, but the model that considered the sphere and cone together best describes the data.

ture, and find the average and standard deviation across all temperatures to be 28 ± 3 nm[†].

In theory we could fit the force-distance curves at arbitrary voltages to determine the electrostatics forces. In practice this is quite difficult since the z dependence of the electrostatic forces depends on the tip-sample geometry via the tip-sample capacitance. In practice it is much easier to determine the tip-sample capacitance (and subsequent magnitude of the electrostatic force) by fitting the force-bias curves, which we discuss in Sect. 4.2.3.

[†]At 300 K we estimate r_{tip} to be half that of the other temperatures. This data set was measured with a different tip, and so is not unreasonable.

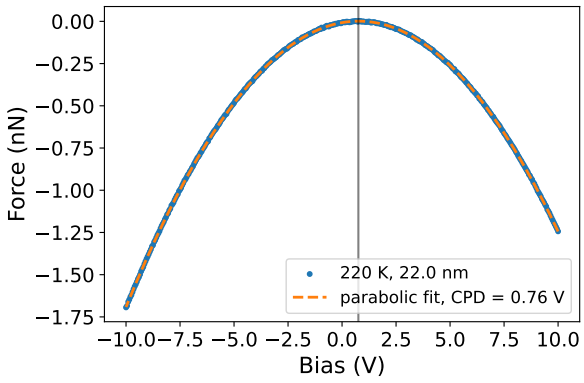

Figure 4.5: Representative force-bias curve with fit to Eq. 4.1 to determine V_{CPD}. We repeat this fitting at all z and report the average work function within each temperature in Fig. 4.6 using Eq. 3.18.

4.2.2 Measure the work function of VO_2 using CPD voltage

Based on Eq. 3.10 we expect an inverted parabola in the force-bias curves, offset from 0 V by the CPD voltage (see Sect. 3.6.2). At each fixed tip-sample separation we fit the force-bias curve to a parabola of the form

$$F(V_b) = -\alpha_F (V_b - V_{\text{CPD}})^2 + \beta_F \tag{4.1}$$

where α_F, V_{CPD}, and β_F are fit parameters, where $\alpha_F = -1/2\ \partial C/\partial z$ (Eq. 3.10) and β_F is due to the bias-independent vdW and repulsive forces (Eq. 3.11). An example fit shown in Fig. 4.5.

To calculate the work function of VO_2 we use Eq. 3.18, but we first need to determine the work function of the tip. We calibrate the work function of the

tip by performing the parabolic fitting from Eq. 4.1 on the z-V_b maps taken on a gold sample at 220 K. Au(111) has a known work function of 5.3 ± 0.06 eV[81], whereas amorphous gold can have a lower work function, of around 5.1 ± 0.1 eV[82]. Here, we take the work function of gold to be 5.2 ± 0.1 eV, and measure the CPD between the tip and gold to be 0.58 ± 0.06 V. Using these values we rearrange Eq. 3.17 to calculate the work function of the tip:

$$\begin{aligned} \Phi_{\text{tip}} &= \Phi_{\text{Au}} - eV_{\text{tip-Au}} \\ \Phi_{\text{tip}} &= 5.2 \pm 0.1 \text{ eV} - 0.58 \pm 0.06 \text{ eV} \\ \Phi_{\text{tip}} &= 4.6 \pm 0.1 \text{ eV}, \end{aligned} \tag{4.2}$$

which is similar to, but lower than, previously published work using Pt-Ir tips of 5.0 eV[80] and 4.86 eV[83].

At each T we take the average of the CPD from all z, and take the standard deviation to be the error. We then add the tip work function of 4.62 eV to calculate the work function of VO_2 at each temperature. In Fig. 4.6 we show the bulk transport for the Air Sample[†] (a) and the work function at each temperature in dark red in (b). We also report the work function from extracting the CPD from temperature sweep (cooling and warming), which has a finer tem-

[†]Air Sample is the copy sample for which we used the *ex situ* transport as a proxy for our *in situ* sample. For more information see Appendix A.

perature resolution, but may not be the exact temperature read on the thermocouple. This is our first evidence that we are observing the transition: the work function is ~ 0.2 eV higher in the insulating state than in the metallic state, and the drop in work function happens between 290 K and 300 K while warming. This change in the work function through the IMT is in great agreement with previous work using Kelvin probe force microscopy (KPFM) on a $VO_2(002)_R$ oriented film grown on TiO_2 (001)[80,84]. Rodríguez *et al* reported Φ_{VO_2} of 5.3 eV in the insulating state and 5.1 eV in the metallic state[80], and Sohn *et al.* reported Φ_{VO_2} of 5.1 eV in the insulating state and 4.95 eV in the metallic state[84].

We now investigate to the z dependence of the work function of VO_2 within each temperature. In Fig. 4.7 (a) we show the work function at each fixed z across all temperatures. Nominally, the work function is a static surface property, however, in our data we find it shifts slightly with tip-sample separation. Based on the temperature sweep, we expect a decrease in the work function of ~ 0.2 eV as the film transitions into the metallic state. We see little to no variation in the CPD at the two highest temperatures, 300 K and 315 K, potentially because these two samples are in the metallic state for the entire measurement, and thus we observe no change in the work function. Similarly, at 220 K we see

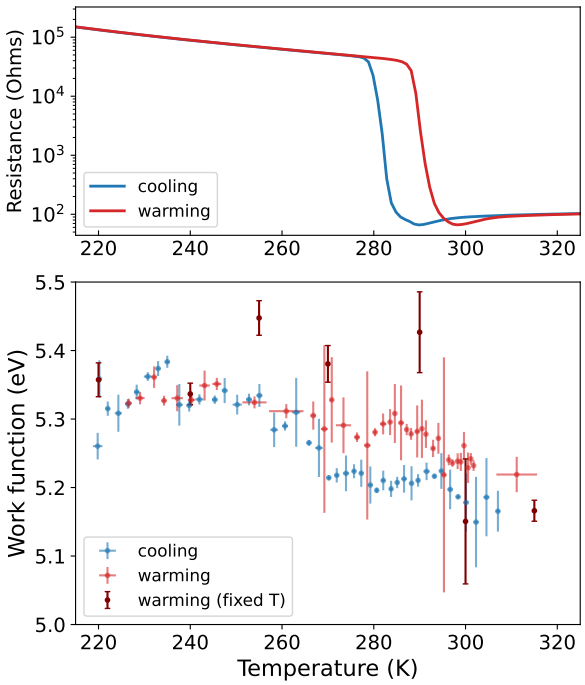

Figure 4.6: (a) Bulk transport of the Air Sample (the copy film), assumed to approximate the bulk transport of the film studied in vacuum throughout this Chapter. (b) The work function of VO_2 at each temperature, measured *in situ* and calculated by adding V_{CPD} and Φ_{tip} according to Eq. 3.18. V_{CPD} was extracted from force-bias curves by fitting to Eq. 4.1, and $\Phi_{\text{tip}} = 4.62$ eV (Eq. 4.2).

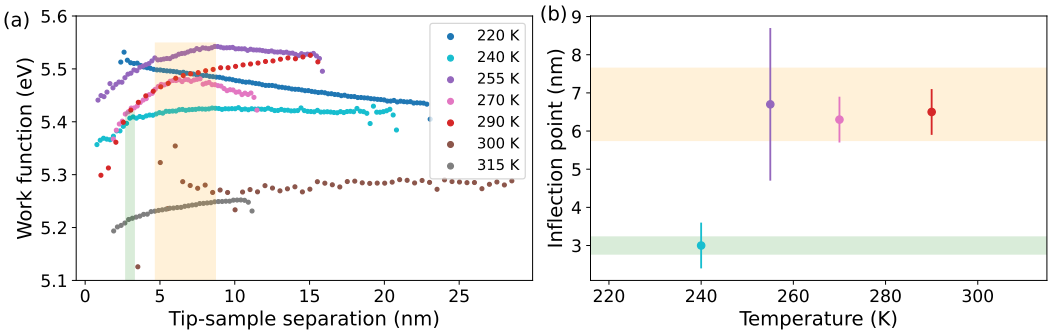

Figure 4.7: (a) The z dependence of the work function at each temperature, calculated by adding the V_{CPD} to the work function of the tip, according to Eq. 3.18. V_{CPD} was determined from fitting the force-bias curves to the Eq. 4.1 at each z. (b) The inflection point of the work function change at each temperature. We see no inflection at 220 K, 300 K, and 315 K due to the sample staying insulating (metallic) throughout the measurement at 220 K (300 K and 315 K). Measurements taken close to, but below the bulk T_{IMT} exhibit a lowering of the work function due to tip proximity. This effect is suppressed for lower temperatures, with the lowest temperature, 240 K, requiring a much closer z and therefore higher electric field, than the other temperatures.

no decrease in the work function, indicating the film is insulating for the full measurement. However at 240 K, 255 K, 270 K, and 290 K there is some z at which the work function starts to decrease. We tabulate the start of the work function inflection in Fig. 4.7 (b), picked out using panel (a). We find at 240 K a much closer z, and therefore higher field, is required than for 255 K, 270 K, and 290 K, which are closer the the bulk T_{IMT}.

4.2.3 Fit the tip-sample capacitance using force-bias curves

As discussed in Sect. 3.6.2, V_{CPD} is the voltage where there are no electrostatic forces. However, the z dependence to the work function indicates the field between the tip and sample may be playing a role in the changing work function.

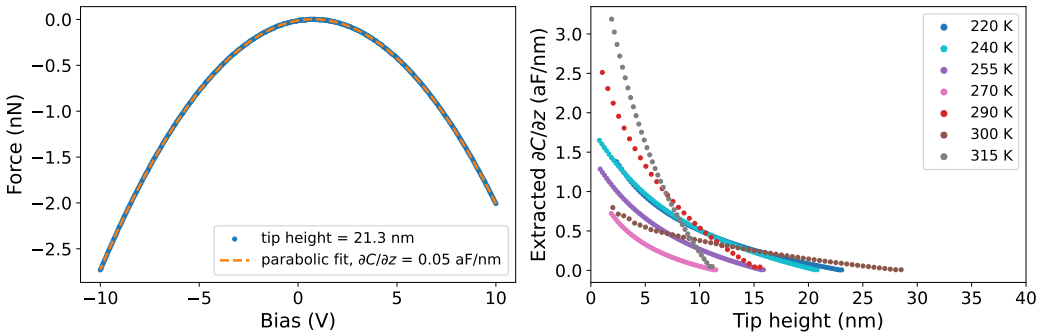

Figure 4.8: (a) Representative force-bias data with parabolic fit to Eq. 4.1 to determine $\partial C/\partial z$ at fixed z. (b) z dependence of the extracted $\partial C(z)/\partial z$ at each temperature.

In order to better understand the effects of the electric field we calculate the tip-sample capacitance which mediates the electric field between the tip and sample.

From the same parabolic fitting (Eq. 4.1), we now look at α_F at each z within each temperature, which is proportional to $\partial C/\partial z$. A representative fit is shown in Fig. 4.8 (a), with panel (b) showing the z dependence of $\partial C/\partial z$ at each temperature.

Next, we look to integrate $\partial C/\partial z$ over z to calculate the tip-sample capacitance. We notice that $\partial C/\partial z \rightarrow 0$ at the furthest measured z value of each temperature, however we expect $\partial C/\partial z \rightarrow 0$ as $z \rightarrow \infty$. This is due to the fact the the force is in integral of Δf over z, and so requires an integration factor at each V_b. Ideally, we would have measured out to further z values, where the Δf-bias sweep was truly flat, capturing $\partial C/\partial z \rightarrow 0$ within our data. As a work

around, we include an offset as a fitting parameter, C_{offset}. Another way to see the necessity of the offset is to start with the Δf-bias parabolas, and extract $\partial^2 C/\partial z^2$ in Eq. 3.13, where each integration stage requires an integration factor. After the first integration, without an integration factor, we recover the values extracted from fitting the force-bias parabolas, but need the integration factor to accurately report the values of $\partial C(z)/\partial z$.

Typically one assumes $\partial C/\partial z = -2\pi\epsilon_0 r_{\text{tip}}/z$, however this is an approximation of the capacitance for a sphere and a plane for $z << r_{\text{tip}}$[85]. While the approximation is valid for the z ranges we use, it means that the *value* of the integration will depend on how large of z we integrate to, since $\sim -1/z$ integrates to $\ln 1/z$ which is not bound.

To ensure the correct magnitude of the capacitance we model the tip as a sphere with conical sides and the sample as a plane, as shown in Fig. 4.9 (a). We include the conical sides of the tip because electrostatic forces are long range, so the sides of the tip can contribute a significant amount to the electrostatic forces measured. We use a model of the form

$$\frac{\partial C}{\partial z} = -2\pi\epsilon_0 \left[\frac{r_{\text{tip}}}{z} \frac{1}{1+\frac{z}{r_{\text{tip}}(1-\sin\theta)}} + \frac{1}{\ln^2 \tan\theta/2} \times \left(\ln\left[\frac{z + r_{\text{tip}}(1-\sin\theta)}{H + r_{\text{tip}}(1-\cot\theta)} \right] - 1 + \frac{1+1/\sin\theta}{1+\frac{z}{r_{\text{tip}}(1-\sin\theta)}} \right) \right] + C_{\text{offset}} \tag{4.3}$$

reported by de Voogd *et al.*[86] where θ is the opening of the cone, H is the height of the conical section of the tip and is equal to $W/\tan\theta$ where W is the maximum width of the cone, equal to the radius of the fully cylindrical part of the wire tip, as shown in Fig. 4.9 (a), and C_{offset} is the integration factor required from calculating the force from Δf through integration.

We fit the extracted $\partial C/\partial z$ to Eq. 4.3, treating θ, H and C_{offset} as fit parameters. We do not treat r_{tip} as a fit parameter, instead using the value determined through fitting the force-distance curves in Sect. 4.2.1. The fit at each temperature is shown in Fig. 4.9 (b), which has been offset by C_{offset}. We integrate the $\partial C/\partial z$ from closest z to 20 μm (to approximate $z \rightarrow \infty$), which is shown in Fig. 4.9 (c). Panel (d) shows the same C(z) data as panel (c) at a smaller scale to differentiate the z variation at the lower temperatures.

We calculate a tip-sample capacitance on the order of 100s aF for most temperatures, with 315 K having a tip-sample capacitance $\sim 2000aF$. Capacitances $\sim$ 100s aF is around two orders of magnitude larger than other literature values: $<$ 1 aF in both a pendulum[87] and cantilever geometry[88], $\sim$ 1 aF for a theoretical truncated cylindrical tip[89], or $\sim$ 2 aF for monolayer of mica[67]. We attribute the large difference to strong electrostatic forces from the conical sides of the tip.

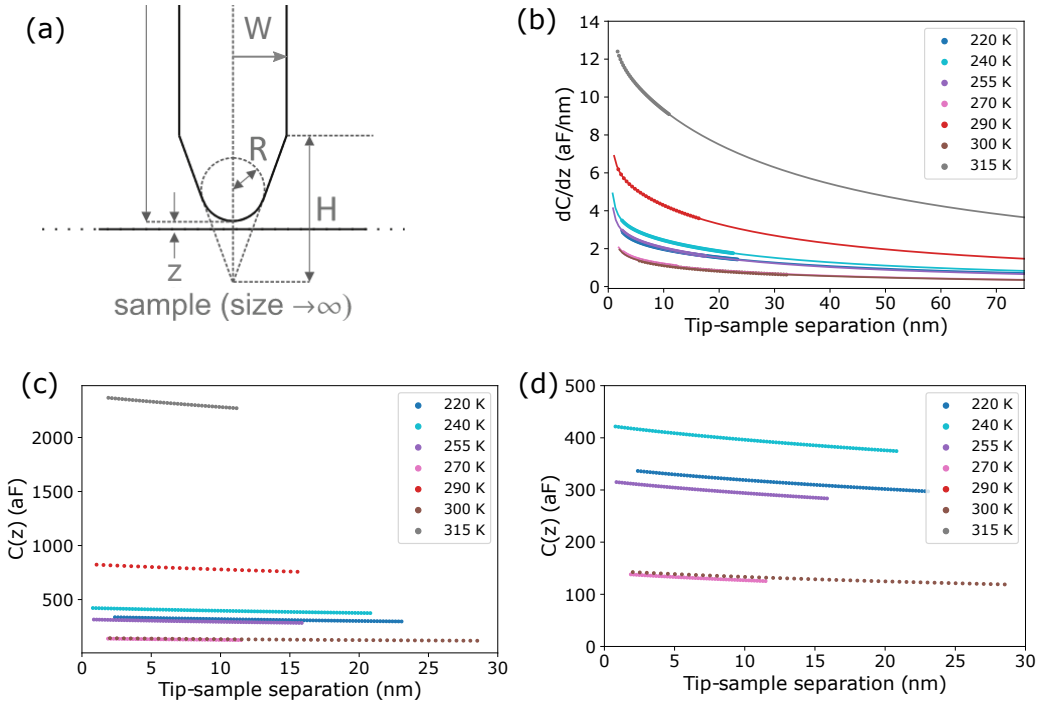

Figure 4.9: (a) Geometry of the tip considered to determine the tip-sample capacitance. (b) $\partial C(z)/\partial z + C_{\text{offset}}$ as a function of z, such that $\partial C(z)/\partial z \to 0$ as $z \to \infty$, determined through fitting to Eq. 4.3. (c) Integrated $\partial C(z)/\partial z$ from closest z to 20 μm. (d) Same data as (c), with a reduced y-axis scale to differentiate the low capacitances.

4.2.4 Carrier density

Next, we use the tip-sample capacitance at each z and $(V_b - V_{\mathrm{CPD}})$ to calculate the the charge induced within the sample (as discussed in Sect. 3.1, specifically Fig. 3.1 (c)), using $Q(z, V_b) = C(z)(V_b - V_{\mathrm{CPD}})$. To calculate the carrier density we define the region in the vicinity of the tip where the charge accumulates. We assume the radius of the induced charge is z independent over the z range we measure ($z < 30$ nm) and is equal to twice the tip radius, similar to the effective area assumed for a sphere-plane configuration with $z \sim r_{\mathrm{tip}}$[†]. We assume a constant depth of charge of 2 nm, or about 7 unit cells along c_R for each temperature[††]. Using this volume, we calculate the z and V_b dependent carrier density at each temperature. In Fig. 4.10 (a) we show the resulting carrier density at fixed $V_b - V_{\mathrm{CPD}} = 1$ V, and z at 3 nm, 8 nm, and 13 nm for each temperature. There is little z dependence on the carrier density over the z range measured. For all temperatures, we calculate a carrier density on the order of 10^{20} cm^{-3}, but see an increase of about 5× at higher temperatures starting around 290 K,

[†]At 300 K we estimate r_{tip} to be half that of the other temperatures, which affects the density calculation more than the other temperatures.

[††]We are currently working on some calculations that estimate the Debye length to be $\lesssim$ 1 nm. Here we use 2 nm to equal an integer number of unit cells. If the depth is the same at each temperature, then changing the depth is simply a linear re-scaling of the density. We may use a temperature-dependent depth if we can accurately model how it changes through the transition, which would affect each temperature differently.

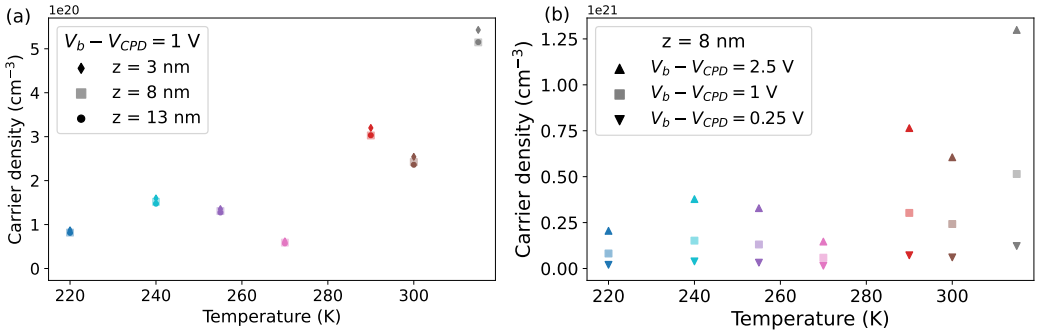

Figure 4.10: (a) z and (b) V_b dependence of the carrier density in the sample induced by the tip, calculated from fitting and integrating $\partial C/\partial z$ in Eq. 4.3, which were extracted from the force-bias curves using Eq. 4.1. We se a much stronger V_b dependence than z dependence in the induced charge. For fixed bias, we see a $\sim$5$\times$ increase in the induced carrier density at higher temperatures, starting at 290 K.

coinciding with the bulk T_{IMT}. This electron density is higher than reported carrier densities in the insulating state[30,90], and larger than carrier densities observed to trigger the transition[30]. Based on our calculated carrier density it is possible the field from the tip is inducing sufficient charge to cause the transition in the surface of the film below the bulk T_{IMT} of 290 K. Taken together with the z dependent work function (Sect. 4.2.2), these results corroborate that we observe the IMT, at least on the surface, as low as 240 K.

In Fig. 4.10 panel (b) we show the resulting charge density for fixed $z = 8$ nm and $V_b - V_{\mathrm{CPD}}$ at 0.25 V, 1 V, and 2.5 V, for each temperature. There is a much stronger V_b dependence than z dependence over the z range measured here. The general trend at fixed $V_b - V_{\mathrm{CPD}}$ across temperatures is preserved; we see a raised induced charge density by about 5$\times$ at higher temperatures, starting at 290 K.

We see the highest charge density at 315 K, with a maximum around 5×10^{21} cm^{-3} at 10 V. From the work function measurements we expect the sample to be fully metallic at this temperature, and the maximum induced charge density at 10 V is close to typical measured metallic state charge density of $\sim 10^{22}-10^{23}$ cm^{-3} [19,30].

4.3 Drive voltage: damping coefficient and dissipation

Having quantified the induced charge that has accumulated in the vicinity of the tip, we now consider the effects of the tip oscillating: Joule dissipation and the corresponding damping. We calculate the damping coefficient from measured V_{drive} as per Eq. 3.26, using tip-specific parameters for f_0 and Q determined through a frequency sweep (as in Fig. 3.2), and $k = 1800$ N/m. In Fig. 4.11 we show a representative damping-bias curve at $z = 8$ nm at each temperature. Based on Eq. 3.24 we expect up-right parabolic behavior in the damping-bias curves, however between 270 K and 300 K (around bulk T_{IMT}) we see inverted behavior; a curve that has the highest damping at low applied bias and comparatively lower damping at high applied bias.

In order to quantify the Joule damping coefficient we fit the damping-bias

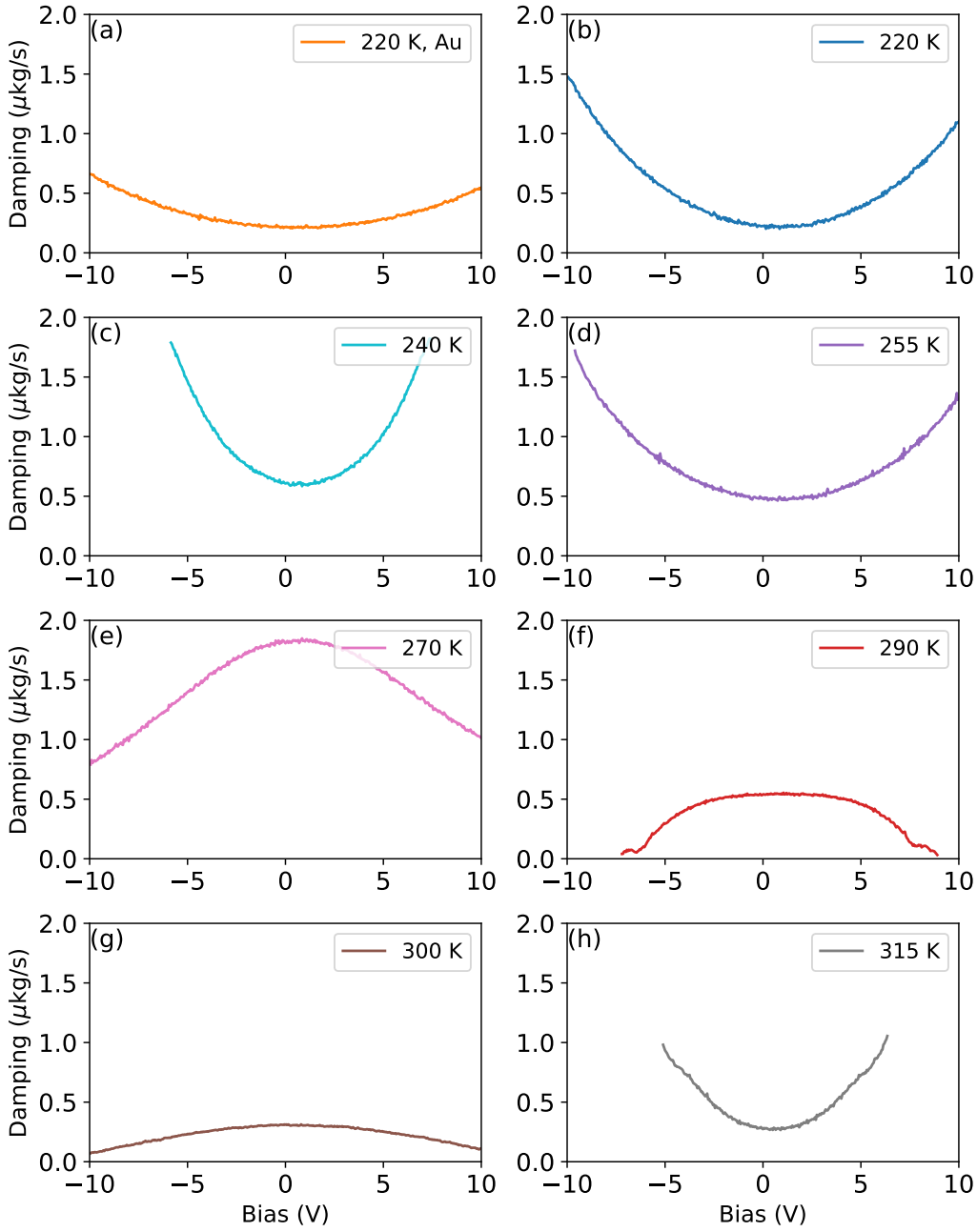

Figure 4.11: Calculated damping-bias curves for each temperature at $z = 8$ nm. (a) Damping on gold at 220 K, (b) - (h) Damping on VO_2 at: (b) 220 K, (c) 240 K, (d) 255 K, (e) 270 K, (f) 290 K, (g) 300 K, and (h) 315 K. These curves show and overall higher damping of 2 $\times 10^{-6}$ kg/s on VO_2 below 270 K, consistent with being in an insulating state, and lower damping above 290 K, consistent with being in a metallic state.

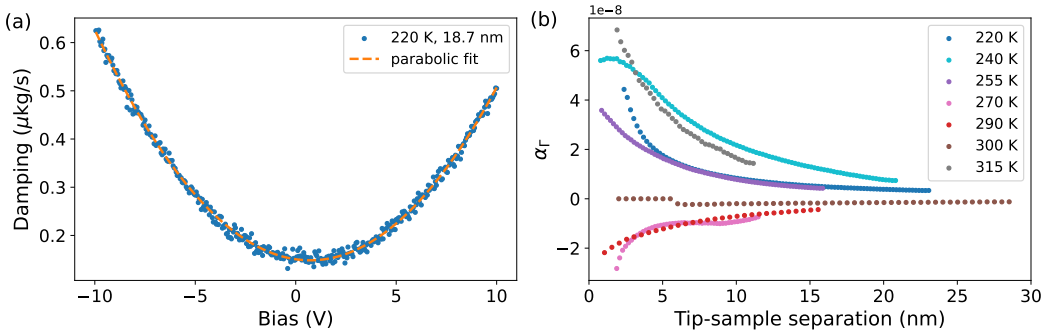

Figure 4.12: (a) A representative damping coefficient-bias curve with parabolic fit to the form Eq. 4.4. (b) z dependence of the quadratic fit parameter, α_Γ in Eq. 4.4, at each temperature. Nominally α_Γ is a positive fit parameter, suggesting we should reasses our assumptions, and take a closer look at the data from 270 K, 290 K, and 300 K.

curves to a parabola using the form

$$\Gamma(V_b) = \alpha_\Gamma(V_b - V_{\mathrm{CPD}})^2 + \beta_\Gamma, \tag{4.4}$$

where α_Γ, V_{CPD}, and β_Γ are positive fit parameters. Similar to the force-bias curves, the offset at β_Γ corresponds to damping due to vdW forces, which have no bias dependence[91]. We fit a parabola at each z and temperature, showing a representative fit Fig. 4.12 (a). In panel (b) we present the fit parameter α_Γ as a function of z at each temperature.

Both in the raw data in Fig. 4.11 and in the parabolic fit parameter extracted from the fits (Fig. 4.12 (b)), the damping parabola opens downwards between 270 K and 300 K (and therefore $\alpha_\Gamma < 0$). This is counter-intuitive to the logic of

Joule dissipation; larger biases induce more charges within the film, leading to higher Joule dissipation. We recall that the force-bias data followed the theory well; the capacitance gradient as a function of tip-sample spacing could be well modeled by Eq. 4.3. Therefore, we can be confident that within a bias sweep at fixed z the capacitance is constant and the carrier density in the sample larger at higher biases, precisely as shown in Fig. 4.10 (b). The final assumption it that more charges would cause higher Joule dissipation, which assumes the resistance is constant. The derivation for Joule dissipation assumed a constant resistance within a bias sweep, however based on previous discussions of the work function (Sect. 4.2.2) and carrier density (Sect. 4.2.4), we suspect VO_2 exhibits a an IMT around 290 K, resulting in a large drop in the resistance around this temperature, even within a bias sweep.

For the damping-bias curves where we observe inverted behavior, we conclude we observe a changing resistance; if the resistance is rapidly decreasing with applied bias the total Joule dissipation detected by the tip could also appear to decrease. One such example, with hypothetical vdW and Joule dissipation, is shown in Fig. 4.13. While this apparent $-V^2$ behavior can be shown to be consistent with a decreasing resistance, there are too many unknown parameters to accurately fit the data to this model and be confident in any extracted param-

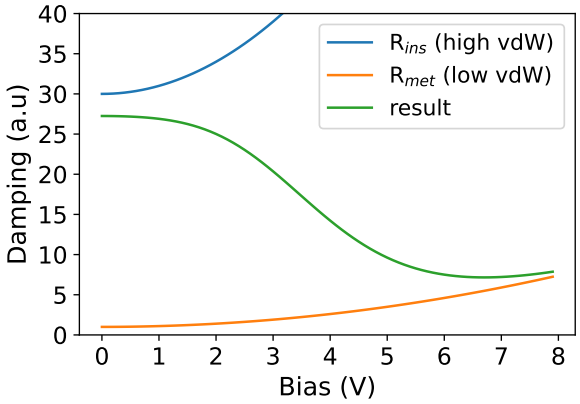

Figure 4.13: Theoretical damping coefficient as the result of a phase change within a bias sweep. The resistance is modeled as a sigmoid transition between the insulating and metallic state, with a factor of 10 resistance change between the states, occurring at 3 V with a 1 V width. This toy model also assumes a factor of 10 change in the vdW dissipation (resulting in a constant damping offset) between the insulating and metallic state.

eters (such as resistance change or threshold voltage). For example, the difference in vdW forces plays a large role in inverted parabola behavior shown here, but would be impossible to accurately fit without more information.

Because we may not be able to extract meaningful parameters from the parabolic fits at all temperatures, we look to the damping coefficient data for trends. Looking back at Fig. 4.11 we notice the maximum value of the damping coefficient at the lowest temperatures (nominally in the insulating state) is generally larger than the damping coefficient at higher temperatures.

In Fig. 4.14 we show the damping at various z and V_b, similar to the carrier density in Fig. 4.10. In panel (a) we show the damping coefficient at $V_b = V_{\mathrm{CPD}}$ for z at 3 nm, 8 nm, and 13 nm. We notice that the damping coefficient is $\sim$

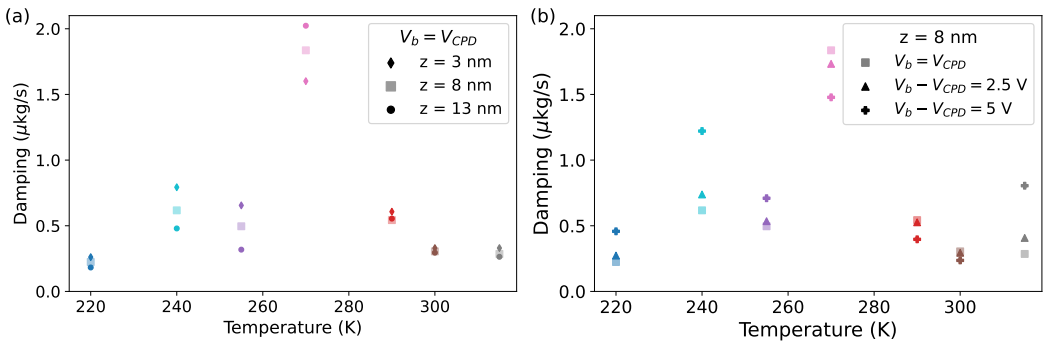

Figure 4.14: (a) Damping coefficient at $V_b = V_{\text{CPD}}$ and z at 3 nm, 8 nm, and 13 nm. We the damping has a stronger z-dependence at 240 K, 255 K, and 270 K; right below the bulk T_{IMT}. (b) Damping coefficient at $z = 8$ nm and V_b at V_{CPD}, V_{CPD}+ 2.5 V, and V_{CPD} +5 V. In the V_b dependence we again see inverted damping behavior 270 K, 290 K, and 300 K.

10^{-6} kg/s, which is on the same order of magnitude as reported by Hasan *et al.*[67]. We also see the damping is approximately 4× larger at 270 K than all the other temperatures at V_{CPD}, however this difference decreases both with z and V_b (shown in Fig. 4.14 (b)), indicating there is some non-Joule damping occurring at V_{CPD} at the 270 K that is less pronounced than the other temperatures. We also notice in Fig. 4.14 (a) that at 240 K, 255 K, and 270 K the damping has much stronger z dependence than at other temperatures, indicating that the damping measured at these temperatures is more strongly electric field dependent than at the other temperatures. Interestingly, these are the same temperatures, just below T_{IMT}, that showed the largest change in the work function with z as well (recall Fig. 4.6), more evidence that the proximity of the probe may be causing a partial transition in the surface of the film.

Finally, we look at the bias dependence of the damping coefficient, shown in Fig. 4.14, we fix z at 8 nm and increase V_b from V_{CPD} to $V_{\mathrm{CPD}}+5\mathrm{V}$. As expected from the raw data, increasing the bias at 270 K, 290 K, and 300 K results in a lower damping.

4.4 Conclusion

First, the decrease in average work function above 290 K (Fig. 4.6) suggests that we observe the IMT in VO_2. The damping at each temperature is also consistent with decreasing resistance between 270 K and 300 K, only slightly below the expected bulk T_{IMT} of 290 K. The lowered temperature measured via nc-AFM may be due to local variations within the sample, or it may be a result of the proximity of the probe and the resulting induced charge. The induced carrier doping that we calculate from the tip-sample capacitance increases at temperatures above 290 K, consistent with the metallic state (Fig. 4.10). Our calculated induced charge in the insulating state is consistent with previously reported threshold densities reported to cause the transition[30]. To further study the effect of the electric field we look to the z dependence of the work function and damping. The z dependence of the work function shows a decrease at close z for temperatures as low as 240 K (Fig. 4.7), suggesting that close tip prox-

imity and the resulting high electric field can initiate the transition, at least in the surface of the film, below the bulk T_{IMT}. Additionally, the z dependence of the damping (Fig. 4.14) demonstrates a stronger z dependence on the damping between 240 K and 270 K as compared to the other temperatures, consistent with the changing work function with z results, and reinforcing the idea that the probe itself is instigating some aspects of transition, such as decreasing the work function, at close z and up to 50 K below the bulk T_{IMT}.

A

Ex situ characterization of the film studied via nc-AFM

Scanning probe techniques, such as nc-AFM, are highly surface sensitive. As such, if possible, samples will be grown in vacuum then transferred to the microscope entirely in vacuum to prohibit carbon or oxygen from contaminating

the surface of the sample. This is precisely what we did; we grew the sample in vacuum using MBE, then transferred it to the UHV of the nc-AFM entirely *in situ*. However, we did not have the capability to pattern contacts and perform transport measurements *in situ* to confirm a bulk IMT. We therefore grew two samples on the same day under the same growth conditions; the first was removed from vacuum to perform *ex situ* film characterization and the second was transferred to the microscope. The first of which, called the Air Sample, was removed from vacuum and the film characterization techniques described in Chapter 2 were performed: XRD, XRR, transport, and tapping AFM. All measurements confirmed the sample was VO_2, and showed a 3 order of magnitude transition in the resistance around 290 K. The second growth, called the Vacuum Sample, was then transferred *in situ* to the RHK, and is the sample studied with nc-AFM in Chapter 4.

Fig. A.1 and Table A.1 outline the timeline of events for both of these samples. These samples were grown in June 2021, and the Air sample was immediately removed from vacuum and bulk characterization measurements were performed: XRD, XRR, AFM topography, and preliminary transport was performed by reading the voltage from a *Keithly* while the sample was cooled to 270 K in a freezer. A year after growth we used a liquid nitrogen dipper probe

to more accurately measure the transition on the Air Sample.

In the mean time, we collected two sets of temperature-dependent, z-V_b data on the Vacuum Sample only a few months after growth. However these data sets had some drawbacks, the largest of which is that we never reached sufficiently high temperature to reach the expected bulk metallic behavior in the VO_2 sample. In the fall of 2022 the RHK underwent repairs that required a vent. To keep the Vacuum Sample free of contaminants from the atmosphere we transferred the sample to a glove box for less than two weeks. It was then loaded back into the RHK and the third, and final set of temperature-dependent, z-V_b measurements were performed, this time reaching a definite metallic state temperature of 315 K. The sample was removed from the RHK, believing vacuum measurements were complete. After some preliminary analysis on the data from fall 2022, we decided to verify the inverted dissipation spectroscopy observed at 270 K and 290 K. The Vacuum Sample was loaded back into the RHK chamber, without a bake, and data was collected at 300 K. We first measured on HOPG, then switched to the Vacuum Sample. This data was consistent with the 290 K behavior on VO_2, confirming the inverted dissipation behavior. The Vacuum Sample we removed again, and a short time later bulk characterization was performed.

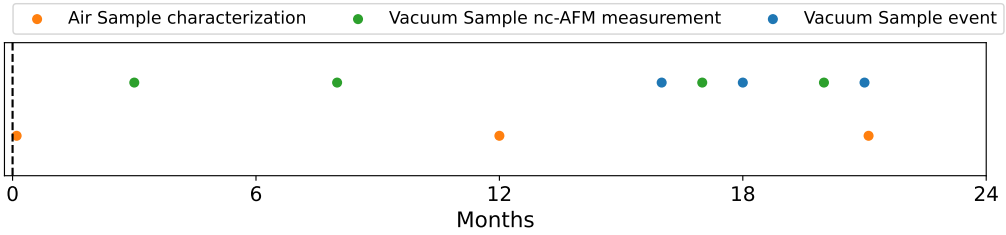

Figure A.1: Timeline of the Air and Vacuum Samples.

Month, Year	event
June, 2021	Both Air Sample and Vacuum Sample grown using oxide MBE
June, 2021	XRD, XRR, AFM topography and preliminary transport collected on Air Sample.
Sept, 2021	Preliminary nc-AFM data collected on Vacuum Sample. Highest $T = 286K$, The data collection was non-monotonic in temperature
Feb, 2022	Secondary nc-AFM data collected on Vacuum Sample. Highest $T = 297K$.
June, 2022	Transport data collected on Air Sample using a liquid nitrogen dipper.
Oct, 2022	Vacuum Sample transported to a glove box for repairs on RHK requiring a vent.
Nov, 2022	Final nc-AFM data collected on Vacuum Sample, presented in Ch. 4.
Dec, 2022	Vacuum Sample removed from vacuum and placed in a desiccator
Feb 2023	Vacuum Sample re-loaded and data at 300 K is collected. Vacuum Sample removed from vacuum.
March 2023	XRD, XRR, AFM topography and transport (PPMS) performed on Vacuum sample.
March 2023	Transport (PPMS) performed on Air Sample.

Table A.1: Timeline of the Air and Vacuum Samples.

After measuring transport on the Vacuum Sample, we re-measured the resistance of the Air Sample once more using the PPMS, confirming it still showed a transition.

First we show the XRD and transport results for the Air Sample in Fig. A.2 taken June 2021 and March 2023 respectively, which we show in Chapter 4 as an approximation of the bulk properties of the Vacuum Sample.

Over the course of 20 months we performed three separate transport measurements on the Air Sample, all of which show an almost 3 order of magnitude change in the the resistance at 290 K. In Fig. A.3 we show all three transport

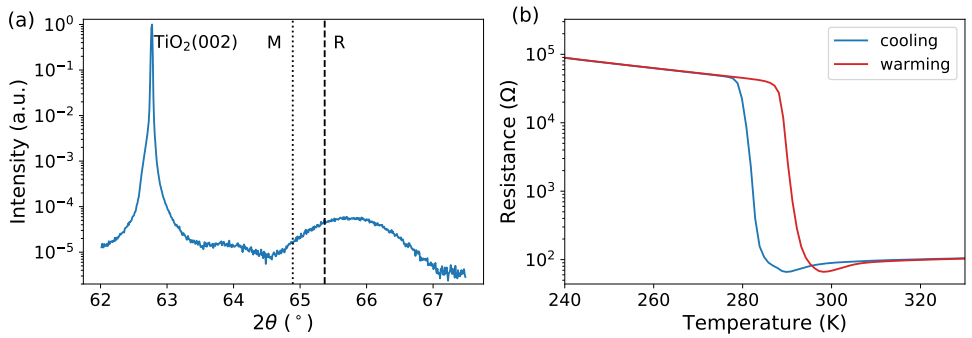

Figure A.2: Characterization of the Air Sample showing VO_2 with a 3 order of magnitude IMT. (a) XRD for the Air sample with the peak position for bulk $VO_2(40\bar{2})_M$ ($VO_2(002)_R$) marked with a dotted (dashed) black line and labeled with 'M' ('R'). The peak in the data is consistent with $VO_2(002)_R$. (b) Transport showing a 3 order of magnitude transition centered at 290.5 K (warming).

measurements taken on the Air Sample. First resistance measurements were taken in June 2021, immediately after growth, by reading the voltage from a *Keithly* while the sample was cooled to 270 K in a freezer, which we assumed to be a good approximation of the characteristics of the Vacuum Sample inside the RHK. Second, transport measurements were performed in June 2022 with a liquid nitrogen dipper connected to a computer, which more accurately read the temperature and resistance. Finally, the resistance was re-measured at the same time as Vacuum Sample using a PPMS. All of these resistance measurements are very consistent with each other, meaning there has been little to no change in the film over the course of almost two years stored in a desiccator at ambient pressure and temperature.

After the nc-AFM measurements were taken, we removed the Vacuum Sam-

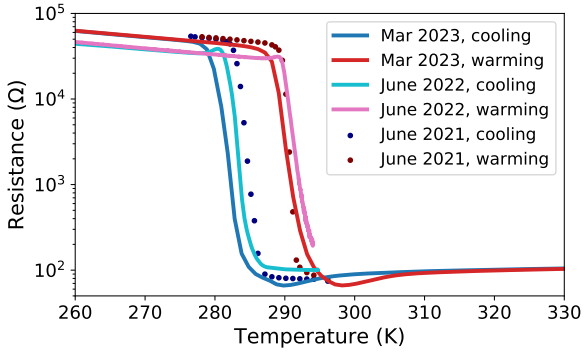

Figure A.3: Transport on the Air Sample over the course of almost two years, showing extremely consistent resistance measurements over three different modes of measurement: manually reading a *Keithly* in June 2021, a liquid nitrogen dipper in June 2022, and a PPMS in March 2023.

ple from UHV and performed XRD, XRR, AFM topography, and transport. In Fig. A.4 we show the XRD and the transport, both taken March 2023. Unfortunately, we do not observe a peak in the XRD corresponding to $VO_2(002)_R$ or $VO_2(40\bar{2})_M$ nor a bulk transition in the transport of the Vacuum Sample between 200 K and 360 K.

In Fig. A.5 we look at the XRD of both samples more closely, and confirm that in the Vacuum Sample there are no peaks, and so there is no crystallized film at the time of the XRD measurement. The Air Sample data is from June 2021, and shows one peak corresponding to $VO_2(002)_R$, indicating the film is single-phase VO_2.

The XRR on both samples are shown in Fig. 2.3, which was taken in June 2021 for the Air Sample and March 2023 for the Vacuum Sample. The XRR on

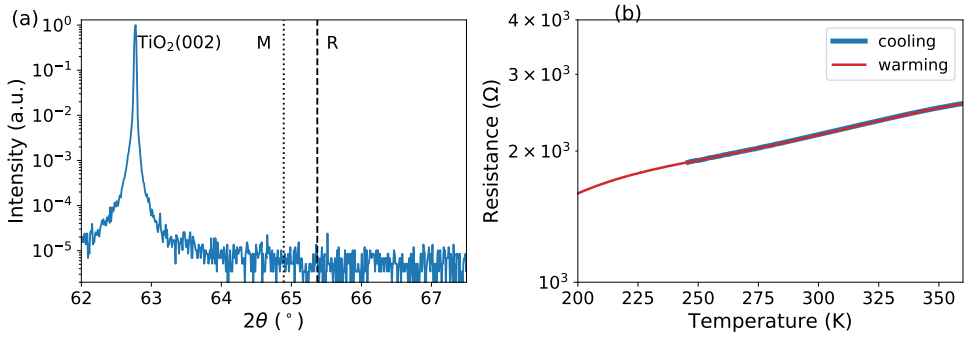

Figure A.4: XRD and transport characterization of the Vacuum Sample. (a) XRD of the region we expect to see the $VO_2(002)_R$ peak, with the peak position for bulk $VO_2(40\bar{2})_M$ ($VO_2(002)_R$) marked with a dotted (dashed) black line and labeled with 'M' ('R'). The data for the Vacuum Sample shows noise, indicating there is no crystallized film. (b) Transport showing no IMT, only 2-3 kΩ resistance between 200 K and 360 K.

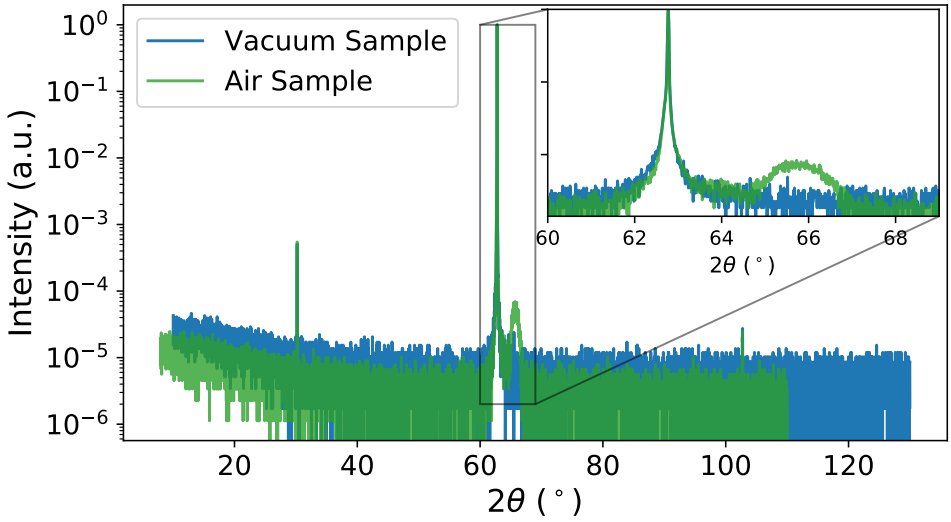

Figure A.5: Full XRD of both the Air Sample and Vacuum sample. The Vacuum sample shows no peaks besides substrate peaks, indicating there is no crystallized film at the time of measurement. The Air Sample shows only the $VO_2(002)_R$ peak in addition to the substrate peak. Inset: zoom of 60° to 70°, highlighting the region where we expect the $VO_2(002)_R$ peak.

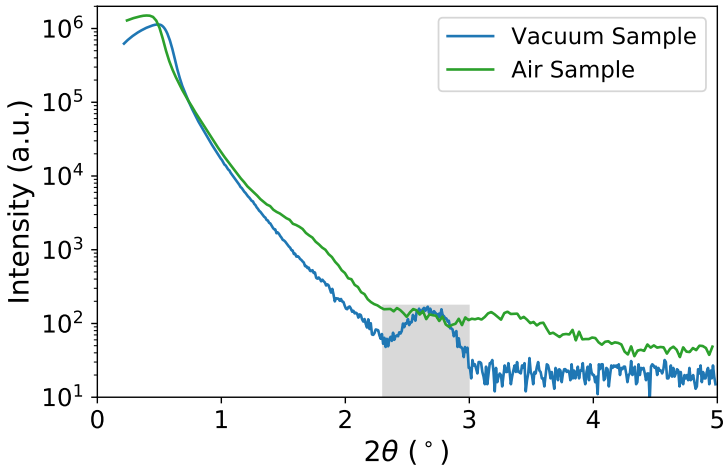

Figure A.6: XRR of both the Air and Vacuum sample. The XRR on the Air Sample shows some large, shallow peaks and valleys, indicative of a thin film at a similar density to the substrate. The XRR on the Vacuum Sample shows only exponential decay, indicating the film is either very thin or very rough, or both. The feature between 2.3° and 3° which has been greyed out, is an instrumentation artifact which we observe in many samples. It is not related to thickness fringes.

the Vacuum Sample shows only exponential decay, which indicates the film is either very thin or very rough, or both.

Finally, in Fig. A.7 we compare AFM topographies between the two samples, taken in air operating in tapping mode. On the Air Sample the topographies were taken in June 2021, on the Vacuum sample they were taken in April 2023. The topographies of the two samples appear similar, and indicate that some material was deposited on the Vacuum Sample, even if both x-ray measurements do no see corresponding peaks.

From all of this, we suspect we grew VO_2 in June 2021, but either being stored in vacuum for an extended period of time, or the process loading/unloading de-

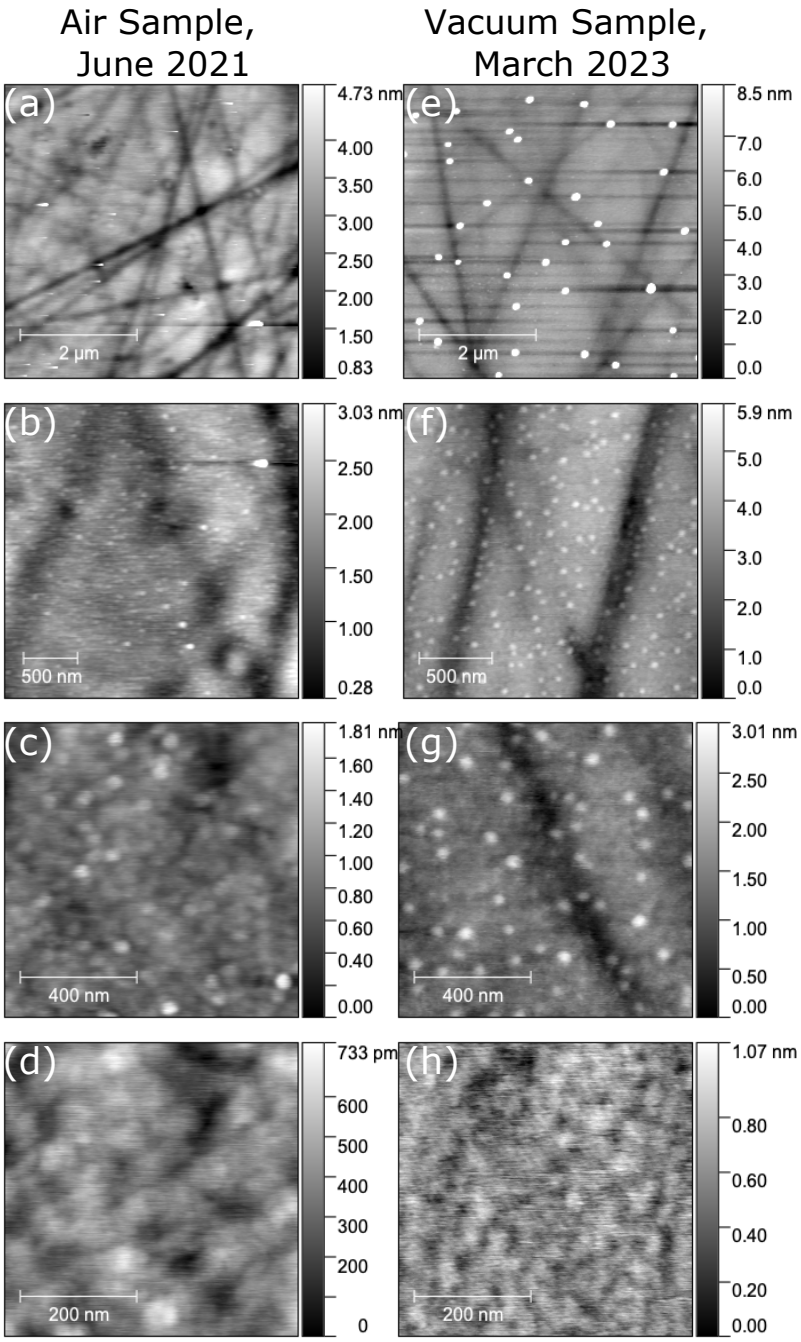

Figure A.7: (a)-(d) tapping AFM topography on the Air Sample at (a) 5 μm square, (b) 2.5 μm square, (c) 1 μm square and (d) 500 nm square areas. (e)-(h) tapping AFM topography on the Vacuum Sample at (e) 5 μm square, (f) 2 μm square, (g) 1 μm square and (h) 500 nm square areas. The topographies between the two samples appear consistent.

stroyed or changed the film enough to not exhibit a transition. We can possibly use the nc-AFM data collected in closer to the growth date to search for a transition, even if the data sets are incomplete. We are also thinking of other ways to confirm the Vacuum Sample is VO_2 and exhibited a transition while in the RHK in fall 2022.

References

[1] F. J. Morin. Oxides which show a metal-to insulator transition at the Néel temperature. *Physical Review Letters*, 3(1):34–36, July 1959.

[2] John B. Goodenough. The two components of the crystallographic transition in VO_2. *Journal of Solid State Chemistry*, 3(4):490–500, November 1971.

[3] J. P. Pouget, H. Launois, T. M. Rice, P. Dernier, A. Gossard, G. Villeneuve, and P. Hagenmuller. Dimerization of a linear Heisenberg chain in the insulating phases of $V_{1-x}Cr_xO_2$. *Physical Review B*, 10(5):1801–1815, September 1974.

[4] A. L. Pergament, G. B. Stefanovich, N. A. Kuldin, and A. A. Velichko. On the Problem of Metal-Insulator Transitions in Vanadium Oxides. *ISRN Condensed Matter Physics*, 2013:1–6, July 2013.

[5] K. D. Rogers. An X-ray diffraction study of semiconductor and metallic vanadium dioxide. *Powder Diffraction*, 8(4):240–244, 1993.

[6] Jae Hyung Park, Jim M. Coy, T. Serkan Kasirga, Chunming Huang, Zaiyao Fei, Scott Hunter, and David H. Cobden. Measurement of a solid-state triple point at the metal–insulator transition in VO_2. *Nature*, 500(7463):431–434, August 2013.

[7] Hubert Jerominek, Francis Picard, Nicholas R. Swart, Martin Renaud, Marc Levesque, Mario Lehoux, Jean-Sebastien Castonguay, Martin Pelletier, Ghislain Bilodeau, Danick Audet, Timothy D. Pope, and Philippe Lambert. Micromachined uncooled VO_2-based IR bolometer arrays. In *Infrared Detectors and Focal Plane Arrays IV*, volume 2746, pages 60–71. SPIE, June 1996.

[8] Gang Xu, Ping Jin, Masato Tazawa, and Kazuki Yoshimura. Optimization of antireflection coating for VO_2-based energy efficient window. *Solar Energy Materials and Solar Cells*, 83(1):29–37, June 2004.

[9] Xi Zhou, Liang Zhao, Weili Zhen, Yinyue Lin, Chunlin Wang, Tianyu Pan, Le Li, Guanlin Du, Linfeng Lu, Xun Cao, and Dongdong Li. Phase-Transition-Induced VO_2 Thin Film IR Photodetector and Threshold Switching Selector for Optical Neural Network Applications. *Advanced Electronic Materials*, 7(5):2001254, 2021.

[10] Minah Seo, Jisoo Kyoung, Hyeongryeol Park, Sukmo Koo, Hyun-sun Kim, Hannes Bernien, Bong Jun Kim, Jong Ho Choe, Yeong Hwan Ahn, Hyun-Tak Kim, Namkyoo Park, Q-Han Park, Kwangjun Ahn, and Dai-sik Kim. Active Terahertz Nanoantennas Based on VO_2 Phase Transition. *Nano Letters*, 10(6):2064–2068, June 2010.

[11] Shengxiang Wang, Lei Kang, and Douglas H. Werner. Hybrid Resonators and Highly Tunable Terahertz Metamaterials Enabled by Vanadium Dioxide (VO_2). *Scientific Reports*, 7(1):4326, June 2017.

[12] Sung-Hwan Bae, Sangmin Lee, Hyun Koo, Long Lin, Bong Hyun Jo, Chan Park, and Zhong Lin Wang. The Memristive Properties of a Single VO_2 Nanowire with Switching Controlled by Self-Heating. *Advanced Materials*, 25(36):5098–5103, 2013.

[13] M. Nakano, K. Shibuya, D. Okuyama, T. Hatano, S. Ono, M. Kawasaki, Y. Iwasa, and Y. Tokura. Collective bulk carrier delocalization driven by electrostatic surface charge accumulation. *Nature*, 487(7408):459–462, July 2012.

[14] Parker Schofield, Adelaide Bradicich, Rebeca M. Gurrola, Yuwei Zhang, Timothy D. Brown, Matt Pharr, Patrick J. Shamberger, and Sarbajit Banerjee. Harnessing the Metal–Insulator Transition of VO_2 in Neuromorphic Computing. *Advanced Materials*, n/a(n/a):2205294, August 2022.

[15] Lele Fan, Yuliang Chen, Qianghu Liu, Shi Chen, Lei Zhu, Qiangqiang Meng, Baolin Wang, Qinfang Zhang, Hui Ren, and Chongwen Zou. Infrared Response and Optoelectronic Memory Device Fabrication Based on Epitaxial VO_2 Film. *ACS Applied Materials & Interfaces*, 8(48):32971–32977, December 2016.

[16] Luca Pellegrino, Nicola Manca, Teruo Kanki, Hidekazu Tanaka, Michele Biasotti, Emilio Bellingeri, Antonio Sergio Siri, and Daniele Marré. Multistate Memory Devices Based on Free-standing VO_2/TiO_2 Microstruc-

tures Driven by Joule Self-Heating. *Advanced Materials*, 24(21):2929–2934, 2012.

[17] Y. Muraoka and Z. Hiroi. Metal–insulator transition of VO_2 thin films grown on TiO_2 (001) and (110) substrates. *Applied Physics Letters*, 80(4):583–585, January 2002.

[18] Kazuki Nagashima, Takeshi Yanagida, Hidekazu Tanaka, and Tomoji Kawai. Stress relaxation effect on transport properties of strained vanadium dioxide epitaxial thin films. *Physical Review B*, 74(17):172106, November 2006.

[19] J. Jeong, N. Aetukuri, T. Graf, T. D. Schladt, M. G. Samant, and S. S. P. Parkin. Suppression of metal-insulator transition in VO_2 by electric field-induced oxygen vacancy formation. *Science*, 339(6126):1402–1405, March 2013.

[20] Hanjong Paik, Jarrett A. Moyer, Timothy Spila, Joshua W. Tashman, Julia A. Mundy, Eugene Freeman, Nikhil Shukla, Jason M. Lapano, Roman Engel-Herbert, Willi Zander, Jürgen Schubert, David A. Muller, Suman Datta, Peter Schiffer, and Darrell G. Schlom. Transport properties of ultra-thin VO_2 films on (001) TiO_2 grown by reactive molecular-beam epitaxy. *Applied Physics Letters*, 107(16):163101, October 2015.

[21] Renhui Yang, Zhiming Wu, Chunhui Ji, Xuefei Wu, Zihao Xiang, Fan Zhang, Weizhi Li, Jun Wang, Xiang Dong, and Yadong Jiang. Far-IR transmittance and metal–insulator phase transition properties of VO_2 films using Al_2O_3 as buffer layer. *Journal of Materials Science: Materials in Electronics*, 30(7):6448–6458, April 2019.

[22] Jianwei Ma, Gang Xu, Lei Miao, Masato Tazawa, and Sakae Tanemura. Thickness-Dependent Structural and Optical Properties of VO_2 Thin Films. *Japanese Journal of Applied Physics*, 50(2):020215, February 2011.

[23] Gang Xu, Ping Jin, Masato Tazawa, and Kazuki Yoshimura. Thickness dependence of optical properties of VO_2 thin films epitaxially grown on sapphire (0001). *Applied Surface Science*, 244(1-4):449–452, May 2005.

[24] N. F. Quackenbush, J. W. Tashman, J. A. Mundy, S. Sallis, H. Paik, R. Misra, J. A. Moyer, J.-H. Guo, D. A. Fischer, J. C. Woicik, D. A.

Muller, D. G. Schlom, and L. F. J. Piper. Nature of the metal insulator transition in ultrathin epitaxial vanadium dioxide. *Nano Letters*, 13(10):4857–4861, October 2013.

[25] Byung-Gyu Chae, Hyun-Tak Kim, Doo-Hyeb Youn, and Kwang-Yong Kang. Abrupt metal–insulator transition observed in VO_2 thin films induced by a switching voltage pulse. *Physica B: Condensed Matter*, 369(1-4):76–80, December 2005.

[26] Zheng Yang, Sean Hart, Changhyun Ko, Amir Yacoby, and Shriram Ramanathan. Studies on electric triggering of the metal-insulator transition in VO_2 thin films between 77 K and 300 K. *Journal of Applied Physics*, 110(3):033725, August 2011.

[27] Alyson Spitzig, Adam Pivonka, Alex Frenzel, Jeehoon Kim, Changhyun Ko, You Zhou, Eric Hudson, Shriram Ramanathan, Jennifer E. Hoffman, and Jason D. Hoffman. Nanoscale thermal imaging of VO_2 via Poole–Frenkel conduction. *Applied Physics Letters*, 120(15):151602, April 2022.

[28] G. M. Liao, S. Chen, L. L. Fan, Y. L. Chen, X. Q. Wang, H. Ren, Z. M. Zhang, and C. W. Zou. Dynamically tracking the joule heating effect on the voltage induced metal-insulator transition in VO_2 crystal film. *AIP Advances*, 6(4):045014, April 2016.

[29] Petr Markov, Robert E. Marvel, Hiram J. Conley, Kevin J. Miller, Richard F. Haglund, and Sharon M. Weiss. Optically Monitored Electrical Switching in VO_2. *ACS Photonics*, 2(8):1175–1182, August 2015.

[30] G Stefanovich, A Pergament, and D Stefanovich. Electrical switching and Mott transition in VO_2. *Journal of Physics: Condensed Matter*, 12(41):8837–8845, October 2000.

[31] Jiyu Xu, Daqiang Chen, and Sheng Meng. Decoupled ultrafast electronic and structural phase transitions in photoexcited monoclinic VO_2. *Science Advances*, 8(44):eadd2392, November 2022.

[32] A. Cavalleri, Cs. Tóth, C. W. Siders, J. A. Squier, F. Ráksi, P. Forget, and J. C. Kieffer. Femtosecond Structural Dynamics in VO_2 during an Ultrafast Solid-Solid Phase Transition. *Physical Review Letters*, 87(23):237401, November 2001.

[33] Michael F. Becker, A. Bruce Buckman, Rodger M. Walser, Thierry Lépine, Patrick Georges, and Alain Brun. Femtosecond laser excitation of the semiconductor-metal phase transition in VO_2. *Applied Physics Letters*, 65(12):1507–1509, September 1994.

[34] F.H. Chen, L. L. Fan, S. Chen, G. M. Liao, Y. L. Chen, P. Wu, Li Song, C. W. Zou, and Z. Y. Wu. Control of the Metal–Insulator Transition in VO_2 Epitaxial Film by Modifying Carrier Density. *ACS Applied Materials & Interfaces*, 7(12):6875–6881, April 2015.

[35] Renata M. Wentzcovitch, Werner W. Schulz, and Philip B. Allen. VO_2: Peierls or Mott-Hubbard? A view from band theory. *Physical Review Letters*, 72(21):3389–3392, May 1994.

[36] T. M. Rice, H. Launois, and J. P. Pouget. Comment on "VO_2: Peierls or Mott-Hubbard? A View from Band Theory". *Physical Review Letters*, 73(22):3042–3042, November 1994.

[37] F. Grandi, A. Amaricci, and M. Fabrizio. Unraveling the Mott-Peierls intrigue in vanadium dioxide. *Physical Review Research*, 2(1):013298, March 2020.

[38] L. Fratino, S. Bag, A. Camjayi, M. Civelli, and M. Rozenberg. Doping-driven resistive collapse of the Mott insulator in a minimal model for VO_2. *Physical Review B*, 105(12):125140, March 2022.

[39] J. Laverock, A. R. H. Preston, D. Newby, K. E. Smith, S. Sallis, L. F. J. Piper, S. Kittiwatanakul, J. W. Lu, S. A. Wolf, M. Leandersson, and T. Balasubramanian. Photoemission evidence for crossover from Peierls-like to Mott-like transition in highly strained VO_2. *Physical Review B*, 86(19):195124, November 2012.

[40] N.W. Ashcroft and N.D. Mermin. *Solid State Physics*. Holt-Saunders, 1976.

[41] D. B. McWhan, A. Menth, J. P. Remeika, W. F. Brinkman, and T. M. Rice. Metal-Insulator Transitions in Pure and Doped V_2O_3. *Physical Review B*, 7(5):1920–1931, March 1973.

[42] W. A. Little. Possibility of Synthesizing an Organic Superconductor. *Physical Review*, 134(6A):A1416–A1424, June 1964.

[43] Cédric Weber, David D. O' Regan, Nicholas D. M. Hine, Mike C. Payne, Gabriel Kotliar, and Peter B. Littlewood. Vanadium Dioxide: A Peierls-Mott Insulator Stable against Disorder. *Physical Review Letters*, 108(25):256402, June 2012.

[44] O. Nájera, M. Civelli, V. Dobrosavljević, and M. J. Rozenberg. Multiple crossovers and coherent states in a Mott-Peierls insulator. *Physical Review B*, 97(4):045108, January 2018.

[45] Salinporn Kittiwatanakul, Stuart A. Wolf, and Jiwei Lu. Large epitaxial bi-axial strain induces a Mott-like phase transition in VO_2. *Applied Physics Letters*, 105(7):073112, August 2014.

[46] Dooyong Lee, Donghyuk Yang, Hyegyeong Kim, Jiwoong Kim, Sehwan Song, Kyoung Soon Choi, Jong-Seong Bae, Jouhahn Lee, Jaekwang Lee, Yunsang Lee, Jiafeng Yan, Jaeyong Kim, and Sungkyun Park. Deposition-Temperature-Mediated Selective Phase Transition Mechanism of VO_2 Films. *The Journal of Physical Chemistry C*, 124(31):17282–17289, August 2020.

[47] Jin-Yi Miao, Wen-Xuan Wang, Zhen-Yi Jiang, Xiao-Dong Zhang, Ji-Ming Zheng, and Aijun Du. A theoretical study on pseudo Mott phase transition of vanadium dioxide. *Physical Chemistry Chemical Physics*, 25(1):759–767, December 2022.

[48] Chen Ling, Qianchen Wang, Xiaoqian Wang, Zhengjing Zhao, Zongguo Wang, Jingbo Li, Yongjie Zhao, and Haibo Jin. Hole Dopants Disentangling Peierls–Mott Relevance States of VO_2 by First-Principles Calculation. *The Journal of Physical Chemistry C*, 125(10):5816–5823, March 2021.

[49] In-Hui Hwang, Chang-In Park, Sunmog Yeo, Cheng-Jun Sun, and Sang-Wook Han. Decoupling the metal insulator transition and crystal field effects of VO_2. *Scientific Reports*, 11(1):3135, February 2021.

[50] D. Shiga, B. E. Yang, N. Hasegawa, T. Kanda, R. Tokunaga, K. Yoshimatsu, R. Yukawa, M. Kitamura, K. Horiba, and H. Kumigashira. Thickness dependence of electronic structures in VO_2 ultrathin films: Suppression of the cooperative Mott-Peierls transition. *Physical Review B*, 102(11):115114, September 2020.

[51] J. W. Tashman, J. H. Lee, H. Paik, J. A. Moyer, R. Misra, J. A. Mundy, T. Spila, T. A. Merz, J. Schubert, D. A. Muller, P. Schiffer, and D. G. Schlom. Epitaxial growth of VO_2 by periodic annealing. *Applied Physics Letters*, 104(6):063104, February 2014.

[52] Koen Martens, Nagaphani Aetukuri, Jaewoo Jeong, Mahesh G. Samant, and Stuart S. P. Parkin. Improved metal-insulator-transition characteristics of ultrathin VO_2 epitaxial films by optimized surface preparation of rutile TiO_2 substrates. *Applied Physics Letters*, 104(8):081918, February 2014.

[53] Qiyang Lu, Changhee Sohn, Guoxiang Hu, Xiang Gao, Matthew F. Chisholm, Ilkka Kylänpää, Jaron T. Krogel, Paul R. C. Kent, Olle Heinonen, P. Ganesh, and Ho Nyung Lee. Metal–insulator transition tuned by oxygen vacancy migration across TiO_2/VO_2 interface. *Scientific Reports*, 10(1):18554, October 2020.

[54] Kunio Okimura, Joe Sakai, Masashi Kuwahara, Mustapha Zaghrioui, and Yoichi Uehara. Approaching ultrathin VO_2 films on sapphire (001) substrates by biased reactive sputtering: Characteristic morphology and its effect on the infrared-light switching. *Journal of Vacuum Science & Technology A*, 39(4):043401, July 2021.

[55] Kevin G. West, Jiwei Lu, Jiani Yu, David Kirkwood, Wei Chen, Yonghang Pei, John Claassen, and Stuart A. Wolf. Growth and characterization of vanadium dioxide thin films prepared by reactive-biased target ion beam deposition. *Journal of Vacuum Science & Technology A: Vacuum, Surfaces, and Films*, 26(1):133–139, January 2008.

[56] Ryan McGee, Ankur Goswami, Soupitak Pal, Kalvin Schofield, Syed Asad Manzoor Bukhari, and Thomas Thundat. Sharpness and intensity modulation of the metal-insulator transition in ultrathin VO_2 films by interfacial structure manipulation. *Physical Review Materials*, 2(3):034605, March 2018.

[57] Yuanjun Yang, Liangxin Wang, Haoliang Huang, Chaoyang Kang, Haitao Zong, Chongwen Zou, Yalin Lu, Xiaoguang Li, Bin Hong, and Chen Gao. Controlling metal-insulator transition in (010)-VO_2/(0001)-Al_2O_3 epitaxial thin film through surface morphological engineering. *Ceramics International*, 44(3):3348–3355, February 2018.

[58] Mengmeng Yang, Yuanjun Yang, Bin Hong, Liangxin Wang, Zhenlin Luo, Xiaoguang Li, Chaoyang Kang, Ming Li, Haitao Zong, and Chen Gao. Surface-growth-mode-induced strain effects on the metal–insulator transition in epitaxial vanadium dioxide thin films. *RSC Advances*, 5(98):80122–80128, September 2015.

[59] Robert E. Marvel, Robert R. Harl, Valentin Craciun, Bridget R. Rogers, and Richard F. Haglund. Influence of deposition process and substrate on the phase transition of vanadium dioxide thin films. *Acta Materialia*, 91:217–226, June 2015.

[60] Deyi Fu, Kai Liu, Tao Tao, Kelvin Lo, Chun Cheng, Bin Liu, Rong Zhang, Hans A. Bechtel, and Junqiao Wu. Comprehensive study of the metal-insulator transition in pulsed laser deposited epitaxial VO_2 thin films. *Journal of Applied Physics*, 113(4):043707, January 2013.

[61] A. Bailly, S. Grenier, M. M. Villamayor, M. Gaudin, A. Y. Ramos, P. Bouvier, C. Bouchard, L. Magaud, L. Laversenne, B. Mongellaz, E. Bellet-Amalric, A. Lacoste, and A. Bès. Three-phase metal-insulator transition and structural alternative for a VO_2 film epitaxially grown on Al2O3(0001). *Journal of Applied Physics*, 126(16):165306, October 2019.

[62] Jingxin Sang, Tan Zheng, Liu Xu, Xin Zhou, Shijian Tian, Jiatong Sun, Xiaofeng Xu, Jianqiang Wang, Shuguang Zhao, and Yang Liu. Modulating the metal-insulator transition in VO_2/Al_2O_3 (001) thin films by grain size and lattice strain. *Journal of Alloys and Compounds*, 876:160208, September 2021.

[63] Joyeeta Nag, E. Andrew Payzant, Karren L. More, and Richard F. Haglund. Enhanced performance of room-temperature-grown epitaxial thin films of vanadium dioxide. *Applied Physics Letters*, 98(25):251916, June 2011.

[64] Hai-Tian Zhang, Craig Eaton, Hansheng Ye, and Roman Engel-Herbert. Phase stabilization of VO_2 thin films in high vacuum. *Journal of Applied Physics*, 118(18):185306, November 2015.

[65] A. Glavic and M. Björck. GenX 3: the latest generation of an established tool. *Journal of Applied Crystallography*, 55(4):1063–1071, August 2022.

[66] Franz J. Giessibl. The qPlus sensor, a powerful core for the atomic force microscope. *Review of Scientific Instruments*, 90(1):011101, January 2019.

[67] Md Mahamudul Hasan, Toyoko Arai, and Masahiko Tomitori. Mechanical energy dissipation of an oscillating cantilever close to a conductive substrate partly covered with thin mica films evaluated by frequency modulation atomic force microscopy. *Japanese Journal of Applied Physics*, 61(6):065006, June 2022.

[68] Omur E. Dagdeviren, Yoichi Miyahara, Aaron Mascaro, and Peter Grütter. Calibration of the oscillation amplitude of electrically excited scanning probe microscopy sensors. *Review of Scientific Instruments*, 90(1):013703, January 2019.

[69] Aleksander Labuda, Yoichi Miyahara, Lynda Cockins, and Peter H. Grütter. Decoupling conservative and dissipative forces in frequency modulation atomic force microscopy. *Physical Review B*, 84(12):125433, September 2011.

[70] Manhee Lee, Bongsu Kim, Sangmin An, and Wonho Jhe. Dynamic Responses of Electrically Driven Quartz Tuning Fork and qPlus Sensor: A Comprehensive Electromechanical Model for Quartz Tuning Fork. *Sensors*, 19(12):2686, January 2019.

[71] Stefan Kuhn and Philipp Rahe. Discriminating short-range from van der Waals forces using total force data in noncontact atomic force microscopy. *Physical Review B*, 89(23):235417, June 2014.

[72] P. Tolias. Non-retarded room temperature Hamaker constants between elemental metals. *Surface Science*, 700:121652, 2020.

[73] Harold D. Ackler, Roger H. French, and Yet-Ming Chiang. Comparisons of Hamaker Constants for Ceramic Systems with Intervening Vacuum or Water: From Force Laws and Physical Properties. *Journal of Colloid and Interface Science*, 179(2):460–469, May 1996.

[74] Lennart Bergstrom. Hamaker constants of inorganic materials. *Advancesin Colloid and Interface Science*, 70:125–169, 1977.

[75] Joshua A. Rackers and Jay W. Ponder. Classical Pauli repulsion: An anisotropic, atomic multipole model. *The Journal of Chemical Physics*, 150(8):084104, February 2019.

[76] M. Guggisberg, M. Bammerlin, Ch. Loppacher, O. Pfeiffer, A. Abdurixit, V. Barwich, R. Bennewitz, A. Baratoff, E. Meyer, and H.-J. Güntherodt. Separation of interactions by noncontact force microscopy. *Physical Review B*, 61(16):11151–11155, April 2000.

[77] Toyoko Arai, Daiki Kura, Ryo Inamura, and Masahiko Tomitori. Resistivity change in Joule heat energy dissipation detected by noncontact atomic force microscopy using a silicon tip terminated with/without atomic hydrogen. *Japanese Journal of Applied Physics*, 57(8S1):08NB04, August 2018.

[78] S. Hudlet, M. Saint Jean, C. Guthmann, and J. Berger. Evaluation of the capacitive force between an atomic force microscopy tip and a metallic surface. *The European Physical Journal B*, 2(1):5–10, April 1998.

[79] John E. Sader and Suzanne P. Jarvis. Accurate formulas for interaction force and energy in frequency modulation force spectroscopy. *Applied Physics Letters*, 84(10):1801–1803, March 2004.

[80] Laura Rodríguez, Elena del Corro, Michele Conroy, Kalani Moore, Felip Sandiumenge, Neus Domingo, José Santiso, and Gustau Catalan. Self-Pixelation Through Fracture in VO_2 Thin Films. *ACS Applied Electronic Materials*, 2(5):1433–1439, May 2020.

[81] Gregory N. Derry, Megan E. Kern, and Eli H. Worth. Recommended values of clean metal surface work functions. *Journal of Vacuum Science & Technology A: Vacuum, Surfaces, and Films*, 33(6):060801, November 2015.

[82] D. E. Eastman. Photoelectric Work Functions of Transition, Rare-Earth, and Noble Metals. *Physical Review B*, 2(1):2, 1970.

[83] N. J. Lee, J. W. Yoo, Y. J. Choi, C. J. Kang, D. Y. Jeon, D. C. Kim, S. Seo, and H. J. Chung. The interlayer screening effect of graphene sheets investigated by Kelvin probe force microscopy. *Applied Physics Letters*, 95(22):222107, November 2009.

[84] Ahrum Sohn, Teruo Kanki, Kotaro Sakai, Hidekazu Tanaka, and Dong-Wook Kim. Fractal Nature of Metallic and Insulating Domain Configurations in a VO_2 Thin Film Revealed by Kelvin Probe Force Microscopy. *Scientific Reports*, 5(1):10417, September 2015.

[85] Dana Longcope. Capacitance of a sphere near a ground plane —images charges to infinity.

[86] J. M. de Voogd, M. A. van Spronsen, F. E. Kalff, B. Bryant, O. Ostojić, A. M. J. den Haan, I. M. N. Groot, T. H. Oosterkamp, A. F. Otte, and M. J. Rost. Fast and reliable pre-approach for scanning probe microscopes based on tip-sample capacitance. *Ultramicroscopy*, 181:61–69, October 2017.

[87] Dilek Yildiz, Marcin Kisiel, Urs Gysin, Oguzhan Gürlü, and Ernst Meyer. Joule meets van der Waals: Mechanical dissipation via image potential states on a topological insulator surface. *Nature Materials*, 18(11):1201–1206, November 2019.

[88] Romain Stomp, Yoichi Miyahara, Sacha Schaer, Qingfeng Sun, Hong Guo, Peter Grutter, Sergei Studenikin, Philip Poole, and Andy Sachrajda. Detection of Single-Electron Charging in an Individual InAs Quantum Dot by Noncontact Atomic-Force Microscopy. *Physical Review Letters*, 94(5):056802, February 2005.

[89] Giancarlo Bartolucci, Giovanni Maria Sardi, Romolo Marcelli, Emanuela Proietti, Andrea Lucibello, Endri Stoja, and Fabrizio Frezza. Modeling of a metallic truncated cone for electromagnetic capacitive sensors. *Journal of Applied Physics*, 118(7):074503, August 2015.

[90] Changhong Chen, Yong Zhao, Xuan Pan, V. Kuryatkov, A. Bernussi, M. Holtz, and Zhaoyang Fan. Influence of defects on structural and electrical properties of VO_2 thin films. *Journal of Applied Physics*, 110(2):023707, July 2011.

[91] A. I. Volokitin and B. N. J. Persson. Near-field radiative heat transfer and noncontact friction. *Reviews of Modern Physics*, 79(4):1291–1329, October 2007.